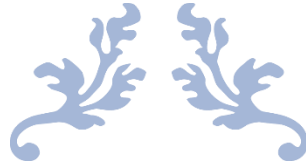




ΠΑΝΕΠΙΣΤΗΜΙΟ ΚΡΗΤΗΣ  
UNIVERSITY OF CRETE



# Manipulating the Exciton in 2D Halide Perovskites: Towards Polaritonics and White-Light Emission

[MASTER THESIS]



Marios-Evangelos Triantafyllou Rundell

Department of Materials Science & Technology

Crystal Chemistry Lab

2020-2021

Supervisor:

Dr Constantinos C. Stoumpos

## **ACKNOWLEDGMENTS**

The author wishes to express sincere appreciation to Professor Constantinos C. Stoumpos for being a great mentor and for his assistance throughout these years. In addition, a big thanks to all group members for their help and the great memories from the lab. A special thanks to colleague Manolis Mavrotsoupakis whose expertise in optical characterization was very helpful during this undertaking. Lastly thanks to the members of the school council for their valuable input.

**Abstract:** The three-dimensional (3D) hybrid organic–inorganic perovskites  $AMX_3$  have shown huge potential for use in solar cells and other optoelectronic devices in the past decade. More recently, two-dimensional (2D) perovskite derivatives have been shown to expand the field into a more diverse subgroup of high-performance semiconducting hybrids that possesses unique photophysical properties. In particular, because of the negligible contributions to the frontier orbitals from the organic cation and to the absence of orbital overlap between the metal-halide layers, electron and hole wave functions are confined within the crystallographically ordered 2D inorganic sublattice, resulting in a natural, multiple quantum-well electronic structure. As a result, the hybrid 2D perovskites are subject to quantum confinement, which leads to an increase in the optical band gap, but, in addition, they are also subject to coulombic screening of the photo-generated electron–hole pairs due to the large dielectric contrast between the organic and inorganic components. The latter feature give rise to a huge exciton binding energies of  $\sim E_b = 200\text{-}500$  meV, which is  $\sim 10$  times larger than  $k_B T$  thermal energy at room temperature.

The present Thesis deals with the crystal chemistry of these materials and attempts to address important questions in the field. The first part of the Thesis deals with the crystal growth of 2D Ruddlesden-Popper-type perovskites  $(BA)_2(MA)_{n-1}Pb_nI_{3n+1}$  ( $BA^+ = CH_3(CH_2)_3NH_3$ ,  $MA^+ = CH_3NH_3$ ;  $n=1\text{-}4$ ) of suitable spatial dimensions and optical quality for use in distributed Bragg reflectors (DBRs) microcavities, towards polaritonic applications. The second part concerns exploratory synthesis of  $APbBr_4$  ( $A^{2+} =$  piperidinium-based ammonium dications) 2D Dion-Jacobson type perovskites, in which the heavy lattice strain introduced by the asymmetric organic cations can lead to broadband emission caused by self-trapping of the exciton and producing efficient, single-component white-light emitters during the process.

## Πίνακας περιεχομένων

<b>1. Introduction</b> .....	4
<b>1.1. 3D Perovskites</b> .....	4
<b>1.2. 2D Perovskites</b> .....	6
<b>1.2.1. A brief history of 2D halide perovskites</b> .....	6
<b>1.2.2 2D halide perovskite structure</b> .....	6
<b>1.3. Optoelectronic diversity</b> .....	9
<b>1.3.1. Excitons</b> .....	9
<b>1.3.2. Electronic Confinement in 2D Perovskites</b> .....	10
<b>1.3.3. Electronic band structure</b> .....	11
<b>1.3.4. Semiconducting properties</b> .....	12
<b>1.3.5. Broad band emission</b> .....	14
<b>1.4. Optoelectronic Applications</b> .....	16
<b>1.4.1. Solar-cell absorbers</b> .....	16
<b>1.4.2. Light-Emitting Diodes</b> .....	16
<b>1.4.3. Lasers</b> .....	17
<b>2. Experimental</b> .....	20
<b>2.1 Synthesis</b> .....	20
<b>2.2 Characterization</b> .....	24
<b>PART 1</b> .....	25
<b>3. Results and Discussion</b> .....	26
<b>PART 2</b> .....	39
<b>4. Results and Discussion</b> .....	40
<b>4.1 Crystal Structures</b> .....	40
<b>4.2 Optical Characterization</b> .....	45
<b>Conclusions</b> .....	49
<b>References</b> .....	50

# 1. Introduction

The first time the word “perovskite” was ever used was back in 1839 when Gustav Rose identified a new crystal he examined as a new mineral with cubic symmetry composed of calcium and titanium oxides.<sup>1</sup> It was until 1844 that his brother Heinrich fully analyzed and deduced the actual chemical composition  $\text{CaTiO}_3$  which is the renowned perovskite. The discovery of  $\text{CH}_3\text{NH}_3\text{PbI}_3$ , a three-dimensional (3D) compound that has a similar structure with the mineral  $\text{CaTiO}_3$ , can be traced back to Weber’s work in 1978<sup>2</sup> but the history of the halide perovskites goes even further back, with the works of Wells (1893)<sup>3</sup> and Møller (1957–1959)<sup>4,5</sup> on  $\text{CsPbX}_3$  and Auger and Karantassis on  $\text{CsSnX}_3$  (1925) and  $\text{CsGeX}_3$  (1935) lead-free analogues.<sup>6,7</sup> Despite the many years that perovskite materials are known and studied, it wasn’t a very popular field of study until the early 21<sup>st</sup> century. It was two big milestones that brought perovskites back in the active battlefield of science. The first was in 2009 when the hybrid halide perovskite  $\text{CH}_3\text{NH}_3\text{PbI}_3$ , was demonstrated by Miyasaka and co-workers as a photosensitizer in dye-sensitized solar cells (DSSCs).<sup>8</sup> And the second was when  $\text{CsSnI}_3$  perovskite was used as a hole transporting material in solid-state DSSCs with ~10% efficiency as reported in 2012 by Kanatzidis and co-workers.<sup>9</sup> Since then the field is constantly evolving and the word perovskite is strongly associated with solar cells (PSCs) which have performed an epic march to >25% efficiencies and have won a spot among other established inorganic semiconductors.<sup>10,11,12,13</sup>

## 1.1. 3D Perovskites

Three-dimensional (3D) halide perovskites, which have the general formula  $\text{A}^{\text{I}}\text{B}^{\text{II}}\text{X}_3$ , consist of  $[\text{BX}_6]^{4-}$  corner-sharing octahedra of divalent B-site cations, bridged by halide anions ( $\text{X} = \text{Cl}^-, \text{Br}^-, \text{I}^-$ ), to create a 3D anionic network. Small monovalent organic or inorganic A-site cations ( $\text{MA}^+$ ,  $\text{FA}^+$ ,  $\text{Cs}^+$ ) occupy cuboctahedral cavities in between the B–X sublattice and provide charge neutrality in the compounds (Figure 1). The first one who estimated the geometrical restrictions required for a perovskite structure to be stable was Goldschmidt,<sup>14</sup> who introduced the namesake tolerance factor,  $t = (r_{\text{A}} + r_{\text{X}}) / [\sqrt{2}(r_{\text{B}} + r_{\text{X}})]$ , where  $r_{\text{A}}$ ,  $r_{\text{B}}$ , and  $r_{\text{X}}$  are the ionic radii of the respective ions in the  $\text{AMX}_3$  formula. If the tolerance factor is in the range of  $0.8 < t < 1.0$  the formation of a perovskitic structure can be achieved; otherwise different structure-types are favored (Figure 2). Following this rule restricts the combination of elements that can form such a structure when it comes down to halide perovskites: (a) the halide ( $\text{X}^-$ ) anions bear a small negative charge sufficient only to compensate metal ions in lower oxidation states, and (b) they have large ionic radii, which

precludes the incorporation of small metal ions. In order to counteract this compositional dearth and using dimensional reduction as a design tool,<sup>15</sup> researchers were oriented towards the development of new structure-types that are in close relationship with the original structure, hoping that these new materials will retain the superb semiconducting properties of the standard halide perovskites.<sup>16</sup>

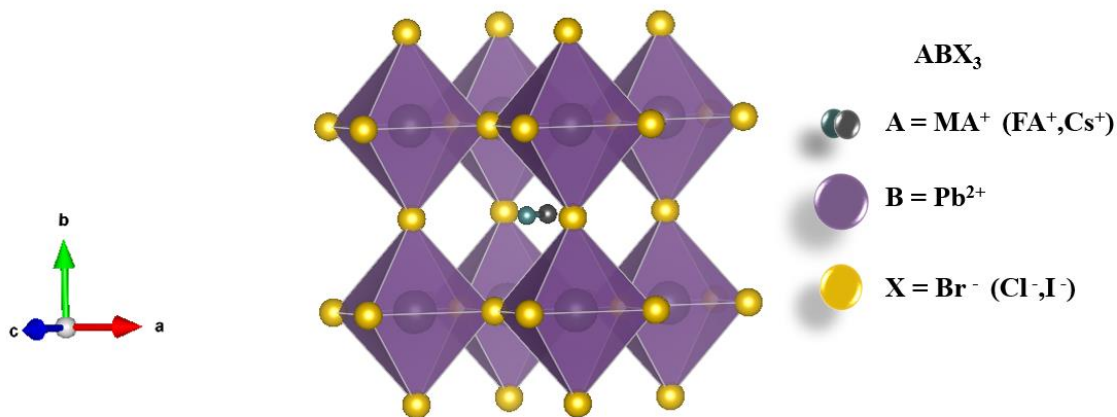


**Figure 1.** Representation of the perovskite unit cell, exemplified on the MAPbBr<sub>3</sub> halide perovskite

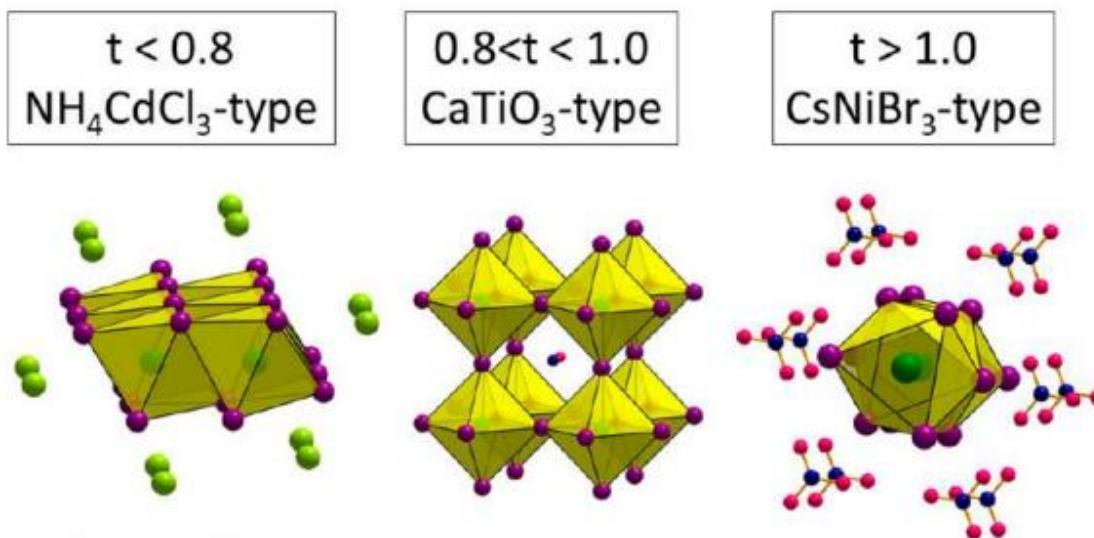


**Figure 2.** Structural motif for the ABX<sub>3</sub> halide compounds as a function of the ionic radii of A<sup>+</sup>, B<sup>2+</sup> and X<sup>-</sup> ions expressed with the tentative tolerance factor value.<sup>17</sup>

## 1.2. 2D Perovskites

### 1.2.1. A brief history of 2D halide perovskites

Two dimensional (2D) perovskites, especially the transition-metal-based structures  $(\text{RNH}_3)_2\text{BX}_4$ , with  $\text{B} = \text{Cd}^{2+}$ ,  $\text{Mn}^{2+}$ ,  $\text{Fe}^{2+}$ ,  $\text{Cu}^{2+}$ ,  $\text{Hg}^{2+}$ , etc., and  $\text{X} = \text{Cl}^-$ ,  $\text{Br}^-$ , have been investigated early on with respect to their dielectric and magnetic properties.<sup>18,19,20</sup> Exploration of a lead-based purely semiconducting 2D system was reported by Maruyama and co-workers for  $(\text{CH}_3(\text{CH}_2)_8\text{NH}_3)_2\text{PbI}_4$  in 1986<sup>21</sup> followed by Ishihara et al.,<sup>16</sup> Papavassiliou et al.,<sup>22</sup> and Thorn et al.<sup>23</sup> who systematically studied the optical properties of the materials. Mitzi and co-workers combined the collective knowledge of that time into a well-defined research field and laid the groundwork for the explosive growth of 2D halide perovskite semiconductors. Their report on the evolution of the  $(\text{C}_4\text{H}_9\text{NH}_3)_2(\text{CH}_3\text{NH}_3)_{n-1}\text{Sn}_n\text{I}_{3n+1}$  ( $n = 1-5$ ) homologous series for many-n members and demonstrated how the electrical properties of the compounds may change as a function of  $n$ , from the nearly intrinsic  $n = 1$  to the heavily doped,  $n = \infty$ .<sup>24</sup>

### 1.2.2 2D halide perovskite structure

Through the dimensional reduction of the 3D crystal lattice, 2D perovskites,  $(\text{A}')_m(\text{A})_{n-1}\text{B}_n\text{X}_{3n+1}$ , adopt a new structural and compositional dimension,  $\text{A}'$ , where monovalent ( $m = 2$ ) or divalent ( $m = 1$ ) cations can intercalate between the anions of the 2D perovskite sheets. Slicing a 3D perovskite lattice along a specific crystallographic direction by incorporating a large  $\text{A}'$ -site cation in between the inorganic perovskitic layers anyone can rather easily extract a two-dimensional layered halide perovskite (2D-perovskite). Most 2D perovskites derive from the (100) crystallographic plane of the 3D cubic perovskite but there are also others that have been reported (Figure 3a). Typically,  $\text{A}'$ -site cations which can pack efficiently, are more common in 2D layers of corner-sharing metal halide octahedra. In the 2D hybrid halide perovskites, the organic cations act as insulating barriers that confine the charge carriers in two dimensions, but they also serve as dielectric moderators that determine the electrostatic forces exerted on the photogenerated electron-hole pairs. The specific arrangement of alternating organic-inorganic layers generates a crystallographically ordered 2D multiple-quantum-well (MQW) electronic structure that forms naturally through self-assembly. (Figure 3b). In addition, due to the high organic/inorganic dielectric contrast, the perovskite materials generate huge electron-hole binding energies. 2D halide perovskite MQWs can stabilize

excitons that can be readily observed even at ambient temperatures. The (100) orientation has great tolerance in both inorganic and organic components, leading to a high degree of compositional diversity and tunability. By changing the size of the inorganic layer which is quantified as “n”, (n) for the number of octahedral layers that make up a single sheet, we can change the bandgap of the compound as more layers mean more electrons and electronic states (Figure 3b) and by changing the organic layer we can bring closer or dissociate the octahedra alternating this way the size of the barrier.



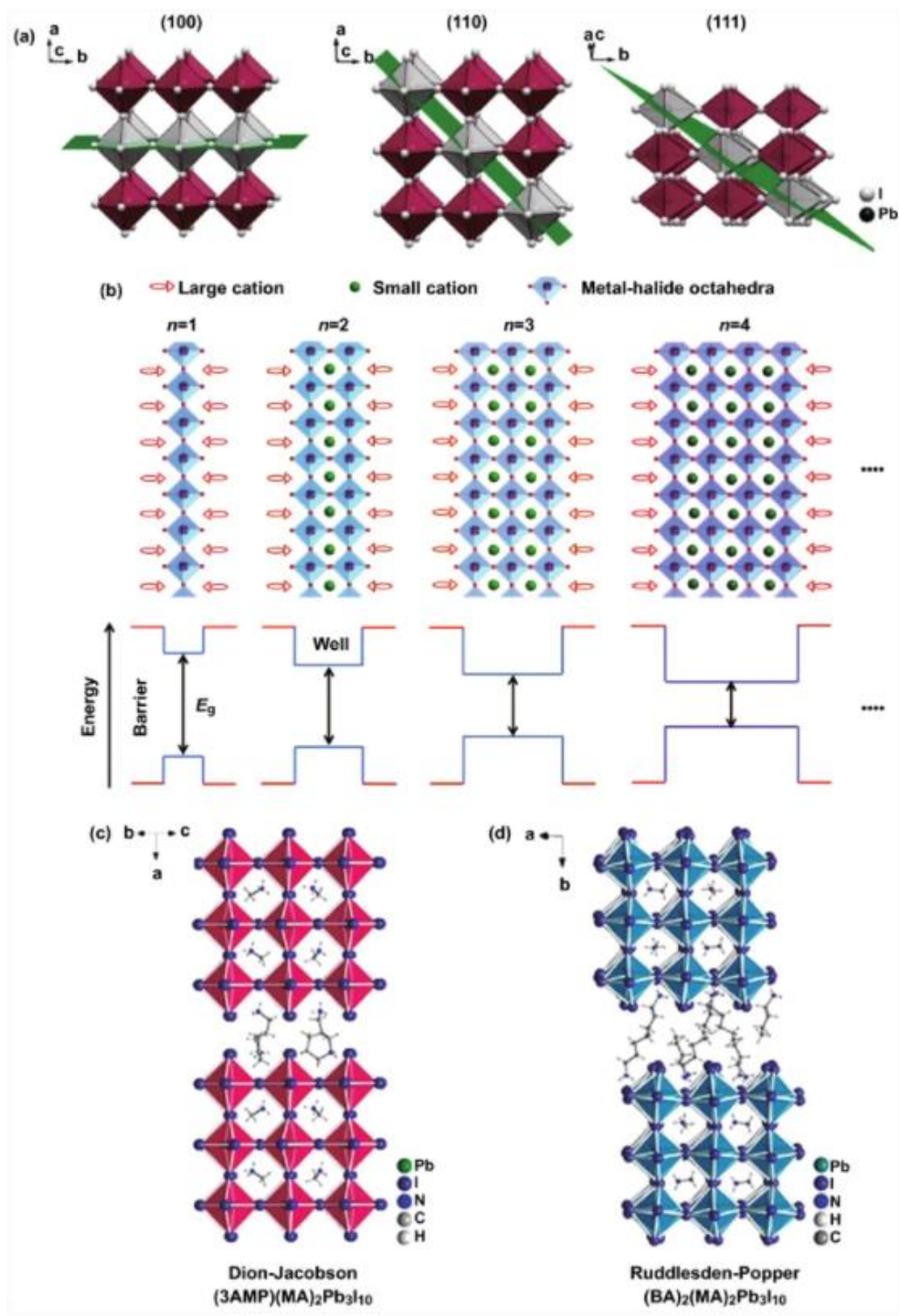


**Figure 3.** **a** Schematic diagram of 2D perovskite series with different orientations.<sup>25</sup> **b** Schematic diagram of quantum wells perovskites comparing to the inorganic layer thickness ( $n$ ).<sup>26</sup> **c** Dion-Jacobson phase and **d** Ruddlesden-Popper phase for halide perovskite. 3AMP = 3-(aminomethyl)piperidinium, MA = methylammonium, BA = butylammonium.<sup>27</sup>

The (100)-oriented perovskites can be further categorized as the Ruddlesden–Popper (RP) phases,<sup>28,29</sup> the Dion–Jacobson (DJ) phases,<sup>30,31</sup> and the Aurivillius phases,<sup>32,33</sup> the general formulas of which can be written as  $A'_2A_{n-1}B_nO_{3n+1}$ ,  $A'A_{n-1}B_nO_{3n+1}$ , and  $(Bi_2O_2)(A_{n-1}B_nO_{3n+1})$ , respectively. Already from the chemical formula, it is clear that the charge of the spacer cation defines the structural type of 2D perovskites. Both the RP and DJ phases can be formed with the halide family, having the general formulas  $A'_2A_{n-1}B_nX_{3n+1}$  and  $A'A_{n-1}B_nX_{3n+1}$  ( $A'$  = interlayer “spacer” cation), respectively.<sup>34</sup> Their obvious difference is that for the RP phase the layers are offset by one octahedral unit showing a  $(\frac{1}{2}, \frac{1}{2})$  in-plane displacement while on the other hand, the DJ phase does not exhibit any shift and the layers are stacked perfectly on top of each other (Figure 3c,d). Because of this difference in the structure, the RP phases will need a bilayer of spacers to ‘line up’ and stabilize the shifted structure and thus have a larger interlayer distance up to 2 times the length of the cation, depending on if there is an overlap or not (Figure 3d). In the case of the RP phases, the layers are well “isolated”, showing no interactions between the inorganic sheets, thereby producing an excitonic emission that results directly from the spatial electronic confinement (n) of the individual layers while in the case of DJ phases the proximity of the layers generates a weak interaction between the octahedral layers which can be readily observed in the position of the exciton, which shows a pronounced redshift.

### 1.3. Optoelectronic diversity

In 3D Pb iodide perovskites, photoexcitation at room temperature generates free electrons and holes. In dimensionally confined systems such as 2D Pb iodide perovskites, however, the excited electrons are strongly attracted to the holes they create via Coulomb interactions. These neutral electron-hole pairs, called

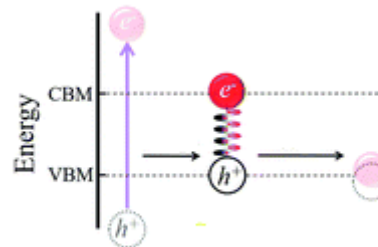


Fig 4. Exciton formation

excitons, can be considered as transient, light-induced dipoles in the material. Excitons are energetically stabilized relative to the free carriers by the exciton binding energy ( $E_b$ ), i.e., the coulombic attraction between the electron and the hole (Figure 4).<sup>35</sup>

#### 1.3.1. Excitons

Excited electrons and holes can experience an energetically stabilizing Coulombic attraction, forming an electrostatically neutral quasiparticle, called a bound exciton.<sup>36</sup> Excitons are stabilized

relative to their free carrier constituents by the exciton binding energy ( $E_b$ ), a quantity whose magnitude describes the energy needed to separate the Coulombically bound charges.<sup>37</sup>

In the layered lead halide perovskites, the full wealth of exciton types have been observed, including free (FE), bound (BE), and self-trapped excitons (STE). The free exciton is the neutral electron–hole quasiparticle that is free to migrate in the material and is essentially unaffected by defects or impurities in the lattice. However, excitons can interact with defects, localizing to the impurity to become bound excitons. Excitons can localize even in the absence of lattice defects, through the creation of transient lattice defects, in a process termed “self-trapping”. In a material with significant coupling between the exciton and the lattice (exciton-phonon coupling), the exciton generates a lattice distortion and becomes (self)-trapped by the distortion it induced and either propagates through the lattice or localizes in specific lattice positions.<sup>38</sup> When localized, STEs behave as small polarons (charge carriers that induce local lattice distortions owing to strong carrier–phonon coupling), as opposed to the large polarons which are thought to form when the lattice does not possess any “natural” trap sites and the excitons are allowed to propagate further.<sup>39</sup> Although excitons are neutral quasiparticles and are thus uncharged and can be considered as excited-state defects, as they exist only upon excitation, and the lattice distortion disappears following decay to the ground state.

### 1.3.2. Electronic Confinement in 2D Perovskites

Despite the ubiquity of excitons in semiconductors and insulators, excitons are often observed only at low temperatures. When thermal energy ( $k_B T = 25.7$  meV at 298 K) is greater than  $E_b$ , excitons ionize to form free carriers. For example,  $E_b$  is less than 5 meV in the textbook semiconductor GaAs<sup>40</sup>. However, excitonic features are visible for the majority of lead-halide perovskites even at room temperature. In fact,  $E_b$  values for layered lead-halide perovskites can be as high as 500 meV.<sup>41</sup> These anomalously large  $E_b$  values can be explained by contributions from two effects: quantum confinement and dielectric confinement as described below.

As already mentioned, layers in 2D perovskites are alternating between inorganic octahedra and organic cations in a crystallographically ordered fashion and as a result they form a quantum well electronic structure where the inorganic layers are the semiconducting wells and the organic layers are the insulating barriers. The fundamental physics of quantum wells,<sup>42</sup> such as quantum and

dielectric confinement, qualitatively apply to 2D perovskites<sup>43,44</sup>. The inorganic sheets confine the lattice to two dimensions and, as a result of the spatial confinement, the band gap opens up to accommodate discrete energy levels across the stacking spatial dimension (quantum confinement). On the other hand, the dielectric contrast between the highly polarizable inorganic lattice and the non-polarizable organic interlayers gives rise to a massive dielectric stabilization of the excitons, which effectively quadruple the  $E_b$  and halve the Bohr radius relative to a 3D material (dielectric confinement).<sup>45</sup> Typically, the organic layers have a low dielectric constants ( $\epsilon_\infty \sim 2$  aliphatic carbon chains) relative to the inorganic layers (3-6 for lead halide perovskites)<sup>32,46</sup>

### 1.3.3. Electronic band structure

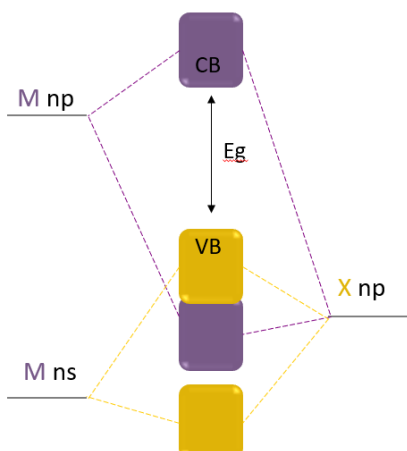


Figure 5. Schematic molecular orbital diagram

The lead-halide perovskites are direct-bandgap semiconductors in which halide (X) np and Pb 6s orbitals compose the valence band maximum, while the conduction band minimum mostly comprises Pb 6p orbitals (Figure 5).<sup>47</sup> Here, the relativistic contraction of the Pb 6s orbital pushes it below the valence band maximum, likely offering more protection from oxidation compared to the lighter  $\text{Sn}^{2+}$  and  $\text{Ge}^{2+}$  congeners.<sup>48</sup> Therefore, the excited states and photophysics of these materials are controlled by the structure and composition of the inorganic layer, with the organic cations providing indirect effects related with stereochemistry and charge distribution.

Increasing halide electronegativity selectively lowers the energy of the valence band maximum but leaves the conduction band minimum mostly unchanged, thereby increasing the bandgap.

Apart from compositional changes, two main structural parameters substantially tune the photophysical properties of these materials: the thickness and the connectivity of the inorganic sheets. As stated earlier the thickness is analogous to the number of inorganic octahedra ( $n$ ) so the optoelectronic properties of these materials also vary as a function of  $n$ . As the inorganic layer thickness increases, the optoelectronic properties of the 2D perovskite approach those of the 3D perovskite, with decreasing  $E_g$  and  $E_b$ . For the  $(\text{CH}_3(\text{CH}_2)_3\text{NH}_3)_2(\text{CH}_3\text{NH}_3)_{n-1}\text{Pb}_n\text{I}_{3n+1}$  (or  $(\text{BA})_2(\text{MA})_{n-1}\text{Pb}_n\text{I}_{3n+1}$  for convenience) system, which is the main homologous system studied in

this Thesis, the PL energy ranges from 2.35 to 1.83 eV for  $n$  values 1 through 5, quadratically decaying to the energy gap of the  $n = \infty$  perovskite at 1.60 eV.<sup>49,50</sup> Bandgap tuning through sheet thickness is reflected in the perovskite's color, with typical  $n = 1$  Pb iodide perovskites appearing yellow-orange and  $n \geq 2$  Pb iodide perovskites appearing dark red ( $n = 2, 3$ ) or black ( $n \geq 4$ ) (Figure 6).

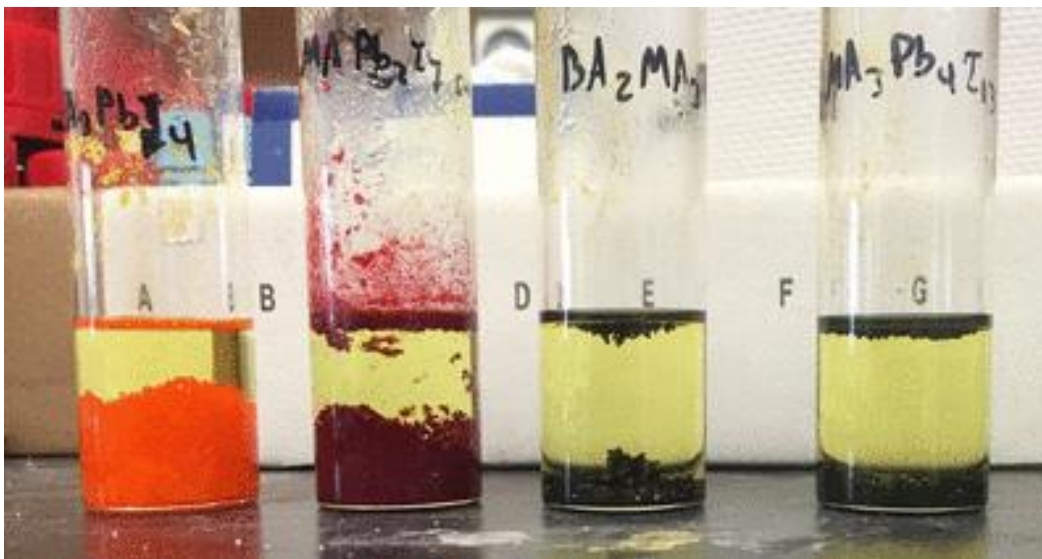


**Figure 6.** Image of crystal colour change for  $(\text{BA})_2(\text{MA})_{n-1}\text{Pb}_n\text{I}_{3n+1}$  ( $n=1-4$ ) perovskite.<sup>42</sup>

#### 1.3.4. Semiconducting properties

The properties of 2D halide perovskites are governed by their unusual absorption spectra which feature a coexistence an extended band edge (typical of an extended solid) as well as peak-shaped (typical in molecular solid). These peak-shaped features are the signature appearance of stable excitons in the materials (Fig 7). Due to the difficulty of determining the bandgap from the absorption spectra, this is commonly determined by means of photoluminescence (PL) emission spectroscopy. The room-temperature PL spectra typically reveal the radiative recombination of the excitons originating from the inorganic layers of 2D perovskites. The width of the excitonic emission can range from narrow (full width at half-maximum (fwhm) ca. 100 meV)<sup>16,51</sup> to extremely broad (fwhm ca. 1 eV)<sup>52</sup> depending on the nature of the A-, B-, and X-site constituents of the perovskite compound.



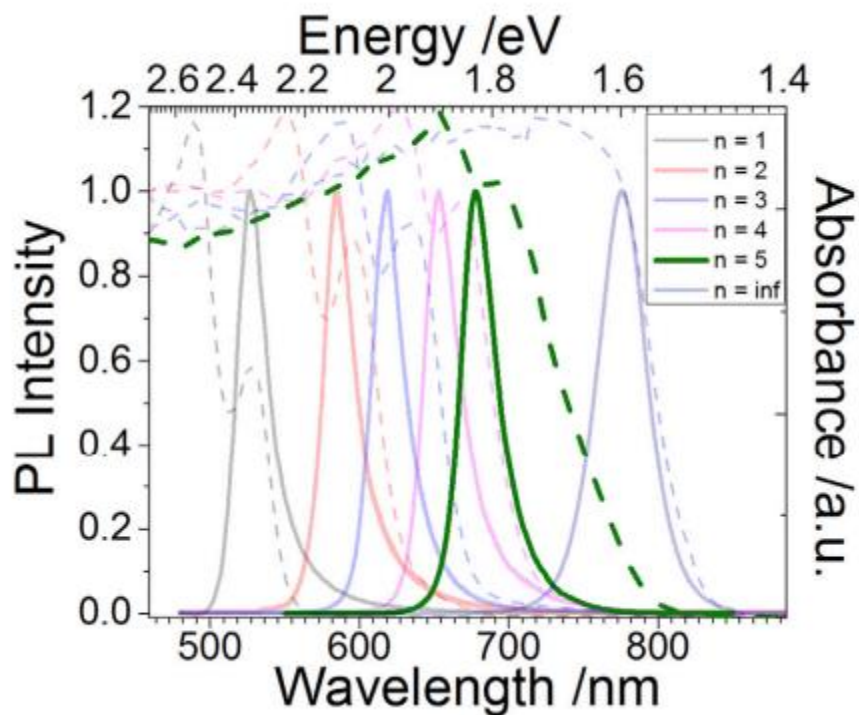


**Figure 7.** Optical absorption and emission spectra of  $(\text{BA})_2(\text{MA})_{n-1}\text{Pb}_n\text{I}_{3n+1}$  ( $n=1-\infty$ ).<sup>53</sup>

The primary source of PL in (100) lead-halide perovskites is free-excitonic recombination, which manifests as a blue ( $X = \text{Cl}, \text{Br}$ ) or green ( $X = \text{I}$ ) light. Room-temperature photoluminescence quantum efficiencies (PLQE) up to 22% have been obtained for this emission.<sup>54</sup> Although most perovskites show narrow emission, the narrow and broad emissions appear to be connected by a simple thermal equilibrium between free and self-trapped excitonic states. Self-trapping reflects the bulk properties of the lattice such as the extent of exciton-lattice coupling and lattice deformability. Therefore, changes to the overall crystal structure should systematically affect the broad emission. In a series of experiments conducted by *Smith MD et. al.*<sup>44</sup> the only structural parameter that showed a strong correlation with the broad emission was the out-of-plane interoctahedral tilt angle (where the plane is defined by the Pb atoms). This provides the design rule that large out-of-plane tilting of the metal-halide octahedra increases the likelihood of a perovskite emitting white light. From the exciton's perspective, this deformation may prime the inorganic layers for the excited-state distortion that occurs upon self-trapping. Further understanding of the relationship between STEs and the perovskite crystal structure should reveal more design rules for the synthesis of white-light-emitting perovskites and related metal halides.

### 1.3.5. Broad band emission

Much of the original interest in the layered lead halide perovskites stemmed from their narrow, free-excitonic photoluminescence,<sup>37</sup> studied since the late 1980s by Ishihara and colleagues,<sup>17</sup> with only occasional observations of Stokes shifted luminescence. However, a small subset of 2D perovskites exhibit highly Stokes shifted broadband PL at room temperature, with near ultraviolet photoexcitation resulting in broad visible emission; in some perovskites, the emission is sufficiently broad to cover the entire visible spectrum, resulting in “white light”.<sup>55</sup>

Because of the focus on understanding the narrow, free excitonic emission (fwhm ca. 100 meV) from 2D perovskites,<sup>56,57</sup> white-light-emitting perovskites were not studied until 2014 by Karunadasa and colleagues.<sup>58,59</sup> These 2D lead-halide perovskites were (EDBE)PbX<sub>4</sub> (X = Cl or Br) and (N-MEDA)PbX<sub>4</sub> (X = Br), where EDBE is 2,2'-(ethylenedioxy)bis(ethylammonium), and N-MEDA is N1 - methylethane-1,2-diammonium.<sup>59,62</sup> Upon UV excitation, the inorganic layers of these perovskites emit continuously across the entire visible spectrum (spanning 400–700 nm), appearing white.

One of the most desirable aspects of artificial indoor illumination is its ability to accurately reproduce the color of objects relative to how they appear in natural light. A quantitative measure of this is known as the color rendering index (CRI), with values ranging from 0 to 100, where 100 is standardized daylight.<sup>60</sup> To date, the incandescent light bulb remains one of the highest-quality light sources, with a CRI value of 98; however, its poor energy efficiency and lifespan make it less than ideal as an illumination source.<sup>61</sup> Many of the white-light-emitting perovskites have CRI values above 80 which is unusual for a single emitter to span the entire visible spectrum since a typical white-light mechanism involves the combination of more than one monochromatic light source to emulate a broadband white light spectrum. This is why the source of the broadband emission from 2D perovskites has been studied since 2014. Most of the reports on broadband photoluminescence in the 2D perovskites implicate exciton self-trapping as the dominant emission mechanism.<sup>59</sup>

Mechanistically, broadband emission has been attributed to the radiative decay from the trapped exciton states, and becomes the dominant emission at cryogenic temperatures. Both the free excitons (FE) as well as the phonon-assisted self-trapped excitons (STE) are affected by materials defects which can lead to changes so much in the energy as much as the bandwidth (Figure 8).<sup>60</sup>

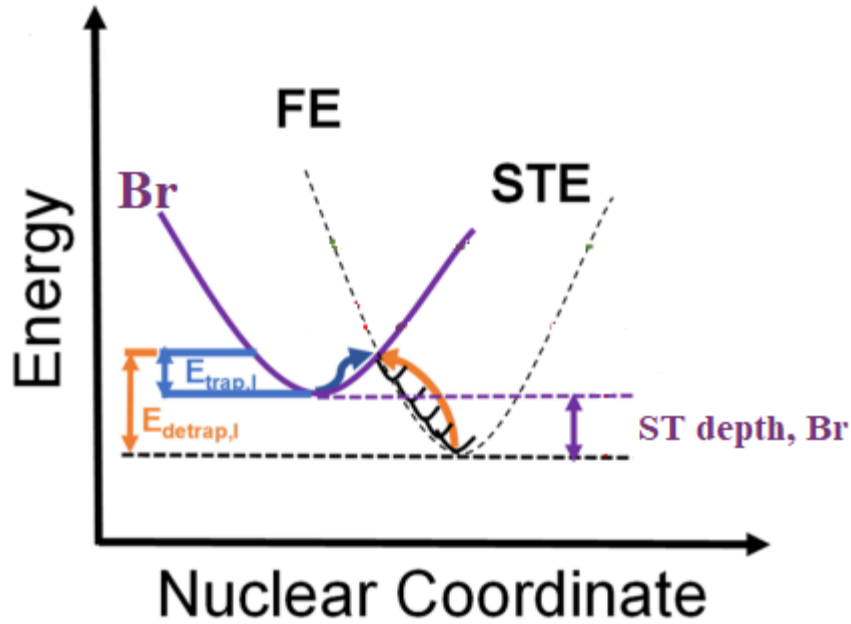


**Figure 8.** Schematic comparison of self-trapping mechanism. Self-trapping (blue arrow) and detrapping (orange arrow) , (FE = free exciton state, STE = self-trapped exciton state,  $E_{\text{trap,l}}$  = energy for self-trapping,  $E_{\text{detrapp,l}}$  = energy for detrapping, self-trapping (ST) depth = energy difference between FE and STE).

In intrinsic self-trapping, strong exciton–lattice coupling causes large structural distortions in the excited state. This lattice deformation leads to a homogeneously broadened emission width, while both the lattice distortion and the stabilization of the self-trapped exciton with respect to the free exciton result in the large Stokes shift. Homogeneous broadening by itself is unlikely to generate enough spectral width to be responsible for the white-light emission. Self-trapping events that occur near-native lattice defects (e.g., lattice vacancies), also called extrinsic self-trapping, can cause inhomogeneities in the excited state, resulting in a distribution of self-trapped states.<sup>62</sup> Emission from such distinct environments can give rise to different optical frequencies and lifetimes, further increasing the emission width. Extrinsic defects, such as vacancies, are essentially static on fast time scales. To account for the very broad continuous spectrum, there would have to be a very large number of such defects. A very high concentration of static defects is unlikely in the single crystals studied here. In addition, the time independence of the emission spectrum is also observed in the spin-coated film, which would be expected to have a much higher concentration of extrinsic defects than the single crystals. Thomaz J. E. et al. proposed that rapid structural fluctuations cause excitations to experience all environments faster than the emission decay time scale, resulting in



identical emission dynamics at all wavelengths.<sup>63</sup> In this section, we also highlight several sets of perovskites that exhibit broad, non-free-excitonic luminescence. We report here a variety of hybrid lead bromide perovskites focusing on their white-light emission properties.

## 1.4. Optoelectronic Applications

Several 2D perovskites have been deployed in actual devices that show superb performance. Their hybrid inorganic–organic nature allows for the development of multifunctional materials with the added advantage over the 3D perovskites of having enhanced environmental stability,<sup>64</sup> reduced ionic migration,<sup>65</sup> and easily tunable electrical properties.<sup>66</sup>

### 1.4.1. Solar-cell absorbers

The low  $E_g$  and  $E_b$  of 3D Pb–I perovskites are instrumental in their high performance as solar-cell absorbers.<sup>67</sup> The higher  $E_g$  and  $E_b$  of the 2D counterpart, at the lowest thickness ( $n=1$ ) makes them seem unsuitable for this application. By increasing the layer thickness of the inorganic sheets though, the optical properties and values of the 2D perovskites start to resemble those of their 3D congeners. A layered perovskite solar cell was first demonstrated by Karunadasa and coworkers<sup>45</sup> in 2014 using the  $n = 3$  perovskite  $(C_6H_5(CH_2)_2NH_3)_2(CH_3NH_3)_2Pb_3I_{10}$  (or  $(PEA)_2(MA)_2Pb_3I_{10}$  for convenience). The first device showed a power conversion efficiency of 4.73% under ambient conditions, without encapsulation with much greater resistance to humidity than the 3D counterpart.<sup>45</sup> Since then, several  $n > 1$  perovskite absorbers have been described, with device efficiencies improving rapidly, including 12.5% for  $n = 4$  perovskites reported by Mohite, Kanatzidis, and coworkers.<sup>68</sup> The inorganic layers need to be aligned perpendicularly to the substrate to allow facile charge transport between the electrodes. As  $n$  increases, the perovskite contains a distribution of  $n$  values in the films. High  $n$  values provide better sunlight absorption and higher carrier mobility, whereas low  $n$  values provide moisture resistance (attributed to the hydrophobicity of the organic layers) and higher-quality films.<sup>45</sup> Finding balance between those two is therefore the key in finding the best all-around perovskite-based solar cell.

### 1.4.2. Light-Emitting Diodes

The first report of electroluminescence was from Nurmikko and co-workers in 1992, using  $(C_6H_5(CH_2)_2NH_3)_2Pb_2I_7$  simply connected to a power supply with silver contacts.<sup>69</sup> Light-emitting diodes as devices came shortly after that and they consisted of 2D Pb iodide perovskite thin films

spin-coated on a transparent conductive oxide substrate, followed by an electron transport layer and low work function metal. The electron transport layer also served as a hole-blocking layer, so an injection of charge carriers results in the formation of excitons in the layered perovskite and subsequent electroluminescence. Despite the improvement of these initial devices, bright electroluminescence was observed only upon cooling below 110 K.<sup>70</sup> In 1999, Chondroudis and Mitzi<sup>71</sup> prepared the first device that operated at lower potentials and was bright even at room temperature. Unlike previous work, in this case, charge carriers are injected from the inorganic sheets into the organic layer, which then emits green light but with poor conversion efficiency. In the last 5 years, more efficient LEDs have been fabricated again with the thickness ( $n$ ) of the layers somewhere between  $n=1$  and  $n=\infty$  as this is where the material provides good carrier mobility and enhanced emission.

### 1.4.3. Lasers

A Light Amplification by Stimulated Emission of Radiation (LASER) device is a strong coherent light source that is generated by light amplification via stimulated emission of the gain medium (i.e., gas, dye, doped-glass, semiconductors, and so forth). Semiconductor lasers are one of the most common and important lasers due to their long lifetime, small volume, low electric injection power, and good integration with mature semiconductor technology. However, the main materials for industrially applicable semiconductor lasers, namely II–VI/ III–V semiconductors such as CdSe, GaN, InP, and GaAs, are fabricated via high-cost and high energy-consuming routes such as metal–organic chemical vapor deposition (MOCVD) and molecular beam epitaxy (MBE).<sup>72</sup> Replacing them with low-temperature solution-processable semiconductors such as 2D perovskites will not only reduce the cost of the lasers but also extend the laser-related applications.

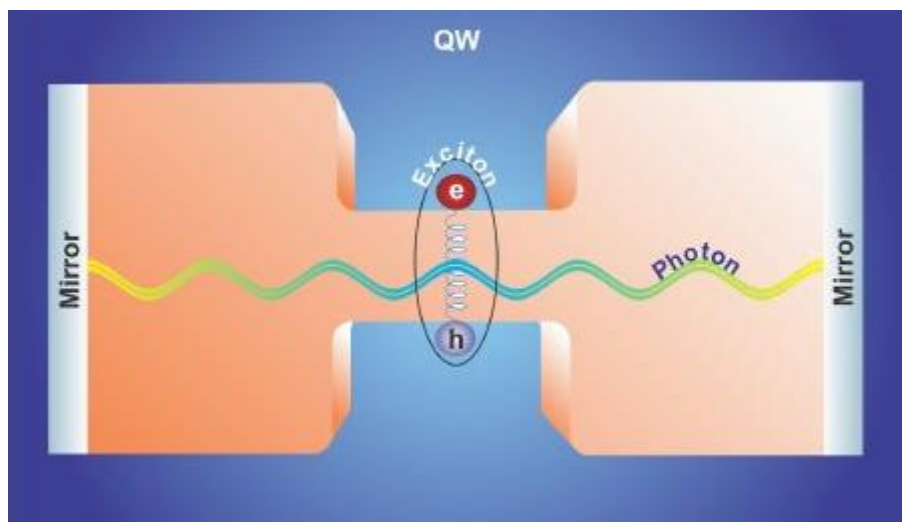


**Figure 9.** Schematics of exciton-polariton microcavity<sup>73</sup>

The long exciton lifetime at room temperatures in 2D halide perovskites opened a new path of possibilities for polariton lasing.<sup>74</sup> Polaritons are nonlinear bosonic quasi-particles resulting from strong photon-exciton coupling and exist inside semiconductor microcavities. The effect of the cavity is to create strong coupling between the mobile excitons and photons, resulting in new quasiparticles which are a superposition of the two: exciton-polaritons. A typical planar microcavity consists of several quantum wells (QWs) sandwiched between two mirrors (Figure 9). Most used mirrors are distributed Bragg reflectors (DBRs) which essentially is a dielectric heterostructure formed from multiple layers of alternating mirrors with varying refractive indices. Each layer causes a partial reflection of an optical wave and the ones with wavelength 4 times the thickness of the layer combine with constructive interference, so the layers act as high-quality nearly 100% reflectors. The existence of multiple QWs is very important for the formation and stability of excitons and consequently polaritons as they obey bosonic statistics as long as their density is low enough so they do not overlap. By using several QWs the distribution is much larger and you can avoid reaching this saturation density while also enhancing the cavity coupling.

The scope of this thesis is to create a functional microcavity with the 2D halide perovskite  $(\text{CH}_3(\text{CH}_2)_3\text{NH}_3)_2(\text{CH}_3\text{NH}_3)_{n-1}\text{Pb}_n\text{I}_{3n+1}$  or  $(\text{BA})_2(\text{MA})_{n-1}\text{Pb}_n\text{I}_{3n+1}$  as the semiconductor and demonstrate the formation of polaritons. Towards this end, we synthesized and tested perovskites from the homologous  $(\text{CH}_3(\text{CH}_2)_3\text{NH}_3)_2(\text{CH}_3\text{NH}_3)_{n-1}\text{Pb}_n\text{I}_{3n+1}$  series with  $1 \leq n \leq 4$ . Initial screening revealed that the  $(\text{BA})_2(\text{MA})_2\text{Pb}_3\text{I}_{10}$  ( $n=3$ ), as the emission spectrum it provides is the most suitable

for use in the fabricated DBRs. Through optimization of the synthesis, crystal growth and exfoliation processes, we were able to prepare perovskite crystals as thin as 50nm with perfectly parallel crystal facets that were suitable to use in a DBR microcavity. All the samples were characterized with powder XRD, UV-Vis-NIR spectroscopy, Photoluminescence and electron microscopy

## 2. Experimental

### 2.1 Synthesis

**Starting Materials.** All chemicals were purchased from Sigma-Aldrich and use as received.

For convenience, we denote the 2D  $(n\text{-CH}_3(\text{CH}_2)_3\text{NH}_3)_2(\text{CH}_3\text{NH}_3)_{n-1}\text{Pb}_n\text{I}_{3n+1}$  family as  $(\text{BA})_2(\text{MA})_{n-1}\text{Pb}_n\text{I}_{3n+1}$  ( $n=1,2,3,4$ ) throughout.

#### *Iodide perovskites*

##### **1<sup>st</sup> Method: Solution process (SP)** <sup>42</sup>

**(BA)<sub>2</sub>PbI<sub>4</sub> (n=1).** PbO powder (2232 mg, 10 mmol) was dissolved in a mixture of 57% w/w aqueous HI solution (10.0 mL, 76mmol) and 50% aqueous H<sub>3</sub>PO<sub>2</sub> (1.7mL, 15.5mmol) in a 20 mL glass vial by heating to boiling under constant magnetic stirring for about 5 min, which formed a bright yellow solution. In a separate beaker, n-CH<sub>3</sub>(CH<sub>2</sub>)<sub>3</sub>NH<sub>2</sub> (924μL, 10mmol) was neutralized with HI 57% w/w (5mL, 38mmol) resulting in a clear pale yellow solution and then was added to the PbI<sub>2</sub> solution slowly. The stirring was then discontinued, and the solution was left to cool on a hot plate to room temperature during which time orange crystals started to crystallize. The crystals were isolated by suction filtration and thoroughly dried under reduced pressure.

**(BA)<sub>2</sub>MAPb<sub>2</sub>I<sub>7</sub> (n=2).** PbO powder (2232 mg, 10 mmol) was dissolved in a mixture of 57% w/w aqueous HI solution (10.0 mL, 76mmol) and 50% aqueous H<sub>3</sub>PO<sub>2</sub> (1.7mL, 15.5mmol) in a 20 mL glass vial by heating to boiling under constant magnetic stirring for about 5 min, which formed a bright yellow solution. Subsequent addition of solid CH<sub>3</sub>NH<sub>3</sub>Cl (338mg, 5mmol) to the hot yellow solution initially caused the precipitation of a black powder, which was rapidly redissolved under stirring to afford a clear bright yellow solution. In a separate beaker, n-CH<sub>3</sub>(CH<sub>2</sub>)<sub>3</sub>NH<sub>2</sub> (694μL, 7mmol) was neutralized with HI 57% w/w (5mL, 38mmol) resulting in a clear pale yellow solution and then was added to the PbI<sub>2</sub> solution slowly. The stirring was then discontinued, and the solution was left to cool on a hot plate to room temperature during which time cherry red crystals started to

crystallize. The crystals were isolated by suction filtration and thoroughly dried under reduced pressure.

**(BA)<sub>2</sub>(MA)<sub>2</sub>Pb<sub>3</sub>I<sub>10</sub> (n=3).** PbO powder (2232 mg, 10 mmol) was dissolved in a mixture of 57% w/w aqueous HI solution (10.0 mL, 76mmol) and 50% aqueous H<sub>3</sub>PO<sub>2</sub> (1.7mL, 15.5mmol) in a 20 mL glass vial by heating to boiling under constant magnetic stirring for about 5 min, which formed a bright yellow solution. Subsequent addition of solid CH<sub>3</sub>NH<sub>3</sub>Cl (450mg, 6.7mmol) to the hot yellow solution initially caused the precipitation of a black powder, which was rapidly redissolved under stirring to afford a clear bright yellow solution. In a separate beaker, n-CH<sub>3</sub>(CH<sub>2</sub>)<sub>3</sub>NH<sub>2</sub> (326μL, 3.33mmol) was neutralized with HI 57% w/w (5mL, 38mmol) resulting in a clear pale yellow solution and then was added to the PbI<sub>2</sub> solution slowly. The stirring was then discontinued, and the solution was left to cool on a hot plate to room temperature during which time dark red/purple crystals started to crystallize. The crystals were isolated by suction filtration and thoroughly dried under reduced pressure.

**(BA)<sub>2</sub>(MA)<sub>3</sub>Pb<sub>4</sub>I<sub>13</sub> (n=4).** PbO powder (2232 mg, 10 mmol) was dissolved in a mixture of 57% w/w aqueous HI solution (10.0 mL, 76mmol) and 50% aqueous H<sub>3</sub>PO<sub>2</sub> (1.7mL, 15.5mmol) in a 20 mL glass vial by heating to boiling under constant magnetic stirring for about 5 min, which formed a bright yellow solution. Subsequent addition of solid CH<sub>3</sub>NH<sub>3</sub>Cl (507mg, 7.5mmol) to the hot yellow solution initially caused the precipitation of a black powder, which was rapidly redissolved under stirring to afford a clear bright yellow solution. In a separate beaker, n-CH<sub>3</sub>(CH<sub>2</sub>)<sub>3</sub>NH<sub>2</sub> (248μL, 2.5mmol) was neutralized with HI 57% w/w (5mL, 38mmol) resulting in a clear pale yellow solution and then was added to the PbI<sub>2</sub> solution slowly. The stirring was then discontinued, and the solution was left to cool on a hot plate to room temperature during which time black crystals started to crystallize. The crystals were isolated by suction filtration and thoroughly dried under reduced pressure.

## **2<sup>nd</sup> Method: Floating Growth of large-area thin sheets (FG)<sup>75</sup>**

2D RP perovskite thin sheets were synthesized using an interfacial growth method, with the precursor species, concentrations, and ratios carefully optimized and the crystallization temperature carefully controlled to promote layer-by-layer growth, avoid dislocation formation, maximize lateral growth and maintain phase purity. Only the  $(\text{BA})_2(\text{MA})_2\text{Pb}_3\text{I}_{10}$  ( $n=3$ ) was synthesized with both methods, for reasons explained later in section 3, and the synthesis is described below:

$\text{PbI}_2$  (0.59M) and  $\text{CH}_3\text{NH}_3\text{Cl}$  (0.40M) precursors were dispersed in a concentrated aqueous solution of HI and  $\text{H}_3\text{PO}_2$  mixture (10:1 vol/vol) and then heated at  $130^\circ\text{C}$  in a closed glass vial until a clear, yellow solution was obtained. In a separate beaker,  $n\text{-CH}_3(\text{CH}_2)_3\text{NH}_2$  (0.19M) was neutralized with HI 57% w/w (2mL) resulting in a clear pale yellow solution and then was added to the  $\text{PbI}_2$  solution slowly. The solution was cooled down to  $65^\circ\text{C}$  and kept at that temperature in a closed vial in a sand bath as the stock solution. Two microlitres of this warm supernatant solution were collected and dispensed with a  $10\mu\text{l}$  pipette onto a glass slide placed in an open ambient environment ( $25^\circ\text{C}$ ). Nucleation and growth quickly initiated on the surface of the precursor solution droplet and perovskite thin sheets floating on the solution droplets were obtained within a few seconds up to 30s. This growth process on the surface of the droplet on glass slides can be observed directly under an optical microscope to monitor the progress.

### *Bromide perovskites*

The syntheses of the Pb bromide perovskites proceeds in a similar manner with the Pb iodide perovskites with the difference being the choice of hydrohalic acid, i.e. concentrated HBr vs concentrated HI. In addition, the syntheses are less challenging since we did not attempt to build homologous series by mixing two different cations to fine tune the width of the inorganic layer since the target compounds consist of a single perovskite sheet. The design principle for the material rather focuses on the complexity of the organic cation, as we intentionally opt for asymmetric, bulky cations that could produce significant strain to the inorganic lattice, in search of crystal structures that have distortion that may give rise to a broadband emission. The design principles are based on the known compound  $4\text{AMPPbBr}_4$ , the  $n = 1$  member of the homologous

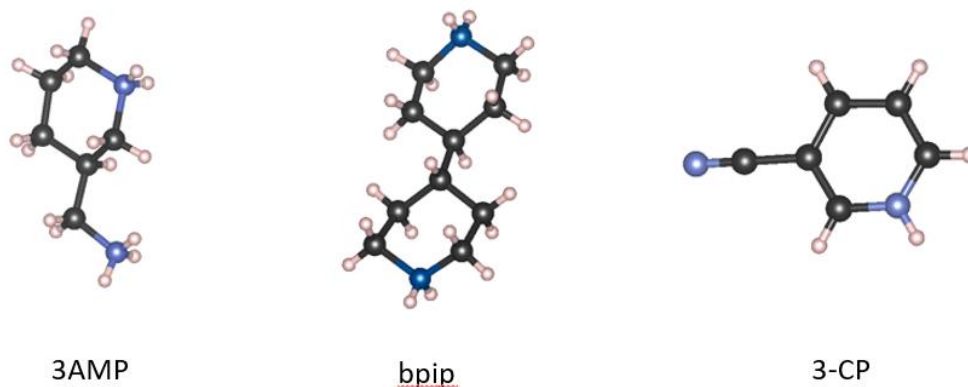


**Figure 10.** Organic cations used in this work. 3AMP = 3-aminomethyl-piperidinium, bpip = 4,4' bipiperidinium, 3CP = 3-cyano-pyridinium

Dion-Jacobson perovskite series  $4\text{AMP}(\text{A})_{n-1}\text{Pb}_n\text{Br}_{3n+1}$ , which exhibits a broadband spectrum.<sup>76,77</sup> Using 4-aminomethyl-piperidinium (4AMP) as the basis, we designed a series of compounds that possess similar cations, with subtle differences on the position of the positive charges (i.e. the ammonium groups) that could tweak the fine structural details in the perovskite layers. These cations are 3-aminomethyl-piperidinium (3AMP), 4,4' bipiperidinium (bpip) and 3-cyano-pyridinium (3CP) and are shown in Figure 10. The first two are closely related to 4AMP including an aliphatic ring that typically obtain a chair conformation, although this can be interchangeable with a boat configuration in the reaction solution. 3CP has a completely different design, since it places the positive charge on a flat aromatic pyridinium ring, with the addition of a strong electron withdrawing -CN group “destabilizing” the regular arrangement of the cations between the perovskite layers. The piperidinium based compounds obtained from this approach possess a 2D perovskite with a formula of  $\text{APbBr}_4$ , whereas the pyridinium based system, which also has a different cationic charge, stabilizes the  $3\text{CPPbBr}_3$  compound which is the first hybrid example of the post-perovskite layered structure.



## 2.2 Characterization

### *Powder X-ray diffraction (PXRD)*

PXRD measurements were performed on a Bruker D8 Advance XRD system using Cu K $\alpha$  radiation ( $\lambda = 1.5406 \text{ \AA}$ ). The samples were mounted on glass in powder form and the data were obtained for angles  $2\theta = 2^\circ - 60^\circ$ .

### *UV-Vis-NIR*

Optical diffuse-reflectance spectra were collected at room temperature using Shimadzu UV-3600 PC double-beam double-monochromator spectrometer operating in the 185–1400 nm region on powdered samples using BaSO<sub>4</sub> as a 100% reflectance reference. The band-gap of the samples was estimated by converting the reflectance to absorption according to the Kubelka–Munk equation:  $K/S = (1 - R)^2 / (2 * R)$ , where R is the reflectance and K and S are the absorption and scattering coefficients, respectively.

### *Photoluminescence*

#### *Iodide perovskites*

Photoluminescence spectra were collected on oriented rectangular crystals of (BA)<sub>2</sub>(MA)<sub>n-1</sub>Pb<sub>n</sub>I<sub>3n+1</sub> (n=1,2,3,4) using Acton SP2500 spectrometer (150 g/mm grating) equipped with a diode CW laser (404nm, 100mW) and Pylon CCD camera. The incident beam was parallel to the (010) direction of the crystal and focused at  $\sim 1 \mu\text{m}$  spot size. Unless stated otherwise the maximum power output of the laser source was filtered to  $300 \mu\text{W}$ .

#### *Bromide perovskites*

Photoluminescence excitation spectra were measured using the Agilent Cary Eclipse spectrofluorometer. The sample was fixed in a quartz dewar in the cuvette compartment of the spectrofluorometer. Photoluminescence spectra were obtained with 365 nm excitation, and photoluminescence excitation spectra were recorded at 510 nm. The emission slit width was 5 nm, and the excitation slit width was 2.5 nm.

# PART 1

The crystal growth of 2D Ruddlesden-Popper-type perovskites  $(\text{BA})_2(\text{MA})_{n-1}\text{Pb}_n\text{I}_{3n+1}$  ( $\text{BA}^+ = \text{CH}_3(\text{CH}_2)_3\text{NH}_3$ ,  $\text{MA}^+ = \text{CH}_3\text{NH}_3$ ;  $n=1-4$ ) of suitable spatial dimensions and optical quality for use in distributed Bragg reflectors (DBRs) microcavities, towards polaritonic applications.

### 3. Results and Discussion

The 2D  $(\text{CH}_3(\text{CH}_2)_3\text{NH}_3)_2(\text{CH}_3\text{NH}_3)_{n-1}\text{Pb}_n\text{I}_{3n+1}$  family of perovskite compounds ( $n = 1-4$ ) was synthesized from a stoichiometric reaction between  $\text{PbI}_2$ ,  $\text{CH}_3\text{NH}_3\text{I}$  (MAI), and *n*-butylamine (BA). A homogeneous solution of concentrated,  $\text{I}_2$ -free hydroiodic acid-containing stoichiometric amounts of  $\text{PbI}_2$  and  $\text{CH}_3\text{NH}_3\text{I}$  (MA), according to the desired composition, was allowed to react with half the stoichiometric amount of BA by addition of the neutralized base into the boiling acid solution under vigorous stirring. This highly exothermic reaction resulted in the formation of a clear, bright yellow solution, which upon cooling to ambient conditions precipitates into the layered perovskite compounds ( $n = 2-4$ ) in the form of colorful rectangular plates with the spectral range spanning from red to black (Figure 11). We find that the use of BA as the reaction limiting reagent is essential in obtaining the compounds in pure form; at the same time, it is detrimental to the reaction yield, which is limited to  $\sim 50\%$  based on the total Pb content due to the high solubility of  $\text{CH}_3\text{NH}_3\text{PbI}_3$  in the  $\text{HI}/\text{H}_3\text{PO}_2$  solvent medium.

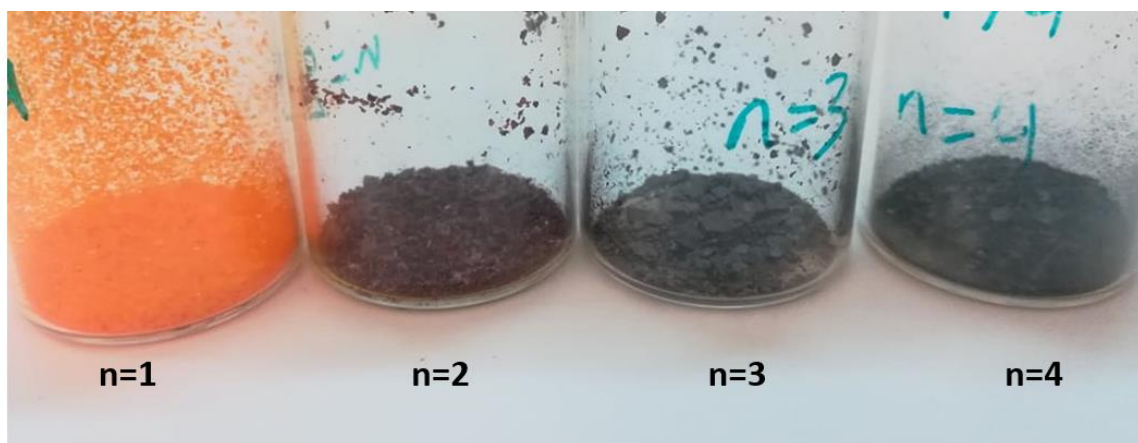


**Figure 11.** Image of  $(\text{CH}_3(\text{CH}_2)_3\text{NH}_3)_2(\text{CH}_3\text{NH}_3)_{n-1}\text{Pb}_n\text{I}_{3n+1}$  ( $n = 1-4$ ) crystals.

As the 2D perovskite layers grow thicker by introducing MA cations in the crystal structure, the unit cell incrementally expands by the addition of a single perovskite layer at a time. These changes in the unit cell can be monitored by X-ray diffraction (XRD), which characteristically reveals an additional low angle reflection for each added perovskite layer (Fig. 12).

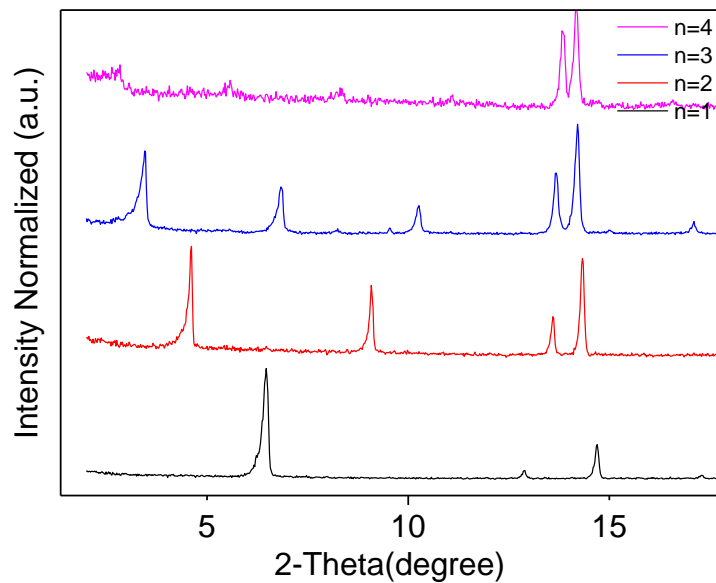
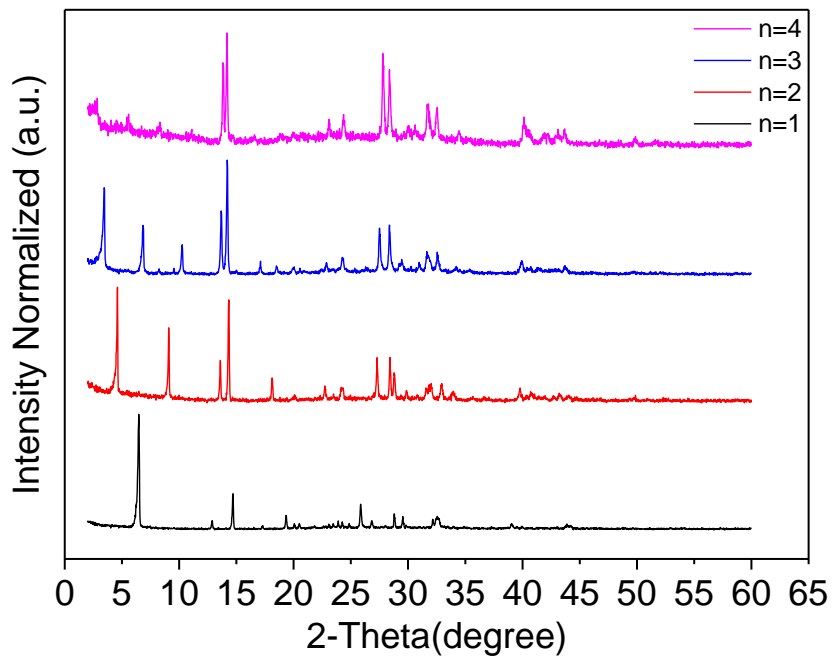


**Figure 12.** X-ray diffraction patterns of the  $(\text{BA})_2(\text{MA})_{n-1}\text{Pb}_n\text{I}_{3n+1}$  ( $n=1-4$ ) perovskites. Bulk powder diffraction and close-up views of the characteristic regions between  $2\theta = 2-15^\circ$ .

***Basic structural characteristics.*** The crystal structures of the  $(\text{BA})_2(\text{MA})_{n-1}\text{Pb}_n\text{I}_{3n+1}$  ( $n=1-4$ ) compounds are shown in Figure 13. Each 2D inorganic layer relates to the tetragonal parent 3D compound ( $n = \infty$ ) by slicing the perovskite along the (110) plane such that some of the oriented MA cations are partially ( $n = 2, 3, 4$ ) or fully ( $n = 1$ ) substituted by the terminal BA cations. Similar to the parent compound, the layers consist of tilted, corner-sharing  $[\text{PbI}_6]^{4-}$  octahedra that propagate in two directions (the ac plane), whereas in the third dimension (the b-axis), the octahedral sheets are physically disconnected by the intercalated organic bilayers.

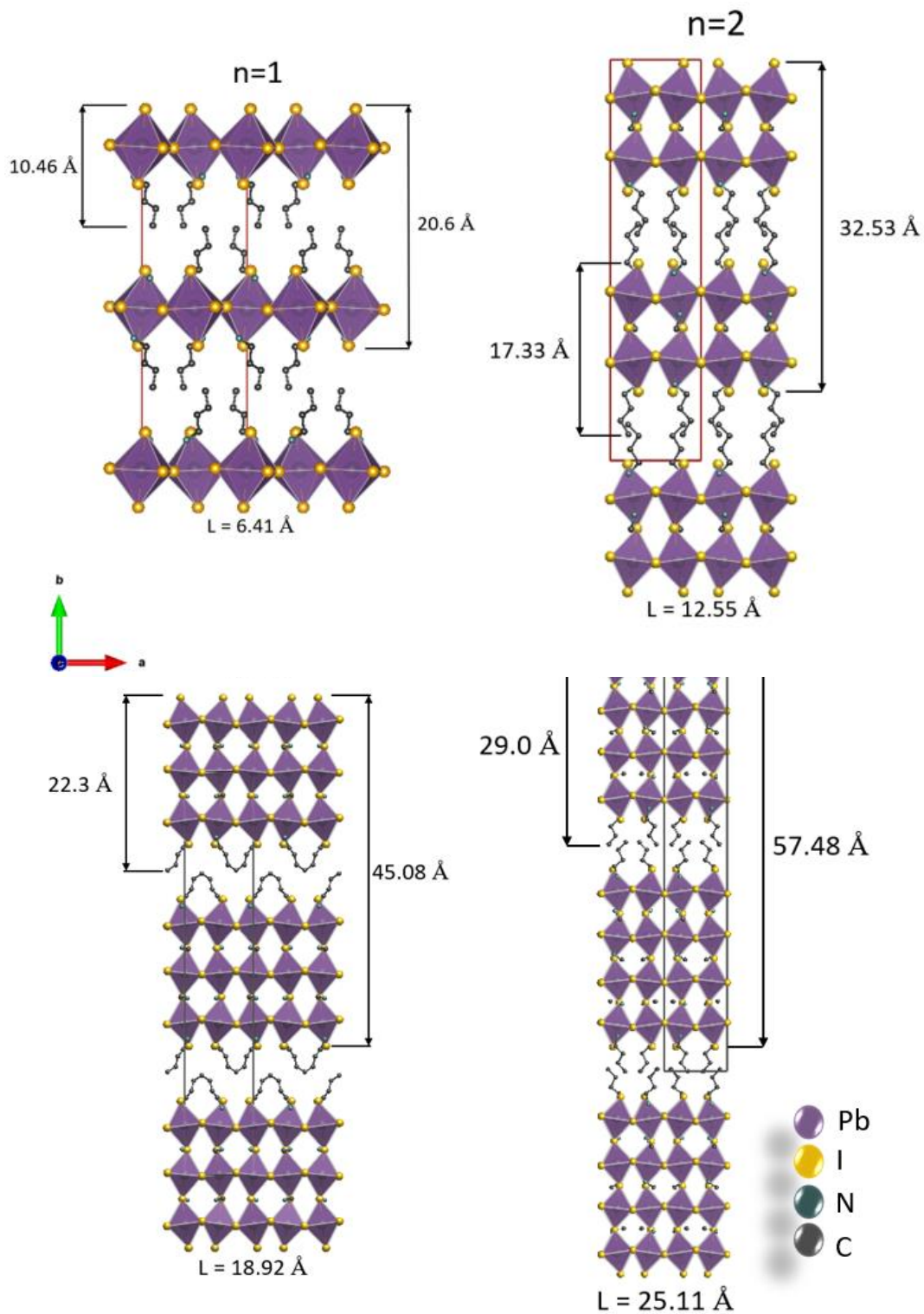


**Figure 13.** Crystal structures of the lead iodide perovskites,  $(\text{BA})_2(\text{MA})_{n-1}\text{Pb}_n\text{I}_{3n+1}$  ( $n=1-4$ ). The L-value denotes the thickness of the inorganic layer in each compound. The numerical values refer to the distance between the terminal iodide ions of each layer and were determined directly from the refined crystal structures.

**Band gaps and photoluminescence.** Figure 14 displays the room temperature absorption and photoluminescence spectra of bulk samples from the  $(\text{BA})_2(\text{MA})_{n-1}\text{Pb}_n\text{I}_{3n+1}$  ( $n=1-4$ ) series. From the experimental spectra, we assign the higher energy absorption edge to the bandgap of the materials (Table 1). The sharp nature of the absorption edges points toward a direct bandgap in all compounds. After the primary absorption edge, it is easy (in most components) to observe a second peak with strong intensity for the  $n=1$  compound which attenuates as the thickness of the inorganic layers increases (Figure 14a). The presence of the secondary, molecular-like absorption in the optical absorption spectra of these compounds, suggests the presence of stable excitons even at room temperature.

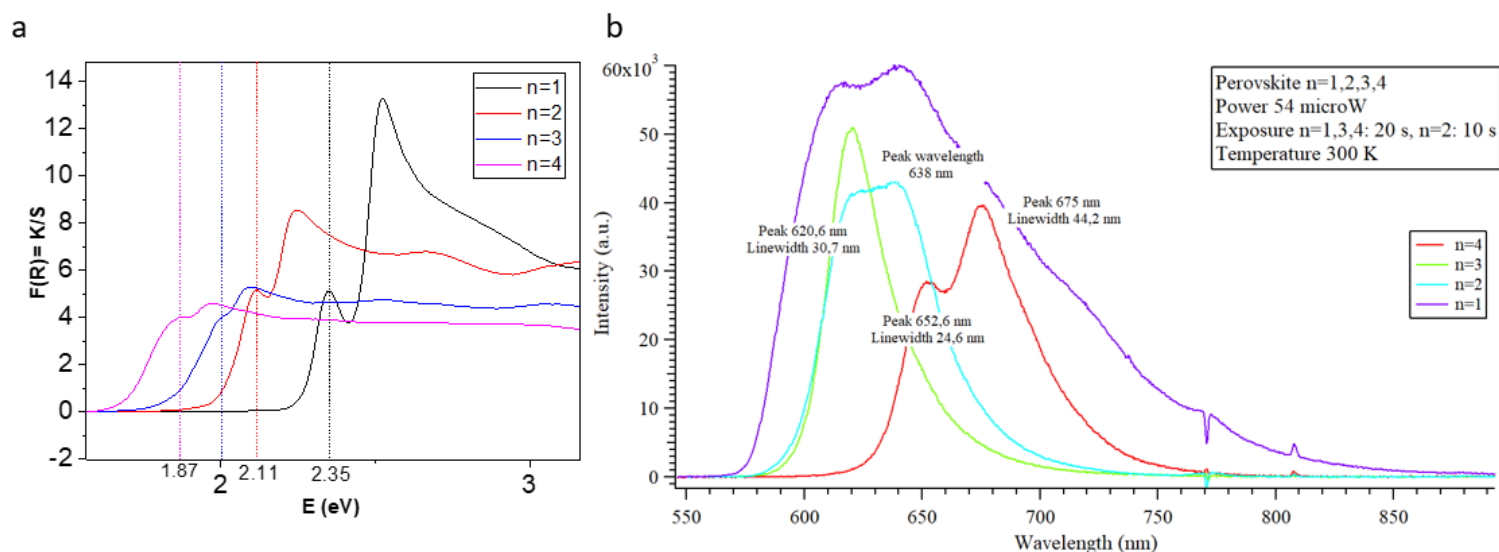


**Figure 14** Optical properties of the  $(\text{BA})_2(\text{MA})_{n-1}\text{Pb}_n\text{I}_{3n+1}$  perovskites (for  $n = 1, 2, 3, 4$ ). (a) Optical absorption of polycrystalline samples obtained from diffuse reflectance measurements converted using the Kubelka–Munk function ( $K/S = (1 - R)^2 / 2R$ ). (b) Photoluminescence of oriented crystals with the wide planar facets oriented perpendicular to the laser beam ( $\lambda_{\text{exc}} = 404 \text{ nm}$ ).

<i>Compound</i>	<i>Bandgap <math>E_g</math> (eV)</i>	<i>Excitonic absorption (eV)</i>	<i>Photoluminescence PL (eV)</i>
$(\text{BA})_2\text{PbI}_4$	2.47	2.35	2.07
$(\text{BA})_2(\text{MA})\text{Pb}_2\text{I}_7$	2.19	2.11	1.94
$(\text{BA})_2(\text{MA})_2\text{Pb}_3\text{I}_{10}$	2.05	2.03	2.02
$(\text{BA})_2(\text{MA})_3\text{Pb}_4\text{I}_{13}$	1.93	1.87	1.83

**Table 1.** Optical parameters of the  $(\text{BA})_2(\text{MA})_{n-1}\text{Pb}_n\text{I}_{3n+1}$  perovskites

Unlike the absorption spectra, which are characterized by an absorption edge and an excitonic peak, the photoluminescence spectra consist of one single emission peak corresponding to the energy value of the excitonic peak in the absorption spectra. This is because the relaxation pathway is dictated by direct radiative recombination of an exciton, typical for an excitonic material. In Figure 13b it is obvious that not all samples have a single emission peak as we expected. This is due to phase impurities and poor crystallization. The most consistent compound was the  $(\text{BA})_2(\text{MA})_2\text{Pb}_3\text{I}_{10}$  ( $n=3$ ) which always presented a single quite sharp emission peak. This is why we proceeded only with this compound for all of our following measurements and deposition in a cavity.

**Comparison of the two synthetic methods for the  $(\text{BA})_2(\text{MA})_2\text{Pb}_3\text{I}_{10}$  ( $n=3$ ).** Since the quality of the samples needs to be able to reach not only chemical quality (phase purity) but also optical quality (single wavelength emission), several synthetic procedures were developed during the Thesis. The first method was the **solution process method (SP)** is a synthetic method that uses the BA as the reaction limiting reagent to obtain the compounds in pure form. Because of the randomness of the crystallization, the crystals are not very consistent in shape and size and they form aggregates. SEM images of typical crystals from the SP process are shown in Figure 15.

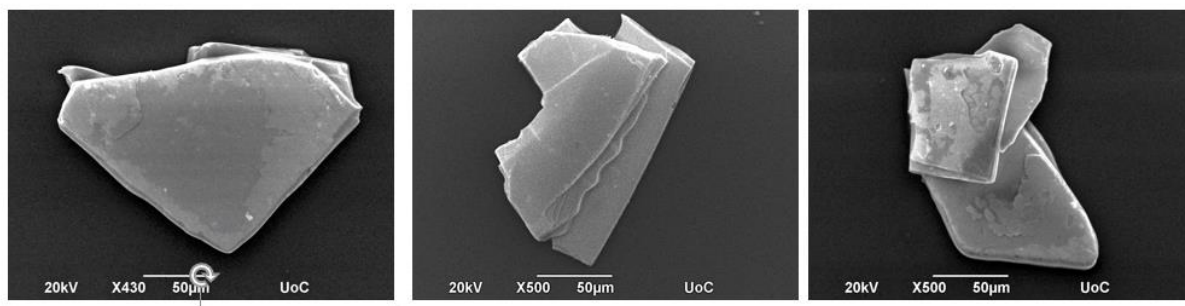


**Figure 15.** SEM images of  $(\text{BA})_2(\text{MA})_2\text{Pb}_3\text{I}_{10}$  ( $n=3$ ) crystals, formed with SP synthetic method.

The PL emission of these crystals is generally very good and quite sharp only after mechanical or chemical exfoliation of the original crystals to extract more thin and well-shaped new ones (Figure 16a,b).



## SOLUTION PROCESS METHOD (SP)

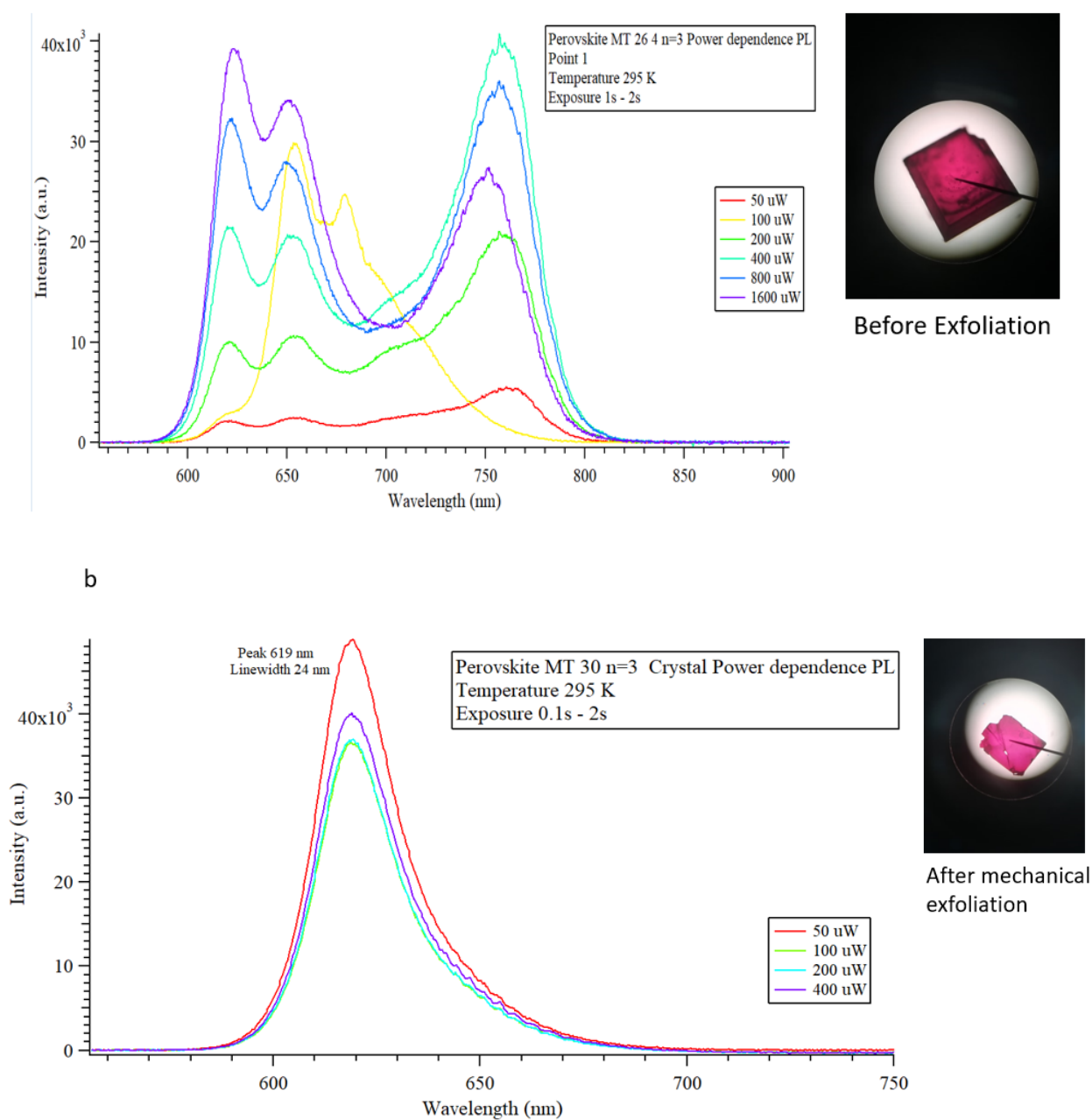


**Figure 16.** PL spectra of a  $(\text{BA})_2(\text{MA})_2\text{Pb}_3\text{I}_{10}$  ( $n=3$ ) crystal-synthesized with SP. (a) before exfoliation. (b) after exfoliation

In Figure 16a the PL of the “bulk” crystal features an additional peak at a lower energy of the exciton emission energy. In this phenomenon part of the photogenerated exciton population travel to the edges of the crystal within its diffusion time, and then undergoes an internal conversion to a layer-edge-state and efficiently emits photons at a lower energy than the main exciton.<sup>78</sup> By exfoliating the crystals we manage to decrease the edge-states to minimize the exciton loses and have a localized exciton population (Figure 16b).

The **floating growth method (FG)**, includes a saturated aqueous solution containing perovskite precursors dissolved in concentrated hydroiodic acid which is dropped onto a glass. The droplet becomes supersaturated upon cooling, initiating nucleation and crystal growth on the surface of the droplet. With this method, the crystals that are forming are more consistent both in shape and size counter to the SP method (Figure 17a,b). The PL spectra are as good as the previous one but the positive thing is that no exfoliation is needed to achieve the same PL results (Figure 17c).

### FLOATING GROWTH METHOD (FG)

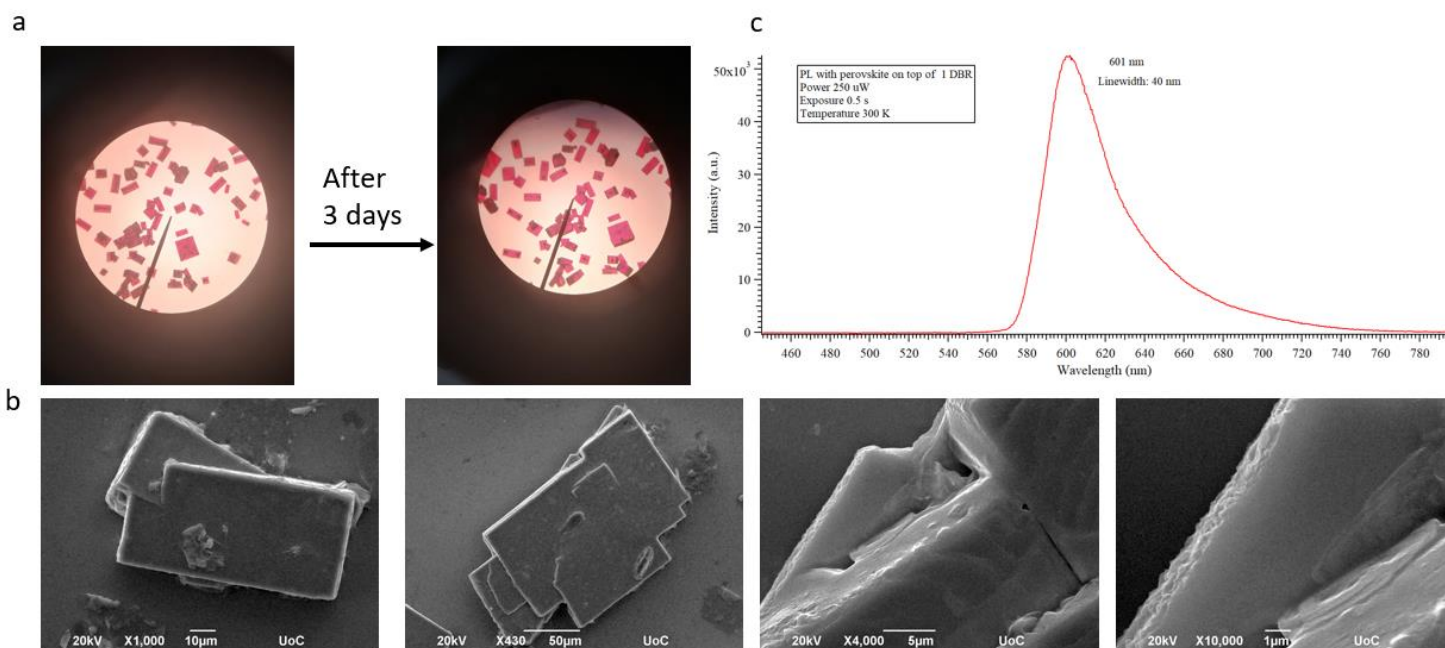


**Figure 17.** (a) images of  $(\text{BA})_2(\text{MA})_2\text{Pb}_3\text{I}_{10}$  ( $n=3$ ) crystals synthesized with FG a few seconds after the droplet hit the glass surface. (b) SEM images of the same crystals 3 days after. (c) PL spectra of crystals formed on a droplet deposited directly on a DBR.

**Deposition in DBR cavity.** The final step was to encapsulate a perovskite layer between two DBRs to form a microcavity. We measured the reflectivity of a single DBR (no cavity) and two DBRs sandwiched together with no extra material in between. In figure 18 the blue line represents the reflectivity of a single DBR which reflects in the region of  $\lambda=550-750$  nm. The red line represents the reflectivity of 2 DBRs with no material between them. The 3 peaks that are shown in the graph are called modes (constructive interference of photons in specific wavelengths depending on their optical path) made in the cavity formed by the trapped air between the two DBRs. Unfortunately, by incorporating the perovskite (synthesized with **SP method**) between the DBRs we couldn't observe any modes inside the cavity (Figure 19). The size of the perovskite is the most probable reason for the absence of modes. For a mode to appear the two DBRs should be perfectly parallel to each other and very close ( $\sim 200$ nm). As shown by the SEM images (Figure 15) the crystals are very uneven and way thicker than we need. This results in a not very transparent medium that absorb and reflects the photons but doesn't transmit so the light is not reflected by both DBRs, and the photons don't interact with each other to form a mode.

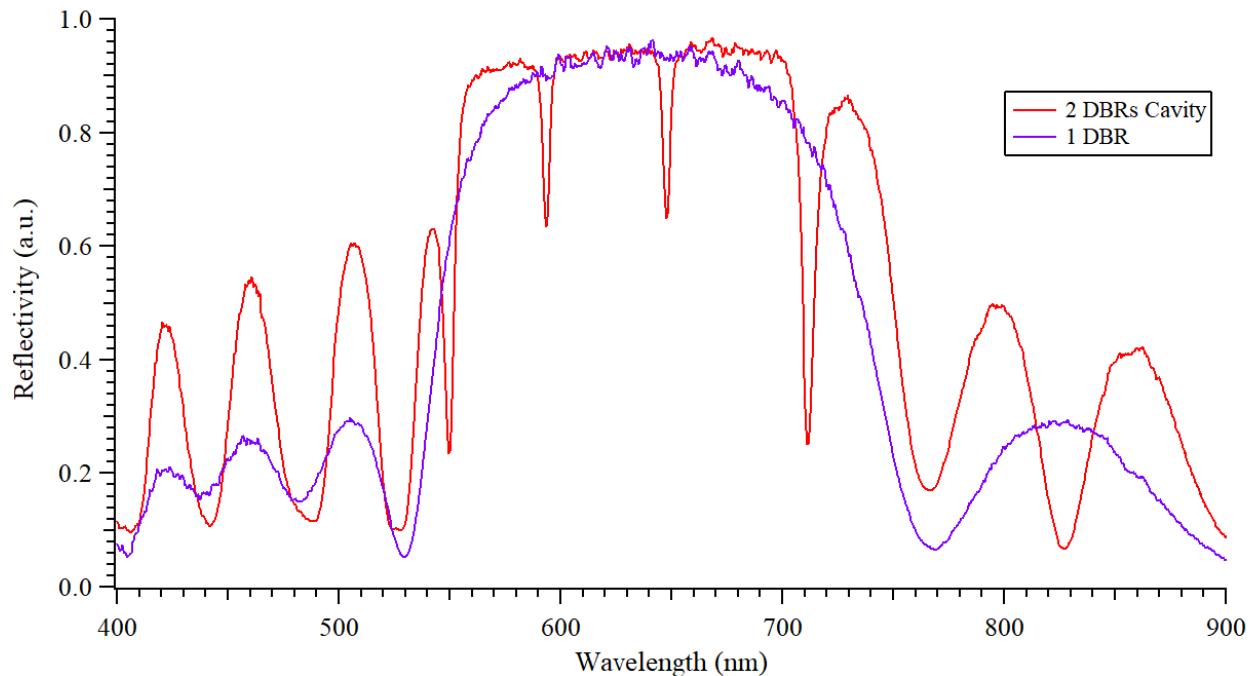


**Figure 18.** Reflectivity spectra of a single DBR (blue line) and two DBRs sandwiched (red line).

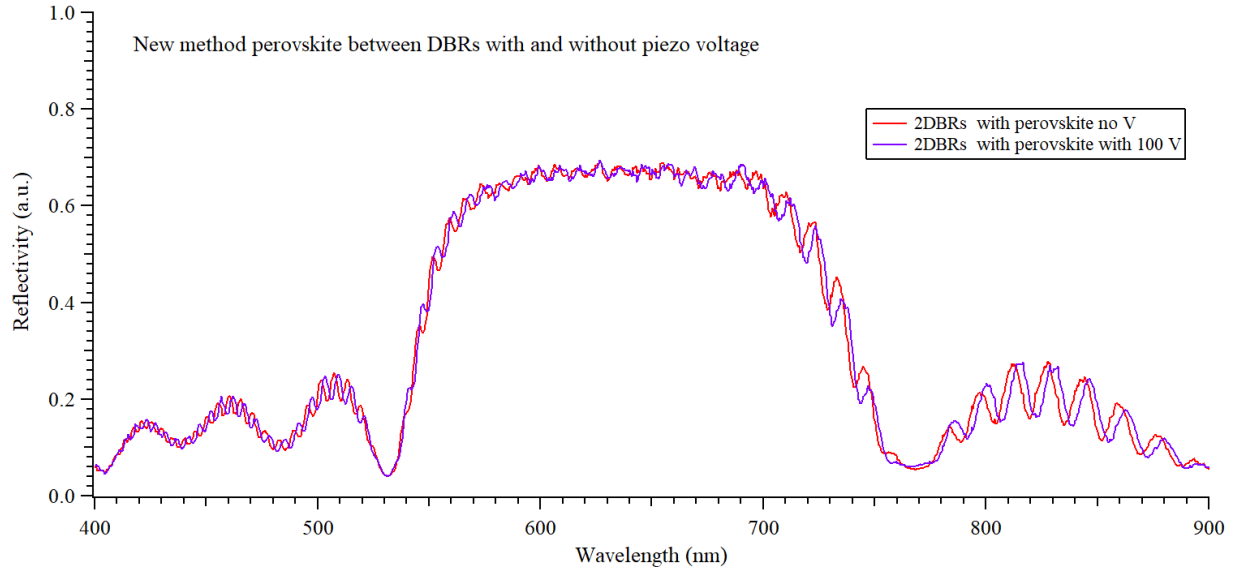


**Figure 19.** Reflectivity spectra of a perovskite (SP method) sandwiched between two DBRs.

On the contrary, by incorporating the perovskite (synthesized with **FG method**) between the DBRs we clearly observe many modes inside the cavity (Figure 20). Ideally, we want to reduce the number of modes that are created, which means that all the photons will interfere at the same wavelength, boosting the intensity of the peak. If we achieve one mode with high reflectivity it will be easier then to interact with the exciton and combine into a polariton. Because with this method formation of the crystals initiates vary fast when the hot droplet touches the cold (RT) DBR when we put the second DBR on top, some crystals were already beginning to form. This resulted in some minor anomalies which is why we don't have an absolute parallel DBR stacking. This is probably the reason for the multiple peaks in the reflectance spectra. By heating the DBRs prior to the droplet deposition, we managed to delay the cooling of the droplet just enough to put the second DBR on top before the crystallization process begins. The DBR-perovskite-DBR system was then placed in a homemade mount designed to exert pressure on the DBRs so that the crystals formed between them will be as thin as possible (Figure 21). This improved the cavity mode as show in Figure 22.

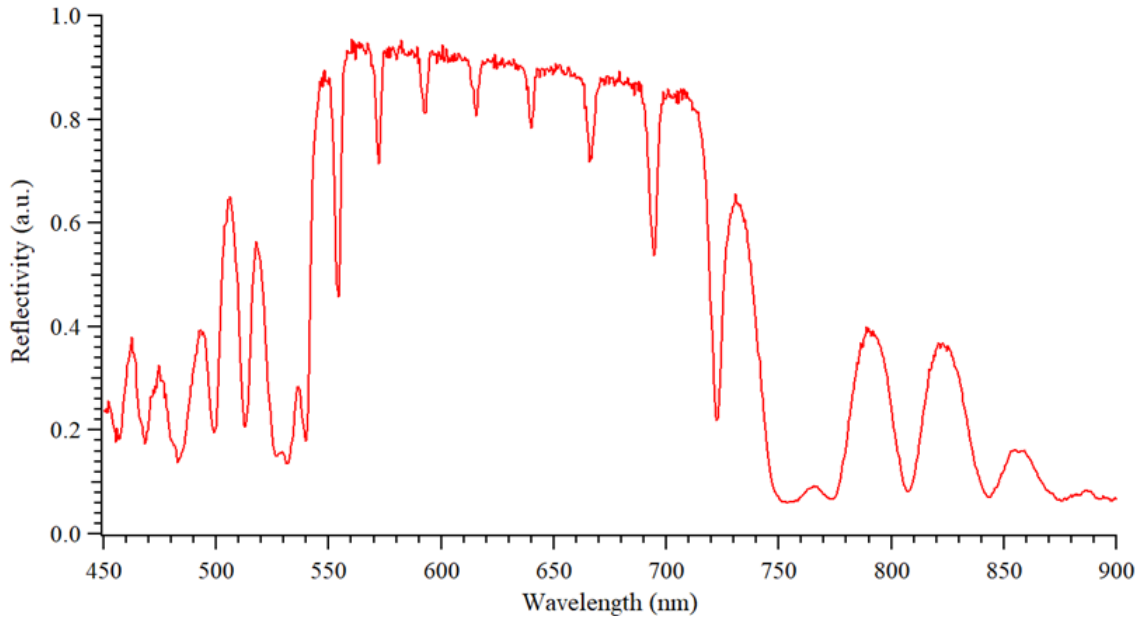


**Figure 20.** Reflectivity spectra of a perovskite (FG method) sandwiched between two (room temperature) DBRs

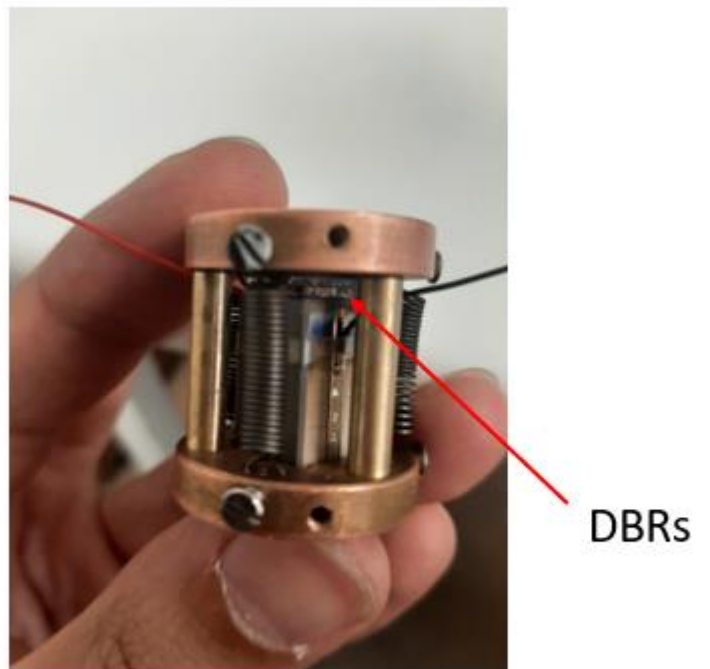


**Figure 21.** Picture of the mounting mechanism.

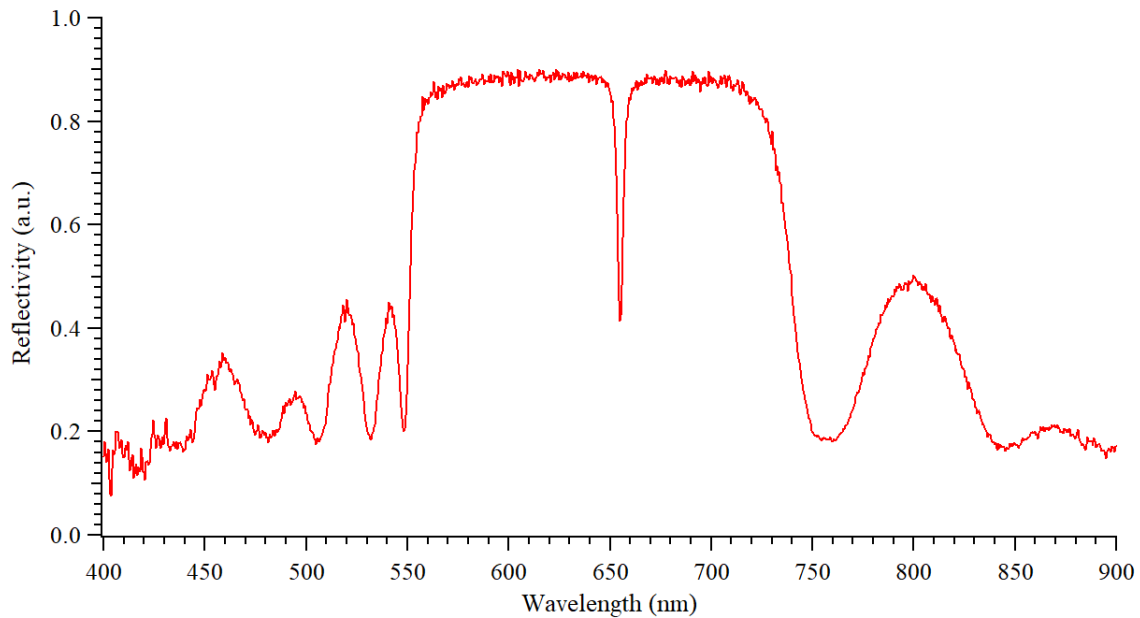


**Figure 22.** Reflectivity spectra of a perovskite (FG method) sandwiched between two (hot,  $\sim 80^{\circ}\text{C}$ ) DBRs

The next step was to check the system for the formation of a polariton. In Figure 23 we did a reflectivity scan of different points of the perovskite cavity. The pattern that we observed in this measurement, is that as we “walk” the cavity mode closer to the exciton region (620 nm) there are some points with 2 peaks at the same time without any combination. This could be explained as the photons get closer to the excitons they interact through strong orbit coupling (SOC) and form a polariton. Further dispersion measurements (Figure 24) show a slight bending at the edges of the mode when it interacts with the exciton at 620 nm. This is another intication of possible polariton formation. These last data are still not very clear to us and deeper analysis is beyond the scope of this thesis. Since the cavity formation with the perovskite was successful and there are indications of the formation of polaritons the first step for the optimization of the perovskite is completed. Further investigation and characterization on the polariton formation is needed.

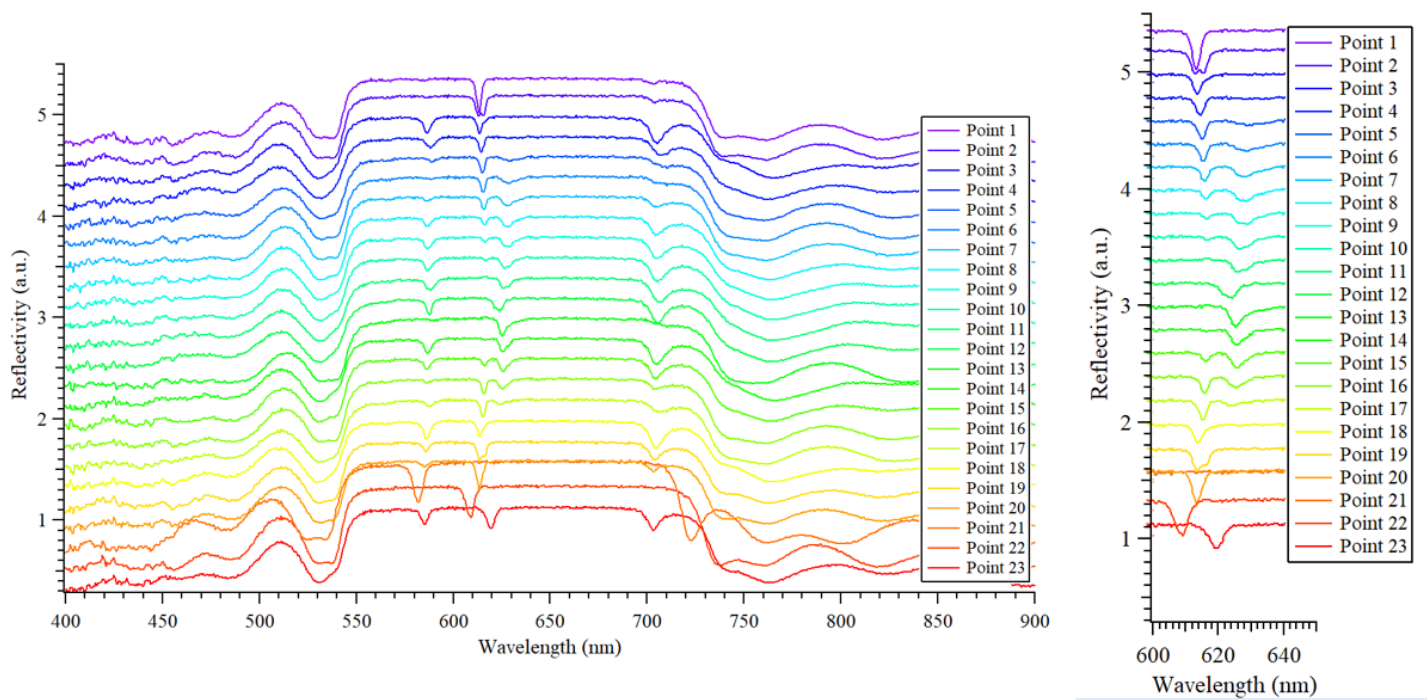


**Figure 23.** Reflectivity scans around the cavity.

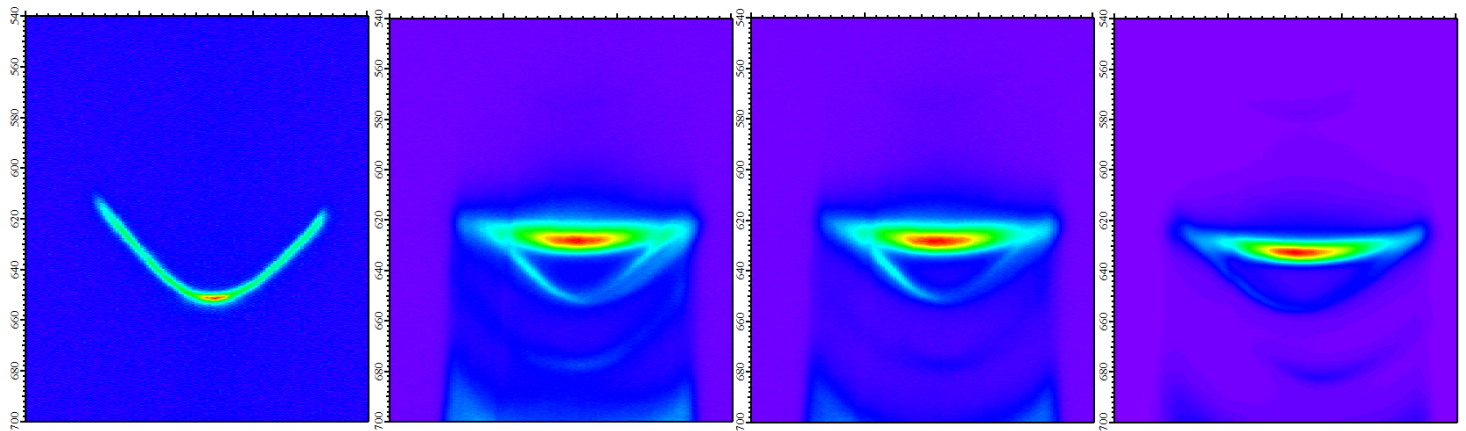


**Figure 24.** Dispersion measurements

## PART 2

Exploratory synthesis of  $\text{APbBr}_4$  ( $\text{A}^{2+}$  = piperidinium-based ammonium dications) 2D Dion-Jacobson type perovskites as single-component white-light emitters.



## 4. Results and Discussion

In 2018, Mao et al. first reported multilayer structures of 2D halide DJ perovskites (xAMP)-(MA)<sub>n-1</sub>PbnI<sub>3n+1</sub> (AMP = (aminomethyl)piperidinium, x = 3 or 4, n = 1–4).<sup>79</sup> The dications are less symmetrical than most spacers discussed in the session above, with one primary N and another N on the piperidine ring. The position of the functional group has a profound influence on the structure and properties of the resulting 2D perovskite structure. Since the inorganic layers are stacked exactly on top of each other with no lateral shift, the distance between adjacent layers defined by the planes of terminal iodine atoms can simply be measured by the closest I···I distance. Both series exhibit a short interlayer distance of ~4 Å, with the 3AMP series showing a slightly smaller distance than the 4AMP because the position where each one connects with the octahedra is different. The 3AMP cation shows weak interaction with the terminal iodine atoms, which exhibits a small effect on the in-plane Pb–I–Pb angle. While 4AMP seems to interact in a stronger fashion where the hydrogen bonding with bridging iodine atoms causes amplified in-plane distortion but negligible out-of-plane distortion (Figure 25).

### 4.1 Crystal Structures

The hybrid lead bromide compounds presented here cover the Dion-Jacobson (3AMP, 4AMP, bpip) and post-perovskite (3CN) structural types. All the crystal structures crystallize in noncentrosymmetric spacegroups in the relatively low symmetry monoclinic (3AMP, bpip, 3CP) and orthorhombic (4AMP) crystal systems (Table 2, see also Appendix).

<i>Cations</i>	<i>Formula</i>	<i>Dimensionality</i>	<i>Space group</i>	<i>Connectivity modes</i>	<i>Bandgap (eV)</i>
<b>3amp</b>	(C <sub>6</sub> H <sub>16</sub> N <sub>2</sub> )PbBr <sub>4</sub>	2D	Cc	Corner-sharing	3.0
<b>4amp</b>	(C <sub>6</sub> H <sub>16</sub> N <sub>2</sub> )PbBr <sub>4</sub>	2D	Pca2 <sub>1</sub>	Corner-sharing	3.1
<b>bpip</b>	(C <sub>10</sub> H <sub>20</sub> N <sub>2</sub> )PbBr <sub>4</sub>	2D	Pc	Corner-sharing	2.9
<b>3cp</b>	(C <sub>6</sub> H <sub>16</sub> N <sub>2</sub> )PbBr <sub>4</sub>	2D	C2/m	Corner- and edge-sharing	3.0

**Table 2.** Summary of structural characteristics of (3amp)PbBr<sub>4</sub>, (4amp)PbBr<sub>4</sub>, (3cp)PbBr<sub>3</sub>, (bpip)PbBr<sub>4</sub>

### **Piperidinium-based Dion-Jacobson crystal structures.**

**(Aminomethyl)piperidinium structures:** The crystal structure of the  $x$ -AMPPbBr<sub>4</sub> ( $x = 3, 4$ ) is shown in Figure 25. They both consist of infinite {PbBr<sub>4</sub>}<sup>2-</sup> layers of corner connected octahedra. All the octahedra are nearly regular (Table XXX) and the major variation arises from the degree of tilting between them. In both compounds, tilting occurs both in the lattice plane (in-plane tilting) and outside of it (out-of-plane tiling) with the second factor being of great importance to the spectral properties according to a recent study by Smith et al.<sup>71</sup> The reason for the increased out-of plane tilting in 3AMPPbBr<sub>4</sub> is directly related to the arrangement of the organic dications between the perovskite stacks where we can observe two major differences: i) the up-down arrangement of the -CH<sub>2</sub>NH<sub>3</sub>/<sup>-</sup>(CH<sub>2</sub>)<sub>2</sub>NH<sub>2</sub> (that is the methylammonium and the piperidinium groups, respectively) groups differs in the sense that 3AMP packs in a continuously alternating up-down arrangement between adjacent cations whereas 4AMP prefers an arrangement where the cations pack in pairs with two of them pointing up(down) before switching their orientation down(up) across the perovskite plane. This latter feature leads to a doubling of the unit cell along the crystallographic  $a$ -axis. ii) The position of the piperidinium nitrogen is rotated in 3AMP vs. 4AMP with the former pointing directly towards the axial bromide atoms of the octahedra, forming relatively strong H-bonds (2.8 Å) with it, whereas in the case of 4AMP the nitrogen is pointing directly towards the inter-octahedral voids of the layer, without any obvious H-bonding. The combination of these features introduces much greater strain in 3AMPPbBr<sub>4</sub> compared to 4AMPPbBr<sub>4</sub>, forcing the perovskite lattice to buckle up (or down) with respect to the layer plane. The comparative structural parameters are shown in Table 5-Appendix.

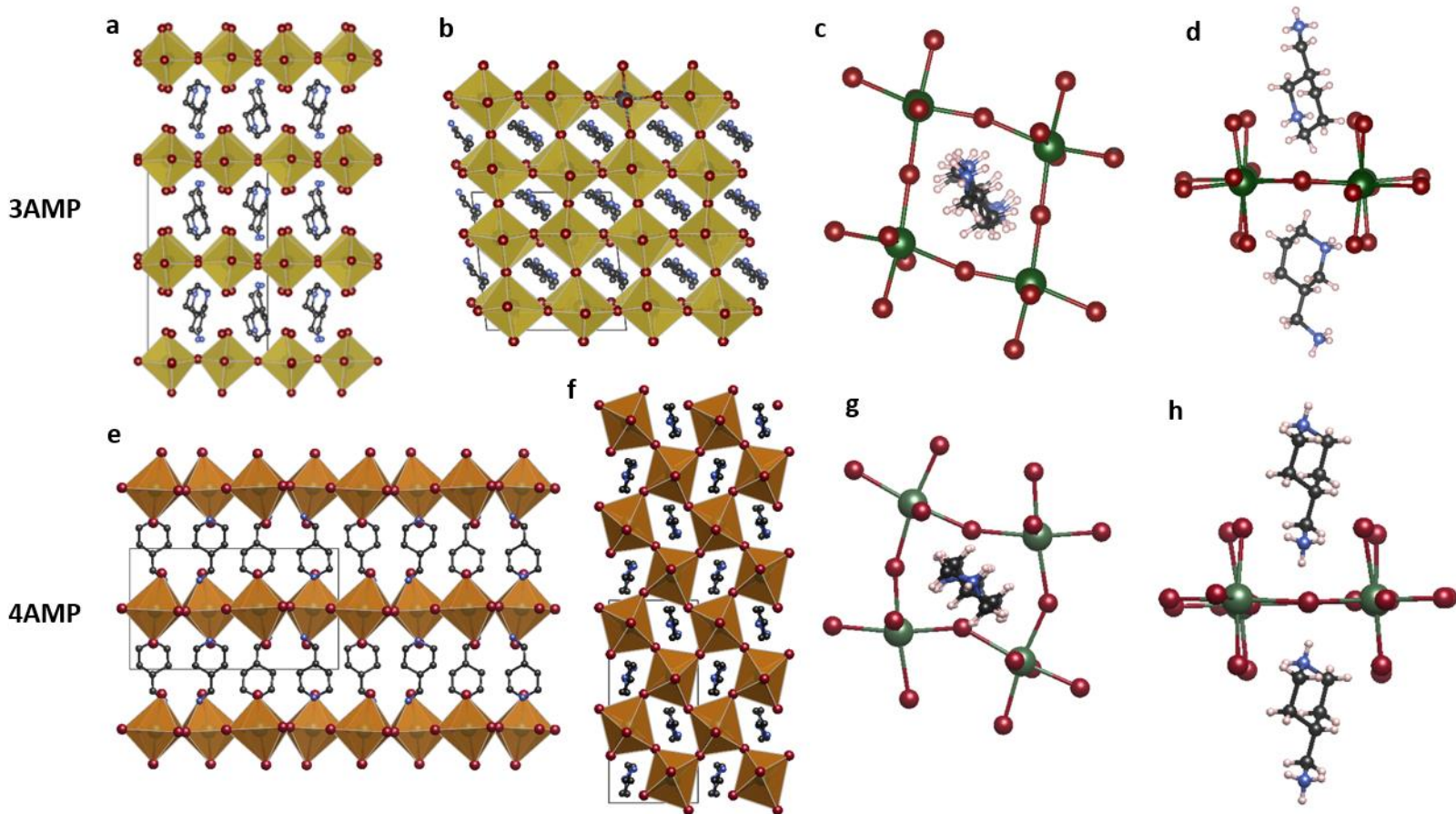


**Figure 25.** Crystal structures of (a-d) (3amp)PbBr<sub>4</sub> and (e-h) (4amp)PbBr<sub>4</sub>. (b), (f) Viewing perpendicular to the layers. (c), (g) In-plane octahedral distortion. (d), (f) out of plane octahedral distortion.

**4,4' bipiperidinium structure.** The crystal structure of (bpip)PbBr<sub>4</sub>, or C<sub>10</sub>H<sub>22</sub>N<sub>2</sub>PbBr<sub>4</sub>, is shown in Figure 26. Similar to the x-AMP compounds, it consists of corner-sharing octahedra, forming the inorganic perovskite layer and 4,4 bipiperidinium cations that fit snugly inside the perovskite lattice pockets. (Figure 26a). This symmetric arrangement of the cations does not produce any out-of-plane tilting but on the other hand the layers suffer from a very intense tilting in the perovskite layer plane (Figure 26c) (Figure 26d). Different from the x-AMP compounds, however, the octahedra seem to be extremely distorted, introducing a strong uncompensated strain in the perovskite lattice (Table 5-Appendix).

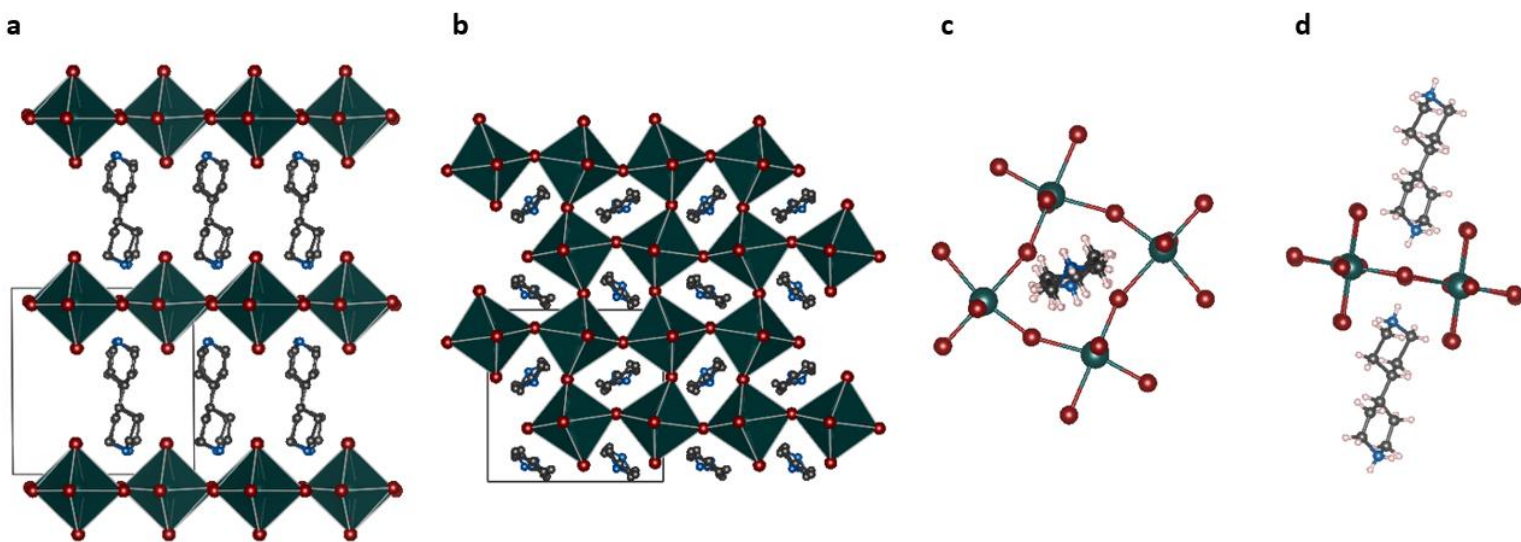


**Figure 26.** Crystal structure of (bip)PbBr<sub>4</sub>. (b) Viewing perpendicular to the layers, (c) In-plane octahedral distortion, (d) out of plane octahedral distortion.

**3-cyanopyridinium cation.** In 2004 a polytype of MgSiO<sub>3</sub> was discovered that exists at a pressure of >125 GPa and a temperature of 2500 K.<sup>80</sup> This phase consists of [SiO<sub>6/2</sub>]<sup>2-</sup> octahedra, forming layers with corner- and edge-sharing connectivity in orthogonal directions across the layers' plane separated by Mg<sup>2+</sup> cations between the layers and was named “post-perovskite.” (3cp)PbBr<sub>3</sub>,

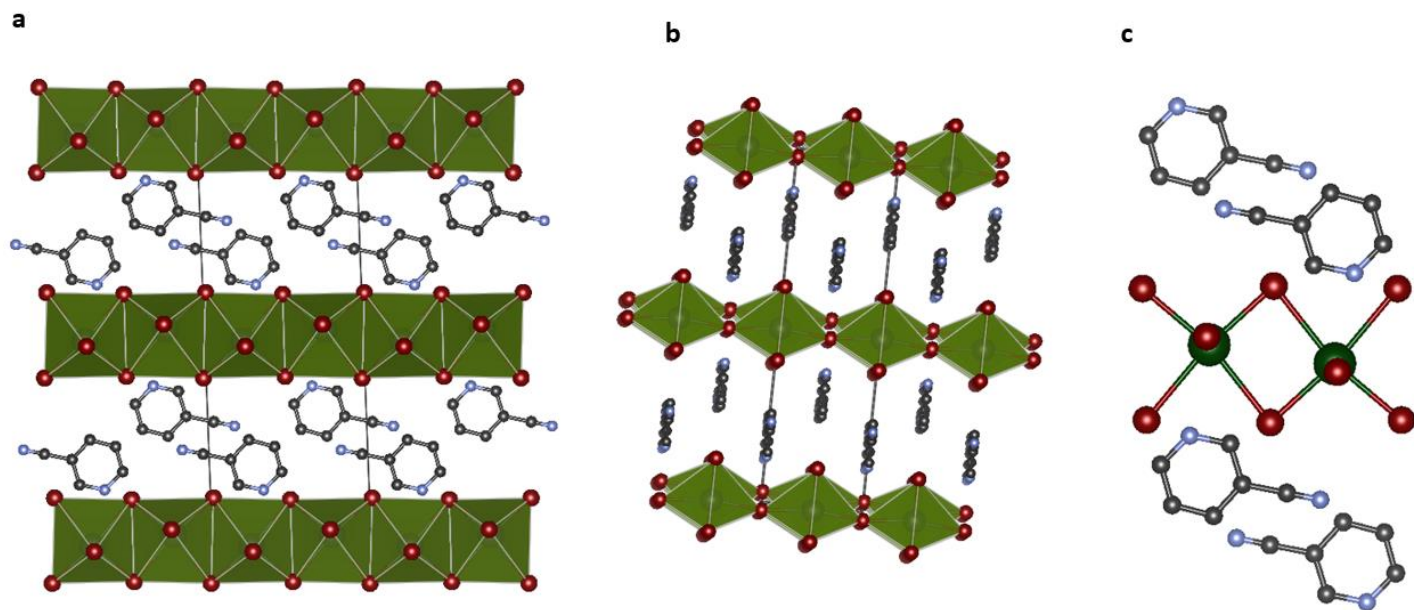


**Figure 27.** Crystal structure of (3cp)PbBr<sub>3</sub> along the (a) y-axis and (b) x-axis. (c) in-plane and out-of-plane octahedra distortion.

where 3cp stands for the 3-cyanopyridinium,  $[3\text{-CN-C}_5\text{H}_5\text{NH}]^+$  cation is the first hybrid organic-inorganic 2D perovskite with post-perovskite structure (Figure 27).<sup>81</sup>

Unlike RP and DJ structures, the distribution of octahedra in  $(3\text{cp})\text{PbBr}_3$  is not uniform in the  $(x,y)$  plane, arranging in “ridges” of edge-shared anions and “grooves” of corner-shared ones along the x-axis (Figure 27a). Such anisotropy results in the perfect ordering of 3-cyanopyridinium cations along the x-axis in the “grooves” with the pyridinium nitrogen atoms being anchored inside the grooves (Figure 27b). The formation of “ribs” in “grooves” is caused by deformation of the  $[\text{BX}_6]$  octahedra, confining the placement of the organic cations along the x-axis. This leads to the doubling of the lattice constant along the x-axis. In this configuration, the  $\text{Pb}^{2+}$  cations are shifted from the octahedra centers (Figure 27#c). The crystal packing of the 3-cyanopyridinium cations in  $(3\text{cp})\text{PbBr}_3$  crystal allows for short interatomic distances between the pyridinium nitrogen atom and bromides. The shortest  $\text{N}\cdots\text{Br}$  distance equal to 3.28 Å allows us to make an assumption about the presence of a hydrogen bond between the corresponding hydrogen and bromine atoms.

## 4.2 Optical Characterization

Optical measurements in room temperature show similar behavior of wide PL emission and high band gap ( $\sim 3\text{eV}$ ) for both (bpip) $\text{PbBr}_4$  and 4AMP $\text{PbBr}_4$  (Figure 28) as we expected from their comparable crystal structure. Temperature dependant PL showed a strange not expected trend. We would expect that as the temperature is getting lower the “edge effect” emission peak will start to faint until fully disappears and only the excitonic peak will be visible. As shown in Figure 29 the peak is still clear even at very low temperatures and it looks like is not affected at all.

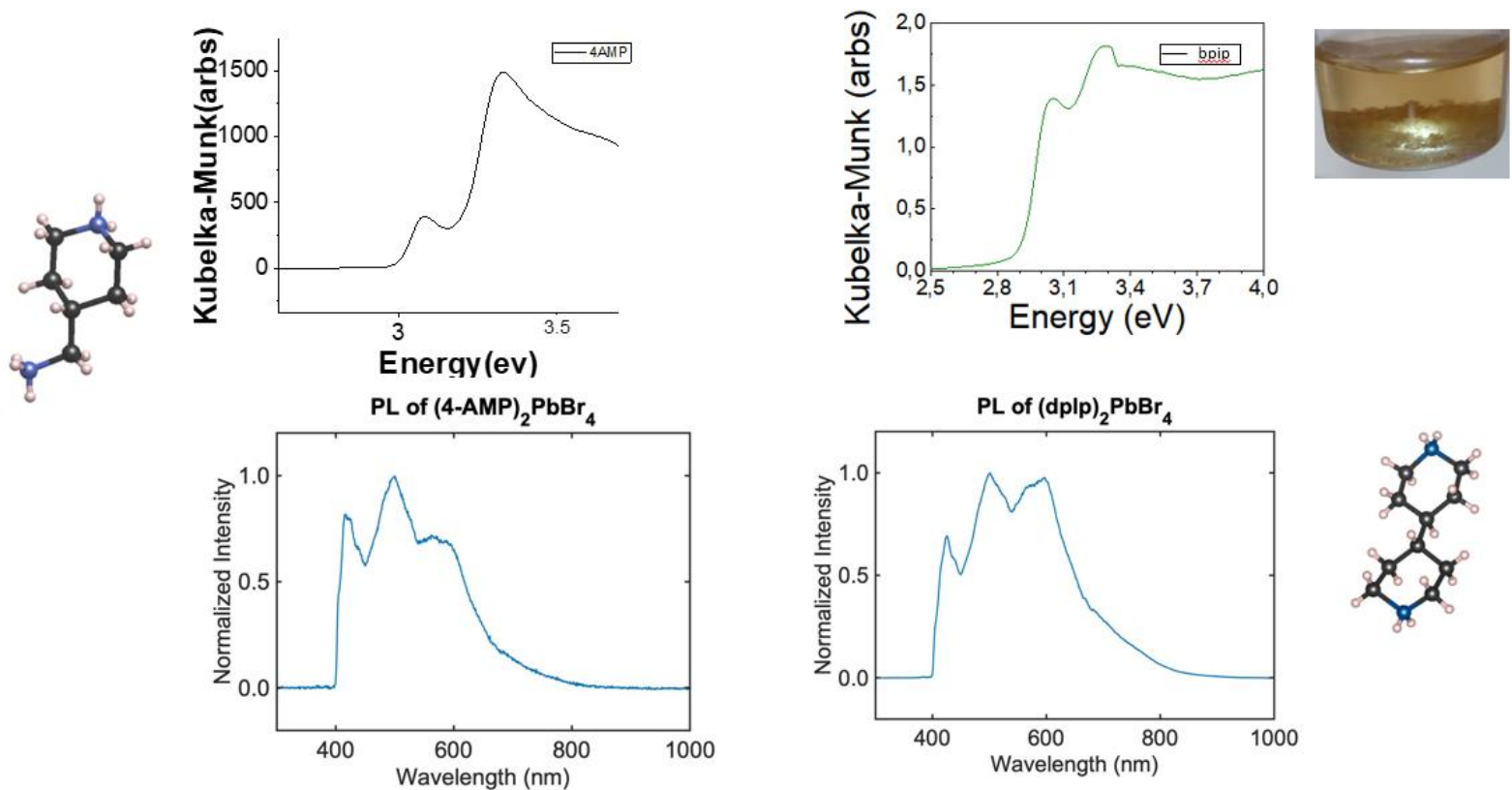


**Figure 28.** Optical absorption and photoluminescence spectra of (4amp) $\text{PbBr}_4$  and (bpip) $\text{PbBr}_4$ .



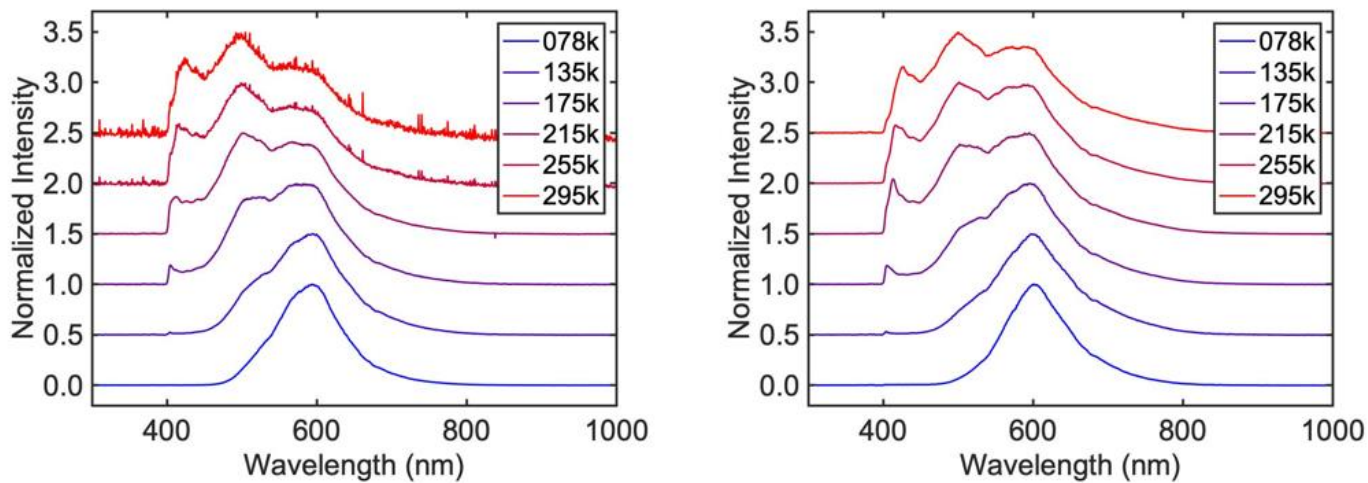


**Figure 29.** Temperature-dependent PL spectra of (4amp)PbBr<sub>4</sub> and (bip)PbBr<sub>4</sub>.

The 3AMPpPbBr<sub>4</sub> displayed an even more unexpected behavior since the PL spectra was much closer to that of a 3D perovskite with a single peak emission than to the other two 2D structures with

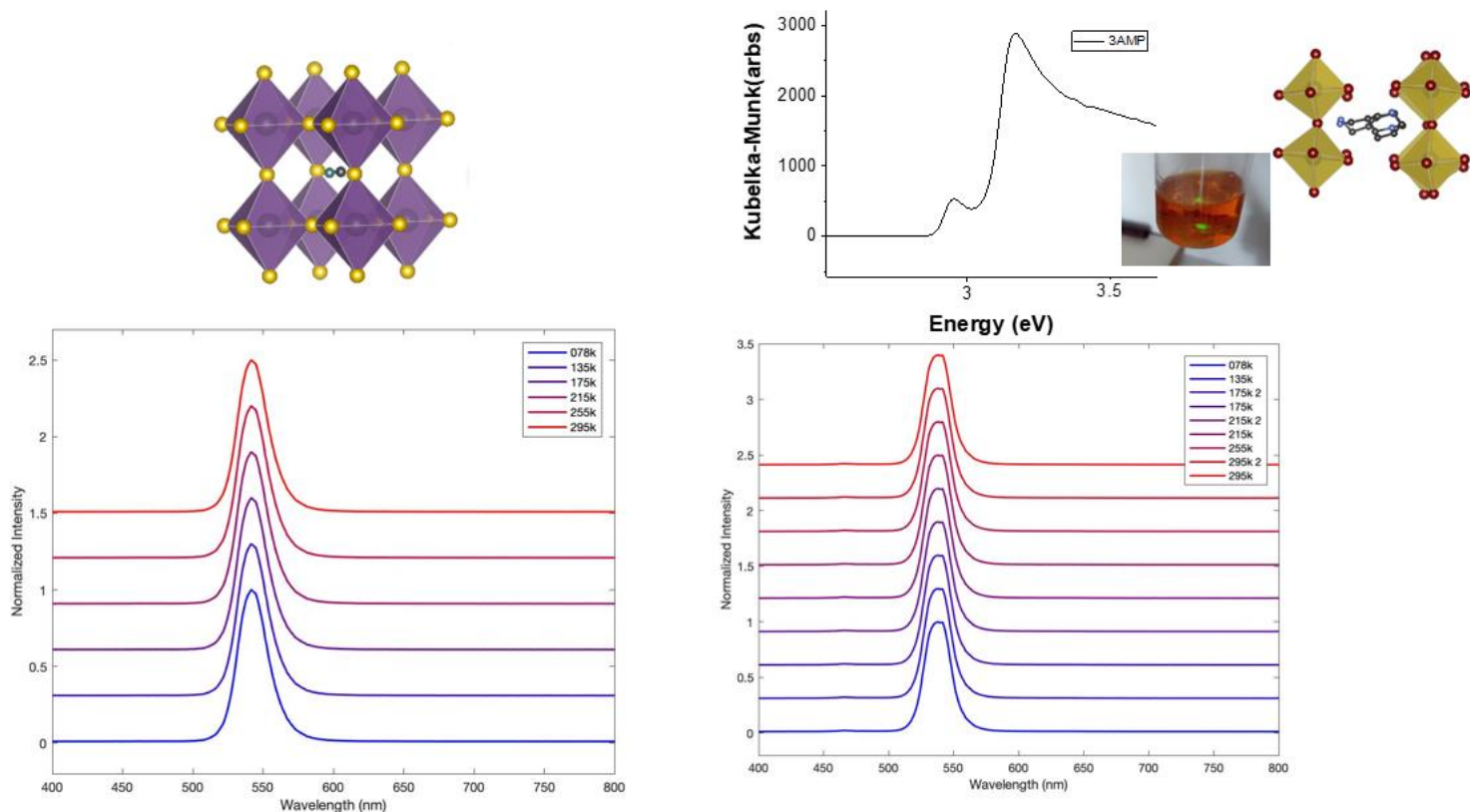


**Figure 30.** Optical absorption and photoluminescence spectra of (4amp)PbBr<sub>4</sub>

“white light” emission (Figure 30). The origins of all these effects are still unclear and need further investigation.

Figure 31 presents the structural parameters of the previously described perovskites. The (bpip)PbBr<sub>4</sub> perovskite has the higher distortion index among the three structures and this is probably the reason for the brighter white light emission (Figure 28).

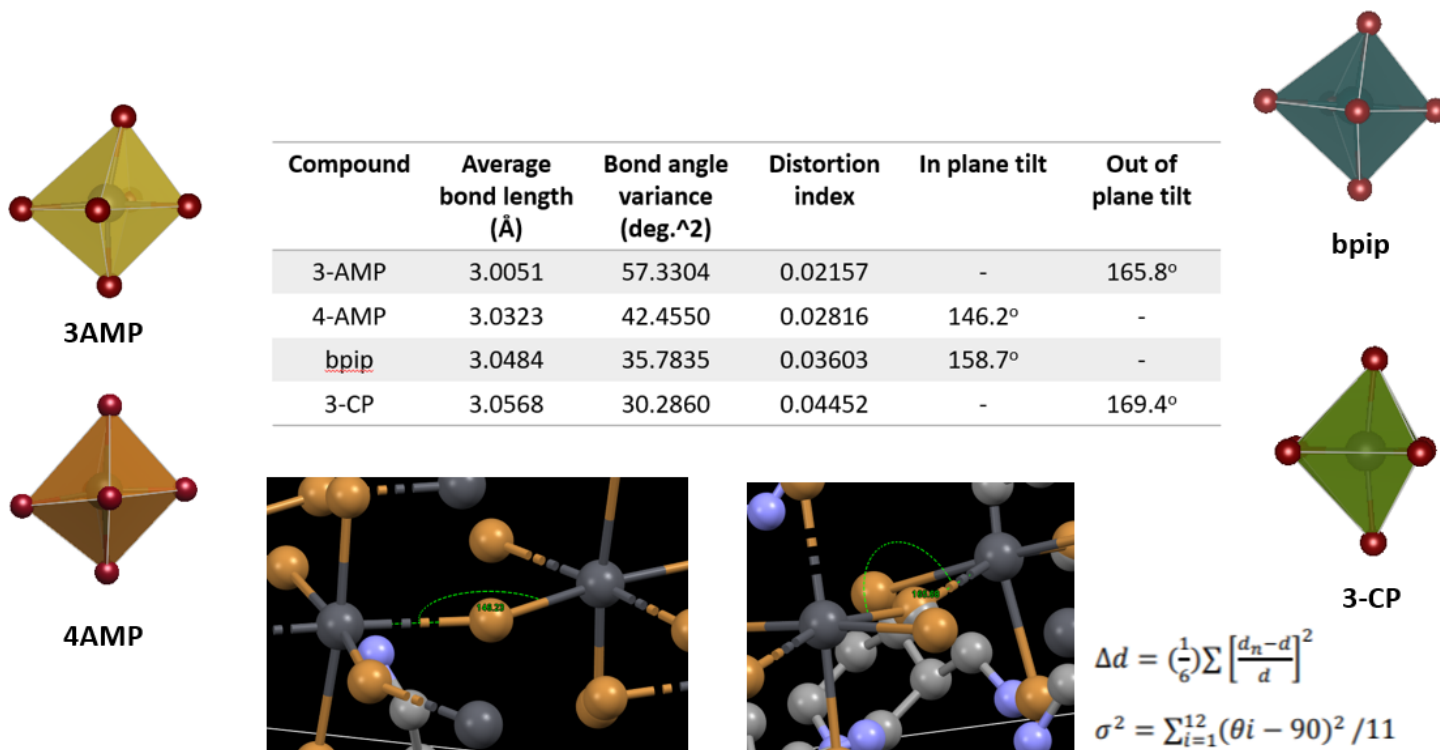


**Figure 31.** Structural parameters of the perovskites.

The last structure that was synthesized ((3cp)PbBr<sub>3</sub>) has a different crystal structure than the other three perovskites as described in section 4.1. The difference in the octahedral connectivity makes the bandgap indirect which results in no photoluminescence emission peak at room temperature. The sample needs to be cooled below 160K in order to observe a PL emission as shown in Figure 32 and being more clear at 77K.



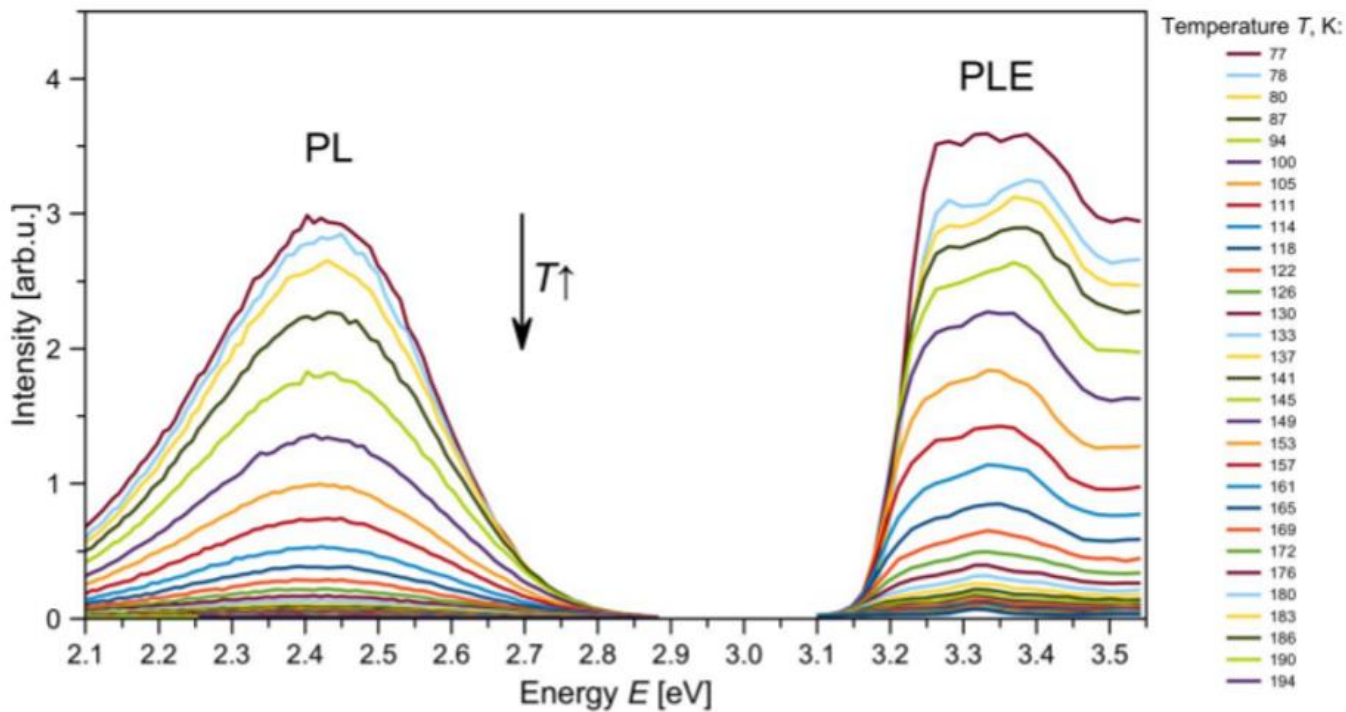
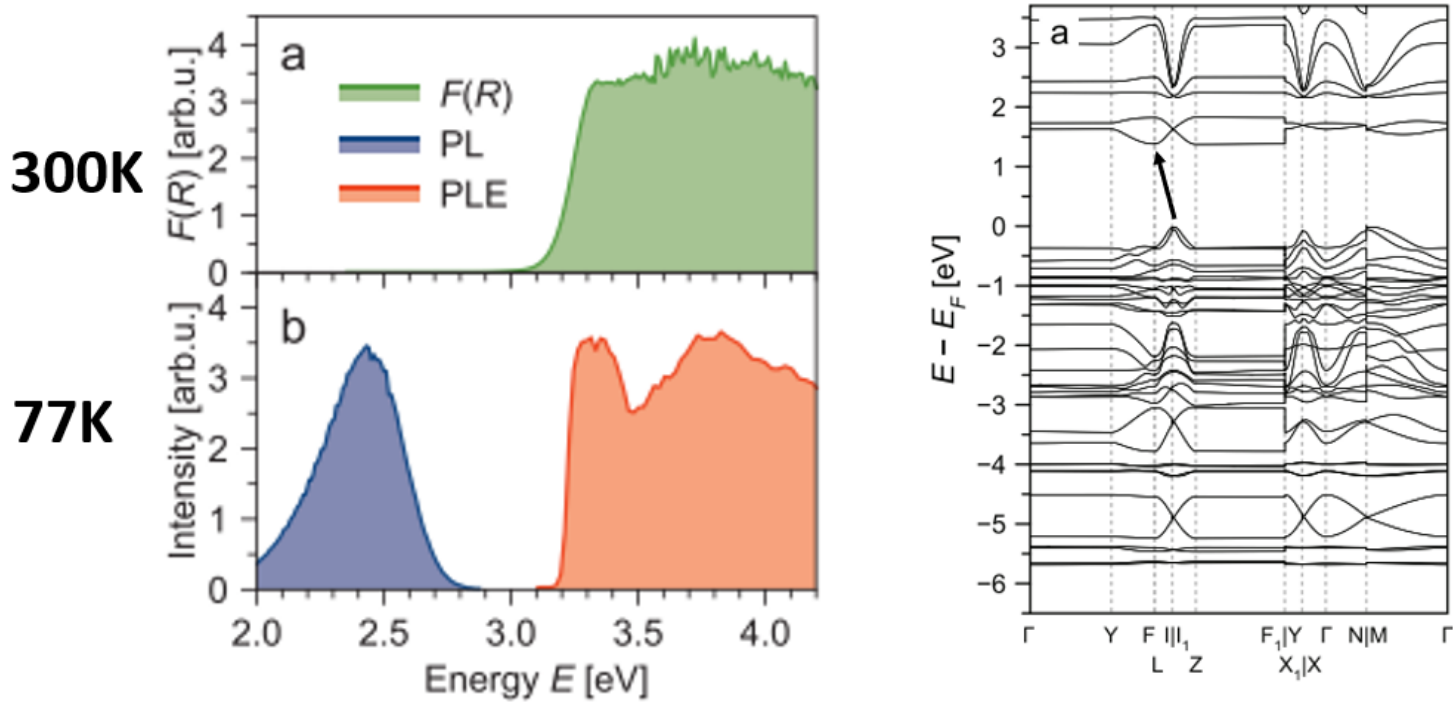


Figure 32. Optical absorption and photoluminescence spectra of  $(3cp)PbBr_3$

# Conclusions

In this Thesis, the two different natures of excitons were examined through the properties of 2D halide perovskites. In the  $(\text{CH}_3(\text{CH}_2)_3\text{NH}_3)_2(\text{CH}_3\text{NH}_3)_{n-1}\text{Pb}_n\text{I}_{3n+1}$  series the fast exciton recombination and localized emission were very important in order to create room-temperature polaritons for polariton lasing. The  $(\text{BA})_2(\text{MA})_2\text{Pb}_3\text{I}_{10}$  ( $n=3$ ) was optimized for cavity formation and we demonstrated possible polariton formation. On the other hand, the structural distortions in the 2D Dion-Jacobson type perovskites introduced by the asymmetric organic cations, lead to self-trapped excitons and broadband emission producing efficient, single-component white-light emitters during the process. We synthesized 3 new structures that emit white light and observed an unexpected green light emission from the 3AMP structure. By changing the organic spacer you can navigate through the optoelectronic diversity of the perovskites and achieve a plethora of applications with just one material. A better understanding of the effects of the structural distortion with the nature of the excitons will help in the selection of the suitable organic cation for better tunability of the perovskite properties. We also want to proceed with band structure calculations for all structures and test more cations for white light.

# References

- <sup>1</sup> Rose G (1839) Beschreibung einiger neuer Mineralien vom Ural. *Ann der Phys und Chemie* 48:551–572
- <sup>2</sup> Weber, D. CH<sub>3</sub>NH<sub>3</sub>PbX<sub>3</sub>, ein Pb (II)-System mit kubischer Perowskitstruktur/ CH<sub>3</sub>NH<sub>3</sub>PbX<sub>3</sub>, a Pb (II)-system with cubic perovskite structure. *Z. Naturforsch., B: J. Chem. Sci.* 1978, 33, 1443–1445
- <sup>3</sup> Wells, H. L. Über die Cäsium- und Kalium-Bleihalogenide. *Z. Anorg. Allg. Chem.* 1893, 3, 195–210
- <sup>4</sup> Møller, C. K. Crystal Structure and Photoconductivity of Caesium Plumbohalides. *Nature* 1958, 182, 1436–1436.
- <sup>5</sup> Møller, C. K. The structure of perovskite-like Caesium Plumbo trihalides. *Mat.-Fys. Medd. Dan. Vid. Selsk* 1959, 32, 2.
- <sup>6</sup> Auger, V.; Karantassis, T. Sels complexes de l'iodure stanneux avec les iodures de rubidium et de caesium. *Compt. Rend.* 1925, 181, 665–666.
- <sup>7</sup> Karantassis, T.; Capatos, L. Sur les complexes iodés du germanium divalent. *Compt. Rend.* 1935, 201, 74–75.
- <sup>8</sup> Kojima, A.; Teshima, K.; Shirai, Y.; Miyasaka, T. Organometal Halide Perovskites as Visible-Light Sensitizers for Photovoltaic Cells. *J. Am. Chem. Soc.* 2009, 131, 6050–6051.
- <sup>9</sup> Chung, I.; Lee, B.; He, J.; Chang, R. P. H.; Kanatzidis, M. G. Allsolid-state dye-sensitized solar cells with high efficiency. *Nature* 2012, 485, 486.
- <sup>10</sup> Lee, M. M.; Teuscher, J.; Miyasaka, T.; Murakami, T. N.; Snaith, H. J. Efficient Hybrid Solar Cells Based on Meso-Superstructured Organometal Halide Perovskites. *Science* 2012, 338, 643–647
- <sup>11</sup> Kim, H.-S.; Lee, C.-R.; Im, J.-H.; Lee, K.-B.; Moehl, T.; Marchioro, A.; Moon, S.-J.; Humphry-Baker, R.; Yum, J.-H.; Moser, J. E.; Gratzel, M.; Park, N.-G. Lead Iodide Perovskite Sensitized All-Solid-State Submicron Thin Film Mesoscopic Solar Cell with Efficiency Exceeding 9%. *Sci. Rep.* 2012, 2, 591.
- <sup>12</sup> Gao, P.; Gratzel, M.; Nazeeruddin, M. K. Organohalide lead perovskites for photovoltaic applications. *Energy Environ. Sci.* 2014, 7, 2448–2463.
- <sup>13</sup> Yang, W. S.; Park, B.-W.; Jung, E. H.; Jeon, N. J.; Kim, Y. C.; Lee, D. U.; Shin, S. S.; Seo, J.; Kim, E. K.; Noh, J. H.; Seok, S. I. Iodide management in formamidinium-lead-halide-based perovskite layers for efficient solar cells. *Science* 2017, 356, 1376–1379.
- <sup>14</sup> Goldschmidt, V. M. Die Gesetze der Krystallochemie. *Naturwissenschaften* 1926, 14, 477–485.
- <sup>15</sup> Androulakis, J., et al. (2011). "Dimensional Reduction: A Design Tool for New Radiation Detection Materials." *Adv. Mater.* **23**(36): 4163-4167.
- <sup>16</sup> Stoumpos, C. C., Mao, L., Malliakas, C. D. & Kanatzidis, M. G. Structure–Band Gap Relationships in Hexagonal Polytypes and Low-Dimensional Structures of Hybrid Tin Iodide Perovskites. *Inorg. Chem.* **56**, 56–73 (2017).
- <sup>17</sup> Stoumpos, C. C. & Kanatzidis, M. G. The Renaissance of Halide Perovskites and Their Evolution as Emerging Semiconductors. *Acc. Chem. Res.* **48**, 2791–2802 (2015).
- <sup>18</sup> Arlt, G.; Hennings, D.; de With, G. Dielectric properties of finegrained barium titanate ceramics. *J. Appl. Phys.* 1985, 58, 1619–1625
- <sup>19</sup> Ishihara, T.; Takahashi, J.; Goto, T. Exciton state in twodimensional perovskite semiconductor (C<sub>10</sub>H<sub>21</sub>NH<sub>3</sub>)<sub>2</sub>PbI<sub>4</sub>. *Solid State Commun.* 1989, 69, 933–936
- <sup>20</sup> Nakajima, T.; Yamauchi, H.; Goto, T.; Yoshizawa, M.; Suzuki, T.; Fujimura, T. Magnetic and elastic properties of (CH<sub>3</sub>NH<sub>3</sub>)<sub>2</sub>FeCl<sub>4</sub> and (C<sub>2</sub>H<sub>5</sub>NH<sub>3</sub>)<sub>2</sub>FeCl<sub>4</sub>. *J. Magn. Mater.* 1983, 31-34, 1189– 1190.
- <sup>21</sup> Dolzhenko, Y. I.; Inabe, T.; Maruyama, Y. In Situ X-Ray Observation on the Intercalation of Weak Interaction Molecules into Perovskite-Type Layered Crystals (C<sub>9</sub>H<sub>19</sub>NH<sub>3</sub>)<sub>2</sub>PbI<sub>4</sub> and (C<sub>10</sub>H<sub>21</sub>NH<sub>3</sub>)<sub>2</sub>CdCl<sub>4</sub>. *Bull. Chem. Soc. Jpn.* 1986, 59, 563–567.

- 22 Papavassiliou, G. C.; Patsis, A. P.; Lagouvardos, D. J.; Koutselas, I. B. Spectroscopic studies of  $(C_{10}H_{21}NH_3)_2PbI_4$ ,  $(CH_3NH_3)(C_{10}H_{21}NH_3)_2Pb_2I_7$ ,  $(CH_3NH_3)PbI_3$ , and similar compounds. *Synth. Met.* 1993, 57, 3889–3894.
- 23 Calabrese, J.; Jones, N. L.; Harlow, R. L.; Herron, N.; Thorn, D. L.; Wang, Y. Preparation and characterization of layered lead halide compounds. *J. Am. Chem. Soc.* 1991, 113, 2328–2330.
- 24 Mitzi, D. B.; Feild, C. A.; Harrison, W. T. A.; Guloy, A. M. Conducting tin halides with a layered organic-based perovskite structure. *Nature* 1994, 369, 467–469
- 25 O. Nazarenko, M.R. Kotyrba, S. Yakunin, M. Aebli, G. Raino et al., Guanidinium-formamidinium lead iodide: a layered perovskite-related compound with red luminescence at room temperature. *J. Am. Chem. Soc.* **140**(11), 3850–3853 (2018).
- 26 L. Cheng, T. Jiang, Y. Cao, C. Yi, N. Wang et al., Multiple-quantum-well perovskites for high-performance light-emitting diodes. *Adv. Mater.* **32**(15), e1904163 (2020).
- 27 L. Mao, W. Ke, L. Pedesseau, Y. Wu, C. Katan et al., Hybrid Dion-Jacobson 2D lead iodide perovskites. *J. Am. Chem. Soc.* **140**(10), 3775–3783 (2018).
- 28 Ruddlesden, S. N.; Popper, P. New compounds of the  $K_2NiF_4$  type. *Acta Crystallogr.* 1957, 10, 538–539
- 29 Ruddlesden, S. N.; Popper, P. The compound  $Sr_3Ti_2O_7$  and its structure. *Acta Crystallogr.* 1958, 11, 54–55.
- 30 Dion, M.; Ganne, M.; Tournoux, M. Nouvelles familles de phases  $M(I)M(II)_2Nb_3O_{10}$  a feuillets "perovskites. *Mater. Res. Bull.* 1981, 16, 1429–1435.
- 31 Jacobson, A. J.; Johnson, J. W.; Lewandowski, J. T. Interlayer chemistry between thick transition-metal oxide layers: synthesis and intercalation reactions of  $K[Ca_2Na_{n-3}Nb_nO=]$  ( $3 \leq n \leq 7$ ). *Inorg. Chem.* 1985, 24, 3727–3729.
- 32 Aurivillius, B. Mixed bismuth oxides with layer lattices. The structure type of  $CaNb_2Bi_2O_9$ . *Ark. Kemi* 1949, 1, 463–480
- 33 Aurivillius, B. Mixed bismuth oxides with layer lattices. Structure of  $BaBi_4Ti_4O_{15}$ . *Ark. Kemi* 1950, 2, 519–527.
- 34 Schaak, R. E. & Mallouk, T. E. Perovskites by Design: A Toolbox of Solid-State Reactions. *Chem. Mater.* **14**, 1455–1471 (2002).
- 35 Toyozawa Y. 2003. Excitons. In *Optical Processes in Solids*, pp. 113–48. Cambridge, UK: Cambridge Univ. Press
- 36 Frenkel, J. On the Transformation of Light into Heat in Solids. I. *Phys. Rev.* 1931, 37, 17–44
- 37 Toyozawa, Y. In *Optical Processes in Solids*; Cambridge University Press: Cambridge, U.K., 2003; pp 113–148.
- 38 Song, K. S.; Williams, R. T. *Self-Trapped Excitons*, 2nd ed.; Springer: Berlin, Germany, 1996; Vol. 105
- 39 Miyata, K., et al. (2017). "Large polarons in lead halide perovskites." *Science Advances* **3**(8): e1701217.
- 40 Adachi S. 2005. Optical properties. In *Physical Properties of III-V Semiconductor Compounds*, pp. 135–92. New York: Wiley-VCH
- 41 Yaffe, O. et al. Excitons in ultrathin organic-inorganic perovskite crystals. *Phys. Rev. B* **92**, 045414 (2015).
- 42 Blancon, J.C., Even, J., Stoumpos, C.C. et al. Semiconductor physics of organic–inorganic 2D halide perovskites. *Nat. Nanotechnol.* **15**, 969–985 (2020). <https://doi.org/10.1038/s41565-020-00811-1>
- 43 Ishihara T. 1994. Optical properties of  $PbI_4$ -based perovskite structures. *J. Lumin.* 60–61:269–74
- 44 Hong X, Ishihara T, Nurmikko AV. 1992. Dielectric confinement effect on excitons in  $PbI_4$ -based layered semiconductors. *Phys. Rev. B Condens. Matter Mater. Phys.* 45:6961–64
- 45 Shinada M, Sugano S. 1966. Interband optical transitions in extremely anisotropic semiconductors. I. Bound and unbound exciton absorption. *J. Phys. Soc. Jpn.* 21:1936–46
- 46 Hanamura E, Nagaosa N, Kumagai M, Takagahara T. 1988. Quantum wells with enhanced exciton effects and optical non-linearity. *Mater. Sci. Eng. B* 1:255–58
- 47 Mitzi DB. 1999. Synthesis, structure, and properties of organic–inorganic perovskites and related materials. In *Progress in Inorganic Chemistry*, Vol. 48, ed. KD Karlin, pp. 1–121. New York: John Wiley & Sons
- 48 Pyykko, P. Relativistic effects in structural chemistry. *Chem. Rev.* **88**, 563–594 (1988).

- 49 Stoumpos CC, Cao DH, Clark DJ, Young J, Rondinelli JM, et al. 2016. Ruddlesden–Popper hybrid lead iodide perovskite 2D homologous semiconductors. *Chem. Mater.* 28:2852–67
- 50 Stoumpos CC, Soe CMM, Tsai H, Nie W, Blancon J-C, et al. 2017. High members of the 2D Ruddlesden–Popper halide perovskites: synthesis, optical properties, and solar cells of  $(\text{CH}_3(\text{CH}_2)_3\text{NH}_3)_2(\text{CH}_3\text{NH}_3)_4\text{Pb}_5\text{I}_{16}$ . *Chem* 2:427–40
- 51 Mitzi, D. B. Synthesis, Crystal Structure, and Optical and Thermal Properties of  $(\text{C}_4\text{H}_9\text{NH}_3)_2\text{MII}_4$  (M = Ge, Sn, Pb). *Chem. Mater.* 1996, 8, 791–800.
- 52 Dohner, E. R.; Hoke, E. T.; Karunadasa, H. I. Self-Assembly of Broadband White-Light Emitters. *J. Am. Chem. Soc.* 2014, 136, 1718–1721.
- 53 Stoumpos, C. C. *et al.* High Members of the 2D Ruddlesden–Popper Halide Perovskites: Synthesis, Optical Properties, and Solar Cells of  $(\text{CH}_3(\text{CH}_2)_3\text{NH}_3)_2(\text{CH}_3\text{NH}_3)_4\text{Pb}_5\text{I}_{16}$ . *Chem* 2, 427–440 (2017).
- 54 Kawano N, Koshimizu M, Sun Y, Yahaba N, Fujimoto Y, et al. 2014. Effects of organic moieties on luminescence properties of organic–inorganic layered perovskite-type compounds. *J. Phys. Chem. C* 118:9101–6
- 55 Smith, M.; Karunadasa, H. White-Light Emission from Layered Halide Perovskites. *Acc. Chem. Res.* 2018, 51, 619
- 56 Smith, M. D.; Jaffe, A.; Dohner, E. R.; Lindenberg, A. M.; Karunadasa, H. I. Structural Origins of Broadband Emission from Layered Pb–Br Hybrid Perovskites. *Chem. Sci.* 2017, 8, 4497–4504.
- 57 Tanaka, K.; Takahashi, T.; Kondo, T.; Umeda, K.; Ema, K.; Umebayashi, T.; Asai, K.; Uchida, K.; Miura, N. Electronic and Excitonic Structures of Inorganic–Organic Perovskite-Type Quantum-Well Crystal  $(\text{C}_4\text{H}_9\text{NH}_3)_2\text{PbBr}_4$ . *Jpn. J. Appl. Phys., Part 1* 2005, 44 (44), 5923–5932
- 58 Dohner, E. R.; Hoke, E. T.; Karunadasa, H. I. Self-Assembly of Broadband White-Light Emitters. *J. Am. Chem. Soc.* 2014, 136, 1718–1721.
- 59 Dohner, E. R.; Jaffe, A.; Bradshaw, L. R.; Karunadasa, H. I. Intrinsic White-Light Emission from Layered Hybrid Perovskites. *J. Am. Chem. Soc.* 2014, 136, 13154–13157.
- 60 Guo, X.; Houser, K. W. A Review of Colour Rendering Indices and Their Application to Commercial Light Sources. *Lighting Res. Technol.* 2004, 36, 183.
- 61 Narendran, N.; Deng, L. *Solid State Lighting II*; International Society for Optics and Photonics, 2002; Vol. 4776, p 61
- 62 Hu, T.; Smith, M. D.; Dohner, E. R.; Sher, M.-J.; Wu, X.; Trinh, M. T.; Fisher, A.; Corbett, J.; Zhu, X.-Y.; Karunadasa, H. I.; Lindenberg, A. M. Mechanism for Broadband White-Light Emission from Two-Dimensional (110) Hybrid Perovskites. *J. Phys. Chem. Lett.* 2016, 7, 2258.
- 63 Thomaz, J. E., Lindquist, K. P., Karunadasa, H. I. & Fayer, M. D. Single Ensemble Non-exponential Photoluminescent Population Decays from a Broadband White-Light-Emitting Perovskite. *J. Am. Chem. Soc.* 142, 16622–16631 (2020).
- 64 Smith, I. C.; Hoke, E. T.; Solis-Ibarra, D.; McGehee, M. D.; Karunadasa, H. I. A Layered Hybrid Perovskite Solar-Cell Absorber with Enhanced Moisture Stability. *Angew. Chem., Int. Ed.* 2014, 53, 11232–11235
- 65 Lin, Y.; Bai, Y.; Fang, Y.; Wang, Q.; Deng, Y.; Huang, J. Suppressed Ion Migration in Low-Dimensional Perovskites. *ACS Energy Lett.* 2017, 2, 1571–1572
- 66 Cao, D. H.; Stoumpos, C. C.; Farha, O. K.; Hupp, J. T.; Kanatzidis, M. G. 2D Homologous Perovskites as Light-Absorbing Materials for Solar Cell Applications. *J. Am. Chem. Soc.* 2015, 137, 7843–7850
- 67 Lee MM, Teuscher J, Miyasaka T, Murakami TN, Snaith HJ. 2012. Efficient hybrid solar cells based on meso-superstructured organometal halide perovskites. *Science* 338:643–47
- 68 . Tsai H, Nie W, Blancon J-C, Stoumpos CC, Asadpour R, et al. 2016. High-efficiency two-dimensional Ruddlesden–Popper perovskite solar cells. *Nature* 536:312–16
- 69 Hong, X.; Ishihara, T.; Nurmikko, A. V. Photoconductivity and Electroluminescence in Lead Iodide Based Natural Quantum Well Structures. *Solid State Commun.* 1992, 84, 657–661.
- 70 Era, M.; Morimoto, S.; Tsutsui, T.; Saito, S. Organic–Inorganic Heterostructure Electroluminescent Device Using a Layered Perovskite Semiconductor  $(\text{C}_6\text{H}_5\text{C}_2\text{H}_4\text{NH}_3)_2\text{PbI}_4$ . *Appl. Phys. Lett.* 1994, 65, 676–678

- 
- <sup>71</sup> Chondroudis K, Mitzi DB. 1999. Electroluminescence from an organic-inorganic perovskite incorporating a quaterthiophene dye within lead halide perovskite layers. *Chem. Mater.* **11**:3028–30
- <sup>72</sup> Ponce, F. A.; Bour, D. P. Nitride-based semiconductors for blue and green light-emitting devices. *Nature* 1997, **386**, 351–359.
- <sup>73</sup> Sierra, J., Kasimov, A., Markowich, P. & Weishäupl, R.-M. On the Gross–Pitaevskii Equation with Pumping and Decay: Stationary States and Their Stability. *Journal of Nonlinear Science* **25**, (2013).
- <sup>74</sup> Deng, H.; Weihs, G.; Snoke, D.; Bloch, J.; Yamamoto, Y. Polariton lasing vs. photon lasing in a semiconductor microcavity. *Proc. Natl. Acad. Sci. U. S. A.* 2003, **100**, 15318–15323
- <sup>75</sup> Pan, D. et al. Deterministic fabrication of arbitrary vertical heterostructures of two-dimensional Ruddlesden–Popper halide perovskites. *Nat. Nanotechnol.* **16**, 159–165 (2021).
- <sup>76</sup> Mao, L. et al. Structural Diversity in White-Light-Emitting Hybrid Lead Bromide Perovskites. *J. Am. Chem. Soc.* **140**, 13078–13088 (2018).
- <sup>77</sup> Mao, L. et al. Organic Cation Alloying on Intralayer A and Interlayer A' sites in 2D Hybrid Dion–Jacobson Lead Bromide Perovskites (A')(A)Pb<sub>2</sub>Br<sub>7</sub>. *J. Am. Chem. Soc.* **142**, 8342–8351 (2020).
- <sup>78</sup> Blancon, J.-C. et al. Extremely efficient internal exciton dissociation through edge states in layered 2D perovskites. *Science* **355**, 1288–1292 (2017).
- <sup>79</sup> Mao, L.; Ke, W.; Pedesseau, L.; Wu, Y.; Katan, C.; Even, J.; Wasielewski, M. R.; Stoumpos, C. C.; Kanatzidis, M. G. Hybrid DionJacobson 2D Lead Iodide Perovskites. *J. Am. Chem. Soc.* 2018, **140**, 3775–3783.
- <sup>80</sup> A. R. Oganov, S. Ono, *Nature* 2004, **430**, 445.
- <sup>8181</sup> Selivanov, N. I. et al. Hybrid Organic–Inorganic Halide Post-Perovskite 3-Cyanopyridinium Lead Tribromide for Optoelectronic Applications. *Adv. Funct. Mater.* **31**, 2102338 (2021).
- <sup>82</sup> H. Takagi et al, " Influence of the image charge effect on excitonic energy structure in organic-inorganic multiple quantum well crystals" *Phys. Rev. B: Condens. Matter Mater. Phys.*, **2013**, *87*, 125421.

---

# Appendix

Table 1. Crystal data and structure refinement for C<sub>6</sub> N<sub>2</sub> H<sub>12</sub> Pb Br<sub>4</sub> at 293 K.

Empirical formula	C <sub>6</sub> N <sub>2</sub> H <sub>12</sub> Pb Br <sub>4</sub>
Formula weight	639
Temperature	293 K
Wavelength	0.71073 Å
Crystal system	monoclinic
Space group	C 1 c 1
Unit cell dimensions	a = 11.88600(10) Å, α = 90° b = 20.0637(2) Å, β = 96.2893(8)° c = 11.94260(10) Å, γ = 90°
Volume	2830.90(4) Å <sup>3</sup>
Z	8
Density (calculated)	2.9985 g/cm <sup>3</sup>
Absorption coefficient	23.177 mm <sup>-1</sup>
F(000)	2328
Crystal size	? x ? x ? mm <sup>3</sup>
θ range for data collection	2 to 35.56°
Index ranges	-19 ≤ h ≤ 18, -31 ≤ k ≤ 32, -17 ≤ l ≤ 19
Reflections collected	72250
Independent reflections	11277 [R <sub>int</sub> = 0.038]
Completeness to θ = 34.24°	98%
Refinement method	Full-matrix least-squares on F <sup>2</sup>
Data / restraints / parameters	11277 / 0 / 246
Goodness-of-fit	9.44
Final R indices [I > 2σ(I)]	R <sub>obs</sub> = 0.2540, wR <sub>obs</sub> = 0.4398
R indices [all data]	R <sub>all</sub> = 0.2626, wR <sub>all</sub> = 0.4575
Extinction coefficient	130000(5000)
Largest diff. peak and hole	131.44 and -14.04 e·Å <sup>-3</sup>

$$R = \frac{\sum ||F_o| - |F_c||}{\sum |F_o|}, wR = \left\{ \frac{\sum [w(|F_o|^2 - |F_c|^2)^2]}{\sum [w(|F_o|^4)]} \right\}^{1/2} \text{ and } w = 1/(\sigma^2(I) + 0.0004I^2)$$



Table 2. Atomic coordinates ( $\times 10^4$ ) and equivalent isotropic displacement parameters ( $\text{\AA}^2 \times 10^3$ ) for C6 N2 H12 Pb Br4 at 293 K with estimated standard deviations in parentheses.

Label	x	y	z	Occupancy	$U_{\text{eq}}^*$
Pb(1)	6666(3)	50(2)	1988(3)	1	34(2)
Pb(2)	1692(2)	57(2)	1709(2)	1	34(2)
Br(1)	6387(10)	-93(5)	-462(11)	1	51(4)
Br(2)	6992(9)	3553(5)	1419(11)	1	58(3)
Br(3)	6196(10)	-1446(4)	2193(10)	1	57(3)
Br(4)	6701(10)	1513(4)	1669(12)	1	57(4)
Br(5)	4184(11)	211(3)	1831(15)	1	58(2)
Br(6)	9189(14)	-101(3)	-3132(17)	1	51(2)
Br(7)	1523(10)	1533(4)	1878(11)	1	52(3)
Br(8)	2000(18)	-42(8)	4130(16)	1	78(7)
C(13)	4060(70)	2360(50)	-270(70)	1	70(30)
C(1)	9580(60)	2650(30)	-680(60)	1	50(20)
N(1)	8950(50)	1610(20)	280(50)	1	48(18)
C(4)	3510(60)	3490(40)	300(80)	1	60(30)
C(5)	8670(80)	2330(40)	0(70)	1	50(30)
N(2)	10010(60)	1600(20)	4100(60)	1	80(30)
C(6)	4980(70)	3490(40)	3550(80)	1	70(30)
C(9)	9300(60)	3360(30)	-1010(60)	1	50(20)
C(10)	3660(70)	1670(30)	-570(70)	1	60(30)
C(12)	2110(60)	-90(30)	4120(80)	1	15(16)
C(2)	4170(70)	3800(40)	4260(70)	1	60(30)
N(3)	4190(60)	1160(30)	4920(50)	1	70(30)
C(3)	4760(60)	2770(40)	3330(70)	1	60(30)
C(7)	4680(60)	2670(40)	-1200(80)	1	50(30)
C(11)	3170(70)	2800(40)	30(60)	1	70(30)
C(14)	9160(70)	1180(40)	4470(90)	1	70(40)
N(4)	4510(50)	1180(30)	-710(50)	1	100(30)
H(1c13)	4583.79	2314.06	396.19	1	79.7
H(1c1)	10276.73	2659.51	-187.11	1	56.8
H(1c4)	3929.98	3509.6	1030.35	1	74.1
H(2c4)	2849.19	3754.57	393	1	74.1
H(1c5)	8633.96	2580.31	684.43	1	65.2

H(2c5)	7944.43	2358.09	-434.88	1	65.2
H(1c6)	5734.39	3550.07	3903.82	1	78.4
H(2c6)	4943.92	3724.79	2847.47	1	78.4
H(1c9)	9858.27	3525.68	-1469.84	1	64
H(2c9)	8630.56	3372.15	-1532.55	1	64
H(1c10)	3180.3	1518.33	-31.55	1	74.7
H(2c10)	3131.16	1686.65	-1236.01	1	74.7
H(1c2)	3470.98	3883.18	3806.97	1	68.8
H(2c2)	4440.19	4230.76	4493.34	1	68.8
H(1c3)	4122.85	2714.92	2768.6	1	71.5
H(2c3)	5359.82	2580.25	2959.66	1	71.5
H(1c7)	4194.03	2664.04	-1896.31	1	63.9
H(2c7)	5345.81	2416.8	-1287.77	1	63.9
H(1c11)	2554.31	2800.78	-560.97	1	83.3
H(2c11)	2826.68	2614.8	648.14	1	83.3
H(1c14)	9507.05	781.59	4799.7	1	85.8
H(2c14)	8657.32	1036.83	3836.46	1	85.8
H(1n1)	8402.54	1432.32	600.03	1	58
H(2n1)	9543.47	1594.1	782.32	1	58
H(1n2)	10294.78	1417.15	3535.71	1	96.7
H(2n2)	10606.68	1600.13	4600.15	1	96.7
H(1n3)	3919.5	789.27	4638.91	1	86.4
H(2n3)	4849.46	1096.79	5289.75	1	86.4
H(3n3)	3731.27	1329.42	5364.72	1	86.4
H(1n4)	4190.8	790.12	-812.59	1	120.4
H(2n4)	4860.54	1279.02	-1288.71	1	120.4
H(3n4)	4995.04	1166.78	-107.04	1	120.4

\* $U_{eq}$  is defined as one third of the trace of the orthogonalized  $U_{ij}$  tensor.

Table 3. Anisotropic displacement parameters ( $\text{\AA}^2 \times 10^3$ ) for C6 N2 H12 Pb Br4 at 293 K with estimated standard deviations in parentheses.

Label	$U_{11}$	$U_{22}$	$U_{33}$	$U_{12}$	$U_{13}$	$U_{23}$
Pb(1)	30(2)	40(2)	33(2)	0(2)	6(2)	2(2)
Pb(2)	29(2)	40(2)	33(2)	2(2)	7(2)	0(2)
Br(1)	61(7)	65(5)	27(5)	2(5)	7(5)	-1(4)
Br(2)	70(6)	45(5)	62(6)	5(4)	21(4)	-1(4)

Br(3)	72(6)	40(5)	61(6)	-2(4)	24(4)	4(4)
Br(4)	55(5)	36(4)	86(8)	4(4)	31(5)	8(4)
Br(5)	26(2)	73(3)	76(4)	3(8)	6(2)	-9(9)
Br(6)	27(2)	57(3)	71(4)	-2(5)	11(2)	-6(7)
Br(7)	60(6)	39(4)	60(5)	-2(4)	18(4)	3(4)
Br(8)	110(14)	94(11)	29(9)	-3(7)	5(9)	1(6)
C(13)	50(50)	90(60)	60(60)	20(40)	10(40)	30(50)
C(1)	50(40)	40(30)	60(40)	0(30)	10(30)	10(30)
N(1)	60(40)	30(20)	50(30)	10(20)	30(30)	0(20)
C(4)	70(50)	40(50)	80(60)	20(40)	50(50)	10(40)
C(5)	70(60)	50(50)	50(40)	10(40)	30(40)	20(40)
N(2)	120(60)	50(30)	90(60)	20(40)	70(50)	20(30)
C(6)	70(60)	60(60)	70(60)	10(40)	20(50)	10(40)
C(9)	70(50)	50(40)	40(30)	-10(30)	40(40)	0(30)
C(10)	80(50)	40(40)	80(60)	10(40)	40(50)	-10(30)
C(12)	20(20)	10(20)	30(40)	-4(16)	10(20)	-10(20)
C(2)	80(60)	40(40)	60(50)	20(50)	40(40)	20(40)
N(3)	80(50)	30(30)	110(60)	10(30)	40(40)	0(30)
C(3)	80(60)	60(40)	40(40)	20(40)	20(40)	10(30)
C(7)	50(50)	50(40)	70(50)	-10(40)	30(40)	-20(40)
C(11)	50(50)	70(50)	90(70)	10(40)	40(40)	10(50)
C(14)	100(70)	30(40)	90(70)	-10(50)	30(60)	-20(50)
N(4)	150(70)	70(40)	120(60)	40(40)	140(60)	30(40)

The anisotropic displacement factor exponent takes the form:  $-2\pi^2[h^2a^{*2}U_{11} + \dots + 2hka^*b^*U_{12}]$ .

Table 4. Bond lengths [ $\text{\AA}$ ] for C6 N2 H12 Pb Br4 at 293 K with estimated standard deviations in parentheses.

Label	Distances
Pb(1)-Br(1)	2.922(13)
Pb(1)-Br(1)#0	3.101(14)
Pb(1)-Br(3)	3.068(10)
Pb(1)-Br(4)	2.960(9)
Pb(1)-Br(5)	2.954(14)
Pb(1)-Br(6)#0	3.019(17)
Pb(2)-Br(2)#0	3.064(10)
Pb(2)-Br(5)	2.965(14)

---

Pb(2)-Br(6)#0	3.004(17)
Pb(2)-Br(7)	2.976(9)
Pb(2)-Br(8)	2.881(19)
Br(1)-N(3)#0	3.45(7)
Br(1)-N(4)	3.38(6)
Br(2)-N(2)#0	3.44(7)
Br(2)-N(3)#0	3.38(7)
Br(3)-N(3)#0	3.46(6)
Br(3)-N(4)#0	3.42(6)
Br(4)-N(1)	3.30(6)
Br(5)-N(3)#0	3.59(6)
Br(6)-N(1)#0	3.57(5)
Br(7)-N(1)#0	3.42(5)
Br(7)-N(2)#0	3.37(7)
Br(8)-C(12)	0.16(7)
C(13)-C(10)	1.49(11)
C(13)-C(7)	1.53(12)
C(13)-C(11)	1.45(12)
C(13)-H(1c13)	0.96
C(1)-C(5)	1.55(12)
C(1)-C(9)	1.51(9)
C(1)-C(3)#0	1.48(11)
C(1)-H(1c1)	0.96
N(1)-C(5)	1.52(10)
N(1)-C(2)#0	1.52(10)
N(1)-H(1n1)	0.8701
N(1)-H(2n1)	0.87
C(4)-C(11)	1.47(11)
C(4)-C(14)#0	1.47(13)
C(4)-H(1c4)	0.9601
C(4)-H(2c4)	0.9601
C(5)-H(1c5)	0.9601
C(5)-H(2c5)	0.96
N(2)-C(7)#0	1.54(9)
N(2)-C(14)	1.43(11)
N(2)-H(1n2)	0.8699

---

N(2)-H(2n2)	0.87
C(6)-C(2)	1.47(12)
C(6)-C(3)	1.50(11)
C(6)-H(1c6)	0.96
C(6)-H(2c6)	0.9599
C(9)-N(3)#0	1.48(10)
C(9)-H(1c9)	0.9598
C(9)-H(2c9)	0.96
C(10)-N(4)	1.44(10)
C(10)-H(1c10)	0.9601
C(10)-H(2c10)	0.96
C(2)-H(1c2)	0.96
C(2)-H(2c2)	0.96
N(3)-H(1n3)	0.87
N(3)-H(2n3)	0.87
N(3)-H(3n3)	0.8702
C(3)-H(1c3)	0.96
C(3)-H(2c3)	0.9599
C(7)-H(1c7)	0.9599
C(7)-H(2c7)	0.9599
C(11)-H(1c11)	0.96
C(11)-H(2c11)	0.9601
C(14)-H(1c14)	0.96
C(14)-H(2c14)	0.96
N(4)-H(1n4)	0.87
N(4)-H(2n4)	0.8698
N(4)-H(3n4)	0.87

---

Table 5. Bond angles [°] for C6 N2 H12 Pb Br4 at 293 K with estimated standard deviations in parentheses.

---

Label	Angles
Br(1)-Pb(1)-Br(1)#0	166.8(3)
Br(1)-Pb(1)-Br(3)	89.0(3)
Br(1)-Pb(1)-Br(4)	88.3(3)
Br(1)-Pb(1)-Br(5)	86.8(4)
Br(1)-Pb(1)-Br(6)#0	87.7(5)

---

Br(1)#0-Pb(1)-Br(3)	84.8(3)
Br(1)#0-Pb(1)-Br(4)	95.9(3)
Br(1)#0-Pb(1)-Br(5)	81.1(4)
Br(1)#0-Pb(1)-Br(6)#0	105.0(5)
Br(3)-Pb(1)-Br(4)	170.2(3)
Br(3)-Pb(1)-Br(5)	85.6(3)
Br(3)-Pb(1)-Br(6)#0	103.1(3)
Br(4)-Pb(1)-Br(5)	84.9(3)
Br(4)-Pb(1)-Br(6)#0	86.1(3)
Br(5)-Pb(1)-Br(6)#0	169.6(4)
Br(2)#0-Pb(2)-Br(5)	88.9(3)
Br(2)#0-Pb(2)-Br(6)#0	99.5(2)
Br(2)#0-Pb(2)-Br(7)	175.9(4)
Br(2)#0-Pb(2)-Br(8)	92.4(4)
Br(5)-Pb(2)-Br(6)#0	170.0(4)
Br(5)-Pb(2)-Br(7)	88.1(3)
Br(5)-Pb(2)-Br(8)	86.7(5)
Br(6)#0-Pb(2)-Br(7)	83.8(3)
Br(6)#0-Pb(2)-Br(8)	87.5(6)
Br(7)-Pb(2)-Br(8)	90.2(4)
Pb(1)-Br(1)-Pb(1)#0	165.5(4)
Pb(1)-Br(1)-N(3)#0	86.3(11)
Pb(1)-Br(1)-N(4)	90.8(11)
Pb(1)#0-Br(1)-N(3)#0	108.0(11)
Pb(1)#0-Br(1)-N(4)	91.9(11)
N(3)#0-Br(1)-N(4)	88.8(15)
Pb(2)#0-Br(2)-N(2)#0	95.9(9)
Pb(2)#0-Br(2)-N(3)#0	90.1(11)
N(2)#0-Br(2)-N(3)#0	95.0(16)
Pb(1)-Br(3)-N(3)#0	83.9(11)
Pb(1)-Br(3)-N(4)#0	91.8(10)
N(3)#0-Br(3)-N(4)#0	98.2(15)
Pb(1)-Br(4)-N(1)	98.5(8)
Pb(1)-Br(5)-Pb(2)	167.7(3)
Pb(1)-Br(5)-N(3)#0	83.4(12)
Pb(2)-Br(5)-N(3)#0	87.7(12)

---

Pb(1)#0-Br(6)-Pb(2)#0	176.3(3)
Pb(1)#0-Br(6)-N(1)#0	91.9(9)
Pb(2)#0-Br(6)-N(1)#0	90.7(10)
Pb(2)-Br(7)-N(1)#0	94.1(8)
Pb(2)-Br(7)-N(2)#0	98.1(9)
N(1)#0-Br(7)-N(2)#0	85.3(15)
Pb(2)-Br(8)-C(12)	90(30)
C(10)-C(13)-C(7)	112(7)
C(10)-C(13)-C(11)	114(7)
C(10)-C(13)-H(1c13)	105.32
C(7)-C(13)-C(11)	111(7)
C(7)-C(13)-H(1c13)	108.88
C(11)-C(13)-H(1c13)	106.27
C(5)-C(1)-C(9)	112(6)
C(5)-C(1)-C(3)#0	111(6)
C(5)-C(1)-H(1c1)	107.2
C(9)-C(1)-C(3)#0	111(6)
C(9)-C(1)-H(1c1)	106.58
C(3)#0-C(1)-H(1c1)	108.15
Br(4)-N(1)-Br(6)#0	72.8(11)
Br(4)-N(1)-Br(7)#0	116.2(17)
Br(4)-N(1)-C(5)	90(4)
Br(4)-N(1)-C(2)#0	126(4)
Br(4)-N(1)-H(1n1)	21.05
Br(4)-N(1)-H(2n1)	106.85
Br(6)#0-N(1)-Br(7)#0	69.6(10)
Br(6)#0-N(1)-C(5)	159(5)
Br(6)#0-N(1)-C(2)#0	88(3)
Br(6)#0-N(1)-H(1n1)	55.68
Br(6)#0-N(1)-H(2n1)	65.86
Br(7)#0-N(1)-C(5)	109(4)
Br(7)#0-N(1)-C(2)#0	102(4)
Br(7)#0-N(1)-H(1n1)	114.02
Br(7)#0-N(1)-H(2n1)	9.37
C(5)-N(1)-C(2)#0	113(6)
C(5)-N(1)-H(1n1)	109.47

---

C(5)-N(1)-H(2n1)	109.47
C(2)#0-N(1)-H(1n1)	109.48
C(2)#0-N(1)-H(2n1)	109.48
H(1n1)-N(1)-H(2n1)	105.83
C(11)-C(4)-C(14)#0	115(8)
C(11)-C(4)-H(1c4)	109.47
C(11)-C(4)-H(2c4)	109.47
C(14)#0-C(4)-H(1c4)	109.48
C(14)#0-C(4)-H(2c4)	109.48
H(1c4)-C(4)-H(2c4)	102.96
C(1)-C(5)-N(1)	111(6)
C(1)-C(5)-H(1c5)	109.48
C(1)-C(5)-H(2c5)	109.48
N(1)-C(5)-H(1c5)	109.47
N(1)-C(5)-H(2c5)	109.47
H(1c5)-C(5)-H(2c5)	108.14
Br(2)#0-N(2)-Br(7)#0	104.7(19)
Br(2)#0-N(2)-C(7)#0	114(4)
Br(2)#0-N(2)-C(14)	98(5)
Br(2)#0-N(2)-H(1n2)	107.51
Br(2)#0-N(2)-H(2n2)	11.64
Br(7)#0-N(2)-C(7)#0	90(4)
Br(7)#0-N(2)-C(14)	133(5)
Br(7)#0-N(2)-H(1n2)	23.91
Br(7)#0-N(2)-H(2n2)	94.46
C(7)#0-N(2)-C(14)	117(6)
C(7)#0-N(2)-H(1n2)	109.47
C(7)#0-N(2)-H(2n2)	109.47
C(14)-N(2)-H(1n2)	109.47
C(14)-N(2)-H(2n2)	109.46
H(1n2)-N(2)-H(2n2)	100.33
C(2)-C(6)-C(3)	113(7)
C(2)-C(6)-H(1c6)	109.46
C(2)-C(6)-H(2c6)	109.46
C(3)-C(6)-H(1c6)	109.47
C(3)-C(6)-H(2c6)	109.47



---

H(1c6)-C(6)-H(2c6)	105.57
C(1)-C(9)-N(3)#0	117(6)
C(1)-C(9)-H(1c9)	109.47
C(1)-C(9)-H(2c9)	109.47
N(3)#0-C(9)-H(1c9)	109.47
N(3)#0-C(9)-H(2c9)	109.46
H(1c9)-C(9)-H(2c9)	101.36
C(13)-C(10)-N(4)	117(7)
C(13)-C(10)-H(1c10)	109.47
C(13)-C(10)-H(2c10)	109.47
N(4)-C(10)-H(1c10)	109.47
N(4)-C(10)-H(2c10)	109.48
H(1c10)-C(10)-H(2c10)	100.15
N(1)#0-C(2)-C(6)	115(6)
N(1)#0-C(2)-H(1c2)	109.46
N(1)#0-C(2)-H(2c2)	109.46
C(6)-C(2)-H(1c2)	109.48
C(6)-C(2)-H(2c2)	109.48
H(1c2)-C(2)-H(2c2)	103.66
Br(1)#0-N(3)-Br(2)#0	145(2)
Br(1)#0-N(3)-Br(3)#0	74.8(14)
Br(1)#0-N(3)-Br(5)#0	70.0(12)
Br(1)#0-N(3)-C(9)#0	100(4)
Br(1)#0-N(3)-H(1n3)	70.35
Br(1)#0-N(3)-H(2n3)	46.86
Br(1)#0-N(3)-H(3n3)	148.3
Br(2)#0-N(3)-Br(3)#0	93.5(15)
Br(2)#0-N(3)-Br(5)#0	74.6(14)
Br(2)#0-N(3)-C(9)#0	116(4)
Br(2)#0-N(3)-H(1n3)	94.17
Br(2)#0-N(3)-H(2n3)	117.39
Br(2)#0-N(3)-H(3n3)	15.32
Br(3)#0-N(3)-Br(5)#0	71.0(12)
Br(3)#0-N(3)-C(9)#0	112(4)
Br(3)#0-N(3)-H(1n3)	129.3
Br(3)#0-N(3)-H(2n3)	28.02

---

Br(3)#0-N(3)-H(3n3)	82.98
Br(5)#0-N(3)-C(9)#0	169(5)
Br(5)#0-N(3)-H(1n3)	63.18
Br(5)#0-N(3)-H(2n3)	67.43
Br(5)#0-N(3)-H(3n3)	81.61
C(9)#0-N(3)-H(1n3)	109.48
C(9)#0-N(3)-H(2n3)	109.48
C(9)#0-N(3)-H(3n3)	109.48
H(1n3)-N(3)-H(2n3)	109.48
H(1n3)-N(3)-H(3n3)	109.46
H(2n3)-N(3)-H(3n3)	109.46
C(1)#0-C(3)-C(6)	116(7)
C(1)#0-C(3)-H(1c3)	109.46
C(1)#0-C(3)-H(2c3)	109.47
C(6)-C(3)-H(1c3)	109.47
C(6)-C(3)-H(2c3)	109.47
H(1c3)-C(3)-H(2c3)	101.59
C(13)-C(7)-N(2)#0	110(7)
C(13)-C(7)-H(1c7)	109.46
C(13)-C(7)-H(2c7)	109.46
N(2)#0-C(7)-H(1c7)	109.47
N(2)#0-C(7)-H(2c7)	109.47
H(1c7)-C(7)-H(2c7)	108.59
C(13)-C(11)-C(4)	116(7)
C(13)-C(11)-H(1c11)	109.48
C(13)-C(11)-H(2c11)	109.47
C(4)-C(11)-H(1c11)	109.47
C(4)-C(11)-H(2c11)	109.47
H(1c11)-C(11)-H(2c11)	102
C(4)#0-C(14)-N(2)	113(7)
C(4)#0-C(14)-H(1c14)	109.46
C(4)#0-C(14)-H(2c14)	109.46
N(2)-C(14)-H(1c14)	109.48
N(2)-C(14)-H(2c14)	109.48
H(1c14)-C(14)-H(2c14)	106
Br(1)-N(4)-Br(3)#0	75.4(13)

---

Br(1)-N(4)-C(10)	167(5)
Br(1)-N(4)-H(1n4)	67.08
Br(1)-N(4)-H(2n4)	82.9
Br(1)-N(4)-H(3n4)	62.45
Br(3)#0-N(4)-C(10)	117(4)
Br(3)#0-N(4)-H(1n4)	108.55
Br(3)#0-N(4)-H(2n4)	8.08
Br(3)#0-N(4)-H(3n4)	102.83
C(10)-N(4)-H(1n4)	109.46
C(10)-N(4)-H(2n4)	109.47
C(10)-N(4)-H(3n4)	109.46
H(1n4)-N(4)-H(2n4)	109.48
H(1n4)-N(4)-H(3n4)	109.47
H(2n4)-N(4)-H(3n4)	109.48

---

Table 1. Crystal data and structure refinement for C<sub>6</sub> H<sub>5</sub> Br<sub>3</sub> N<sub>2</sub> Pb<sub>1</sub> at 296.7 K.

Empirical formula	C <sub>6</sub> H <sub>5</sub> Br <sub>3</sub> N <sub>2</sub> Pb <sub>1</sub>
Formula weight	552
Temperature	296.7 K
Wavelength	0.71073 Å
Crystal system	monoclinic
Space group	C 1 2/m 1
Unit cell dimensions	a = 21.5052(9) Å, α = 90° b = 6.1867(4) Å, β = 92.184(3)° c = 8.3273(3) Å, γ = 90°
Volume	1107.11(9) Å <sup>3</sup>
Z	4
Density (calculated)	3.3119 g/cm <sup>3</sup>
Absorption coefficient	26.018 mm <sup>-1</sup>
F(000)	968
Crystal size	0.1 x 0.08 x 0.03 mm <sup>3</sup>
θ range for data collection	3.04 to 29.14°
Index ranges	-22 ≤ h ≤ 29, -8 ≤ k ≤ 7, -11 ≤ l ≤ 11
Reflections collected	4756
Independent reflections	1432 [R <sub>int</sub> = 0.0216]
Completeness to θ = 27.62°	98%
Refinement method	Full-matrix least-squares on F <sup>2</sup>
Data / restraints / parameters	1432 / 0 / 73
Goodness-of-fit	1.62
Final R indices [I > 2σ(I)]	R <sub>obs</sub> = 0.0219, wR <sub>obs</sub> = 0.0585
R indices [all data]	R <sub>all</sub> = 0.0249, wR <sub>all</sub> = 0.0591
Extinction coefficient	?
Largest diff. peak and hole	0.55 and -1.16 e·Å <sup>-3</sup>

$$R = \frac{\sum ||F_o| - |F_c||}{\sum |F_o|}, wR = \left\{ \frac{\sum [w(|F_o|^2 - |F_c|^2)^2]}{\sum [w(|F_o|^4)]} \right\}^{1/2} \text{ and } w = 1/(\sigma^2(I) + 0.0004I^2)$$

Table 2. Atomic coordinates (x10<sup>4</sup>) and equivalent isotropic displacement parameters (Å<sup>2</sup>x10<sup>3</sup>) for C<sub>6</sub> H<sub>5</sub> Br<sub>3</sub> N<sub>2</sub> Pb<sub>1</sub> at 296.7 K with estimated standard deviations in parentheses.

Label	x	y	z	Occupancy	U <sub>eq</sub> <sup>*</sup>
Pb(1)	4857(1)	0	2448(1)	1	30(1)
Br(1)	3962(1)	0	-171(1)	1	37(1)
Br(2)	9730(1)	0	2541(1)	1	44(1)

Br(3)	4001(1)	0	4982(1)	1	35(1)
N(1)	7791(4)	0	11671(9)	1	64(3)
N(2)	8766(3)	0	6653(7)	1	39(2)
C(1)	7711(4)	0	5862(10)	1	43(3)
C(2)	7894(4)	0	10369(11)	1	46(3)
C(3)	8324(4)	0	5478(9)	1	38(2)
C(4)	7548(4)	0	7462(9)	1	40(3)
C(5)	8027(4)	0	8640(9)	1	39(2)
C(6)	8641(3)	0	8220(9)	1	36(2)
H(1c1)	7392.37	0	5022.54	1	51.1
H(1c3)	8436.82	0	4373	1	45.9
H(1c4)	7119.23	0	7746.98	1	47.9
H(1c6)	8971.45	0	9029.42	1	43.6
H(1n2)	9153.49	0	6388.33	1	47.1

\* $U_{eq}$  is defined as one third of the trace of the orthogonalized  $U_{ij}$  tensor.

Table 3. Anisotropic displacement parameters ( $\text{\AA}^2 \times 10^3$ ) for C6 H5 Br3 N2 Pb1 at 296.7 K with estimated standard deviations in parentheses.

Label	$U_{11}$	$U_{22}$	$U_{33}$	$U_{12}$	$U_{13}$	$U_{23}$
Pb(1)	29(1)	34(1)	27(1)	0	0(1)	0
Br(1)	34(1)	40(1)	36(1)	0	-5(1)	0
Br(2)	35(1)	36(1)	62(1)	0	-1(1)	0
Br(3)	31(1)	40(1)	36(1)	0	4(1)	0
N(1)	77(6)	71(6)	43(4)	0	7(4)	0
N(2)	33(3)	30(4)	54(4)	0	2(3)	0
C(1)	41(4)	36(5)	50(5)	0	-11(4)	0
C(2)	47(5)	37(5)	54(5)	0	-5(4)	0
C(3)	41(4)	31(4)	43(4)	0	2(3)	0
C(4)	28(4)	32(4)	59(5)	0	-4(3)	0
C(5)	37(4)	30(4)	50(4)	0	-1(3)	0
C(6)	34(4)	20(4)	54(5)	0	-5(3)	0

The anisotropic displacement factor exponent takes the form:  $-2\pi^2[h^2a^{*2}U_{11} + \dots + 2hka^*b^*U_{12}]$ .

Table 4. Bond lengths [ $\text{\AA}$ ] for C6 H5 Br3 N2 Pb1 at 296.7 K with estimated standard deviations in parentheses.

Label	Distances
Pb(1)-Br(1)	2.8539(8)
Pb(1)-Br(1)#0	3.2277(8)
Pb(1)-Br(2)#0	3.1065(4)
Pb(1)-Br(2)#0	3.1065(4)
Pb(1)-Br(3)	2.8516(8)
Pb(1)-Br(3)#0	3.1949(8)
Br(1)-N(1)#0	3.925(9)
Br(2)-N(2)#0	3.277(6)
Br(3)-N(2)#0	3.437(3)
Br(3)-N(2)#0	3.437(3)
N(1)-C(2)	1.115(12)
N(2)-C(3)	1.337(10)
N(2)-C(6)	1.343(10)
N(2)-H(1n2)	0.87
C(1)-C(3)	1.369(11)
C(1)-C(4)	1.392(11)
C(1)-H(1c1)	0.96
C(2)-C(5)	1.478(12)
C(3)-H(1c3)	0.96
C(4)-C(5)	1.395(11)
C(4)-H(1c4)	0.96
C(5)-C(6)	1.380(11)
C(6)-H(1c6)	0.96

Table 5. Bond angles [ $^{\circ}$ ] for C6 H5 Br3 N2 Pb1 at 296.7 K with estimated standard deviations in parentheses.

Label	Angles
Br(1)-Pb(1)-Br(1)#0	94.25(2)
Br(1)-Pb(1)-Br(2)#0	87.808(15)
Br(1)-Pb(1)-Br(2)#0	87.808(15)
Br(1)-Pb(1)-Br(3)	97.47(2)
Br(1)-Pb(1)-Br(3)#0	172.22(2)
Br(1)#0-Pb(1)-Br(2)#0	94.944(15)
Br(1)#0-Pb(1)-Br(2)#0	94.944(15)

---

Br(1)#0-Pb(1)-Br(3)	168.28(2)
Br(1)#0-Pb(1)-Br(3)#0	77.964(19)
Br(2)#0-Pb(1)-Br(2)#0	169.45(2)
Br(2)#0-Pb(1)-Br(3)	85.532(15)
Br(2)#0-Pb(1)-Br(3)#0	92.821(15)
Br(2)#0-Pb(1)-Br(3)	85.532(15)
Br(2)#0-Pb(1)-Br(3)#0	92.821(15)
Br(3)-Pb(1)-Br(3)#0	90.31(2)
Pb(1)-Br(1)-Pb(1)#0	85.75(2)
Pb(1)-Br(1)-N(1)#0	148.74(12)
Pb(1)#0-Br(1)-N(1)#0	125.51(12)
Pb(1)#0-Br(2)-Pb(1)#0	169.45(3)
Pb(1)#0-Br(2)-N(2)#0	85.320(16)
Pb(1)#0-Br(2)-N(2)#0	85.320(16)
Pb(1)-Br(3)-Pb(1)#0	89.69(2)
Pb(1)-Br(3)-N(2)#0	114.12(10)
Pb(1)-Br(3)-N(2)#0	114.12(10)
Pb(1)#0-Br(3)-N(2)#0	81.38(10)
Pb(1)#0-Br(3)-N(2)#0	81.38(10)
N(2)#0-Br(3)-N(2)#0	128.30(13)
Br(1)#0-N(1)-C(2)	85.2(6)
Br(2)#0-N(2)-Br(3)#0	85.62(11)
Br(2)#0-N(2)-Br(3)#0	85.62(11)
Br(2)#0-N(2)-C(3)	144.8(5)
Br(2)#0-N(2)-C(6)	91.9(4)
Br(2)#0-N(2)-H(1n2)	26.47
Br(3)#0-N(2)-Br(3)#0	128.30(18)
Br(3)#0-N(2)-C(3)	79.35(19)
Br(3)#0-N(2)-C(6)	115.57(10)
Br(3)#0-N(2)-H(1n2)	74.95
Br(3)#0-N(2)-C(3)	79.35(19)
Br(3)#0-N(2)-C(6)	115.57(10)
Br(3)#0-N(2)-H(1n2)	74.95
C(3)-N(2)-C(6)	123.3(7)
C(3)-N(2)-H(1n2)	118.36
C(6)-N(2)-H(1n2)	118.36

---

C(3)-C(1)-C(4)	120.3(7)
C(3)-C(1)-H(1c1)	119.85
C(4)-C(1)-H(1c1)	119.85
N(1)-C(2)-C(5)	179.6(9)
N(2)-C(3)-C(1)	119.5(7)
N(2)-C(3)-H(1c3)	120.24
C(1)-C(3)-H(1c3)	120.24
C(1)-C(4)-C(5)	117.8(7)
C(1)-C(4)-H(1c4)	121.09
C(5)-C(4)-H(1c4)	121.09
C(2)-C(5)-C(4)	121.4(7)
C(2)-C(5)-C(6)	117.9(7)
C(4)-C(5)-C(6)	120.7(7)
N(2)-C(6)-C(5)	118.3(7)
N(2)-C(6)-H(1c6)	120.83
C(5)-C(6)-H(1c6)	120.83

---



Table 1. Crystal data and structure refinement for C10 H22 Br4 N2 Pb1 at 293 K.

Empirical formula	C10 H22 Br4 N2 Pb1
Formula weight	697.1
Temperature	293 K
Wavelength	0.71073 Å
Crystal system	monoclinic
Space group	P 1 c 1
Unit cell dimensions	a = 12.2301(9) Å, $\alpha = 90^\circ$ b = 12.2474(8) Å, $\beta = 90.399(3)^\circ$ c = 11.9557(8) Å, $\gamma = 90^\circ$
Volume	1790.8(2) Å <sup>3</sup>
Z	4
Density (calculated)	2.5856 g/cm <sup>3</sup>
Absorption coefficient	18.331 mm <sup>-1</sup>
F(000)	1272
Crystal size	? x ? x ? mm <sup>3</sup>
$\theta$ range for data collection	2.35 to 30.67°
Index ranges	-17<=h<=17, -16<=k<=17, -17<=l<=17
Reflections collected	71704
Independent reflections	6486 [R <sub>int</sub> = 0.0496]
Completeness to $\theta = 30.67^\circ$	99%
Refinement method	Full-matrix least-squares on F <sup>2</sup>
Data / restraints / parameters	6486 / 0 / 190
Goodness-of-fit	1.85
Final R indices [I>2 $\sigma$ (I)]	R <sub>obs</sub> = 0.0315, wR <sub>obs</sub> = 0.0801
R indices [all data]	R <sub>all</sub> = 0.0405, wR <sub>all</sub> = 0.0823
Extinction coefficient	810(130)
Largest diff. peak and hole	0.99 and -0.83 e <sup>-</sup> Å <sup>-3</sup>

$$R = \frac{\sum ||F_o| - |F_c||}{\sum |F_o|}, wR = \left\{ \frac{\sum [w(|F_o|^2 - |F_c|^2)^2]}{\sum [w(|F_o|^4)]} \right\}^{1/2} \text{ and } w = 1/(\sigma^2(I) + 0.0004I^2)$$

Table 2. Atomic coordinates (x10<sup>4</sup>) and equivalent isotropic displacement parameters (Å<sup>2</sup>x10<sup>3</sup>) for C10 H22 Br4 N2 Pb1 at 293 K with estimated standard deviations in parentheses.

Label	x	y	z	Occupancy	U <sub>eq</sub> <sup>*</sup>
Pb(1)	9205(1)	9694(1)	3538(2)	1	32(1)
Pb(2)	9197(1)	4698(1)	3520(2)	1	32(1)
Br(1)	9124(3)	2288(2)	3105(3)	1	47(1)

---

Br(2)	9280(3)	4536(2)	5952(3)	1	48(1)
Br(3)	6779(2)	4471(2)	3575(4)	1	43(1)
Br(4)	6777(2)	9328(2)	3574(4)	1	44(1)
Br(5)	1648(2)	4310(3)	3480(4)	1	49(1)
Br(6)	11633(3)	9484(3)	3469(4)	1	50(1)
Br(7)	9251(3)	7320(2)	3952(4)	1	50(1)
Br(8)	9115(3)	9527(2)	1096(3)	1	50(1)
N(1)	1261(12)	2713(13)	1226(14)	1	35(4)
C(1)	6659(12)	6826(13)	5587(14)	1	31(4)
C(2)	6687(18)	6940(18)	1770(20)	1	60(7)
C(3)	1808(13)	1558(14)	1427(16)	1	40(5)
N(2)	11266(12)	7669(11)	1421(16)	1	27(4)
N(3)	7110(20)	7340(18)	750(30)	1	85(9)
C(4)	4795(19)	7530(20)	1060(20)	1	46(8)
C(5)	11742(13)	8244(14)	398(16)	1	26(4)
C(6)	5504(14)	6806(16)	5428(18)	1	45(6)
C(7)	5463(14)	6665(16)	1661(17)	1	45(6)
C(8)	2960(11)	8415(13)	637(14)	1	28(4)
C(9)	2993(12)	1898(13)	1833(15)	1	30(4)
C(10)	3054(11)	6939(13)	2005(14)	1	25(4)
C(11)	4790(17)	7405(17)	6200(20)	1	31(6)
C(12)	6491(15)	8415(15)	420(17)	1	47(5)
C(13)	3571(17)	2514(17)	860(20)	1	37(7)
C(14)	5366(19)	8150(20)	280(20)	1	77(9)
C(15)	1833(14)	6773(15)	1850(16)	1	40(5)
C(16)	1752(15)	3347(16)	289(17)	1	36(5)
C(17)	6447(17)	8418(18)	6750(20)	1	50(6)
N(4)	7137(12)	7908(13)	5870(15)	1	36(4)
C(18)	3582(17)	7381(17)	910(18)	1	30(6)
C(19)	3036(10)	3611(11)	707(13)	1	25(3)
C(20)	5334(14)	8424(14)	6560(15)	1	40(5)
H(1n1)	1297.52	3094.41	1838.66	1	42.3
H(2n1)	563.8	2628.75	1102.84	1	42.3
H(1c1)	7009.78	6540.25	4933.59	1	37.3
H(2c1)	6861.86	6305	6151.81	1	37.3
H(1c2)	6790.11	7476.34	2346.19	1	71.5

---

H(2c2)	7083.18	6298.47	1992.93	1	71.5
H(1c3)	1857.27	1175.33	727.93	1	47.8
H(2c3)	1437.7	1187.35	2021.21	1	47.8
H(1n2)	11161.42	8143.91	1950.88	1	32.4
H(2n2)	10591.72	7484.15	1282.95	1	32.4
H(1n3)	7023.23	6852.59	229.79	1	102.1
H(2n3)	7807.47	7480.96	837.48	1	102.1
H(1c4)	4695.99	8031.57	1670.39	1	55.4
H(1c5)	11654.22	7785.73	-248.09	1	31.7
H(2c5)	11392.25	8939.75	301.1	1	31.7
H(1c6)	5259.64	6063.33	5370.27	1	54.4
H(2c6)	5330.68	7007.01	4671.42	1	54.4
H(1c7)	5378.65	5978.84	1282.01	1	54.6
H(2c7)	5165.56	6539.25	2389.97	1	54.6
H(1c8)	3047.48	8928.23	1237.42	1	33.4
H(2c8)	3291.89	8770.4	9.43	1	33.4
H(1c9)	2938.15	2371.27	2469.93	1	35.8
H(2c9)	3403.99	1254.66	2021.76	1	35.8
H(1c10)	3389.83	6257.44	2206.04	1	30.4
H(2c10)	3182.63	7446.66	2602.96	1	30.4
H(1c11)	4704.47	6962.93	6852.15	1	37.2
H(1c12)	6571.03	8944.05	1007.33	1	56.3
H(2c12)	6775.71	8690.65	-271.41	1	56.3
H(1c13)	3510.58	2145.35	154.58	1	44.6
H(1c14)	5248.56	7856.47	-456.23	1	92.6
H(2c14)	4961.71	8806.49	113.53	1	92.6
H(1c15)	1705.46	6149.06	1381.54	1	48.1
H(2c15)	1516.46	6558.65	2549.28	1	48.1
H(1c16)	1361.7	4021.48	194.5	1	42.9
H(2c16)	1765.5	2903.8	-373.22	1	42.9
H(1c17)	6694.54	9148.99	6888.78	1	60.3
H(2c17)	6598.92	8078.54	7457.4	1	60.3
H(1n4)	7798.66	7820.41	6127.17	1	43.2
H(2n4)	7135.54	8320.39	5277.84	1	43.2
H(1c18)	3525.77	6885.84	289.8	1	36.1
H(1c19)	3409.18	4009.72	132.84	1	29.5

H(2c19)	3023.85	3989.24	1409.95	1	29.5
H(1c20)	4969.96	8709.79	7205.23	1	48.1
H(2c20)	5152.75	9002.2	6048.46	1	48.1

\* $U_{eq}$  is defined as one third of the trace of the orthogonalized  $U_{ij}$  tensor.

Table 3. Anisotropic displacement parameters ( $\text{\AA}^2 \times 10^3$ ) for C10 H22 Br4 N2 Pb1 at 293 K with estimated standard deviations in parentheses.

Label	$U_{11}$	$U_{22}$	$U_{33}$	$U_{12}$	$U_{13}$	$U_{23}$
Pb(1)	39(1)	27(1)	28(1)	1(1)	1(1)	0(1)
Pb(2)	38(1)	28(1)	30(1)	1(1)	1(1)	1(1)
Br(1)	63(2)	19(1)	60(2)	-2(2)	0(2)	0(2)
Br(2)	31(2)	70(2)	41(2)	-7(2)	-1(2)	2(2)
Br(3)	31(1)	41(2)	57(2)	-2(2)	-1(2)	-2(2)
Br(4)	33(1)	39(2)	60(2)	3(2)	1(2)	2(2)
Br(5)	66(2)	44(2)	36(2)	3(2)	1(2)	-7(2)
Br(6)	64(2)	49(2)	39(2)	-9(2)	1(2)	-3(2)
Br(7)	28(1)	36(2)	87(3)	-2(2)	-1(2)	4(2)
Br(8)	54(2)	75(2)	19(2)	2(2)	0(2)	1(2)

The anisotropic displacement factor exponent takes the form:  $-2\pi^2[h^2a^{*2}U_{11} + \dots + 2hka^*b^*U_{12}]$ .

Table 4. Bond lengths [ $\text{\AA}$ ] for C10 H22 Br4 N2 Pb1 at 293 K with estimated standard deviations in parentheses.

Label	Distances
Pb(1)-Br(1)#0	3.220(3)
Pb(1)-Br(4)	3.005(3)
Pb(1)-Br(6)	2.982(3)
Pb(1)-Br(7)	2.950(3)
Pb(1)-Br(8)	2.928(4)
Pb(1)-Br(8)#0	3.206(4)
Pb(2)-Br(1)	2.994(3)
Pb(2)-Br(2)	2.916(4)
Pb(2)-Br(2)#0	3.211(4)
Pb(2)-Br(3)	2.971(3)
Pb(2)-Br(5)#0	3.036(3)
Pb(2)-Br(7)	3.253(3)
Br(1)-N(1)#0	3.496(16)

---

Br(1)-N(4)#0	3.607(17)
Br(2)-N(2)#0	3.673(15)
Br(2)-N(3)#0	3.51(2)
Br(3)-N(3)#0	3.44(3)
Br(4)-N(4)	3.277(17)
Br(5)-N(1)	3.361(17)
Br(6)-N(2)	3.335(17)
Br(7)-N(1)#0	3.653(16)
Br(7)-N(2)	3.939(18)
Br(7)-N(4)	3.542(16)
Br(8)-N(2)	3.498(15)
Br(8)-N(3)	3.65(2)
N(1)-C(3)	1.58(2)
N(1)-C(16)	1.49(3)
N(1)-H(1n1)	0.87
N(1)-H(2n1)	0.87
C(1)-C(6)	1.42(2)
C(1)-N(4)	1.49(2)
C(1)-H(1c1)	0.96
C(1)-H(2c1)	0.96
C(2)-N(3)	1.41(4)
C(2)-C(7)	1.54(3)
C(2)-H(1c2)	0.96
C(2)-H(2c2)	0.96
C(3)-C(9)	1.58(2)
C(3)-H(1c3)	0.96
C(3)-H(2c3)	0.96
N(2)-C(5)	1.53(3)
N(2)-C(15)#0	1.39(2)
N(2)-H(1n2)	0.87
N(2)-H(2n2)	0.87
N(3)-C(12)	1.57(3)
N(3)-H(1n3)	0.87
N(3)-H(2n3)	0.87
C(4)-C(7)	1.51(3)
C(4)-C(14)	1.40(4)

---

C(4)-C(18)	1.50(3)
C(4)-H(1c4)	0.96
C(5)-C(8)#0	1.53(2)
C(5)-H(1c5)	0.96
C(5)-H(2c5)	0.96
C(6)-C(11)	1.47(3)
C(6)-H(1c6)	0.96
C(6)-H(2c6)	0.96
C(7)-H(1c7)	0.96
C(7)-H(2c7)	0.96
C(8)-C(18)	1.51(3)
C(8)-H(1c8)	0.96
C(8)-H(2c8)	0.96
C(9)-C(13)	1.56(3)
C(9)-H(1c9)	0.96
C(9)-H(2c9)	0.96
C(10)-C(15)	1.52(2)
C(10)-C(18)	1.56(3)
C(10)-H(1c10)	0.96
C(10)-H(2c10)	0.96
C(11)-C(13)#0	1.54(3)
C(11)-C(20)	1.48(3)
C(11)-H(1c11)	0.96
C(12)-C(14)	1.42(3)
C(12)-H(1c12)	0.96
C(12)-H(2c12)	0.96
C(13)-C(19)	1.50(3)
C(13)-H(1c13)	0.96
C(14)-H(1c14)	0.96
C(14)-H(2c14)	0.96
C(15)-H(1c15)	0.96
C(15)-H(2c15)	0.96
C(16)-C(19)	1.68(2)
C(16)-H(1c16)	0.96
C(16)-H(2c16)	0.96
C(17)-N(4)	1.49(3)

---

C(17)-C(20)	1.38(3)
C(17)-H(1c17)	0.96
C(17)-H(2c17)	0.96
N(4)-H(1n4)	0.87
N(4)-H(2n4)	0.87
C(18)-H(1c18)	0.96
C(19)-H(1c19)	0.96
C(19)-H(2c19)	0.96
C(20)-H(1c20)	0.96
C(20)-H(2c20)	0.96

---

Table 5. Bond angles [°] for C10 H22 Br4 N2 Pb1 at 293 K with estimated standard deviations in parentheses.

---

Label	Angles
Br(1)#0-Pb(1)-Br(4)	96.92(9)
Br(1)#0-Pb(1)-Br(6)	96.32(9)
Br(1)#0-Pb(1)-Br(7)	179.21(10)
Br(1)#0-Pb(1)-Br(8)	84.70(10)
Br(1)#0-Pb(1)-Br(8)#0	81.88(9)
Br(4)-Pb(1)-Br(6)	166.44(9)
Br(4)-Pb(1)-Br(7)	82.41(9)
Br(4)-Pb(1)-Br(8)	88.48(12)
Br(4)-Pb(1)-Br(8)#0	89.44(11)
Br(6)-Pb(1)-Br(7)	84.37(9)
Br(6)-Pb(1)-Br(8)	89.83(12)
Br(6)-Pb(1)-Br(8)#0	95.33(11)
Br(7)-Pb(1)-Br(8)	95.68(11)
Br(7)-Pb(1)-Br(8)#0	97.70(11)
Br(8)-Pb(1)-Br(8)#0	166.07(9)
Br(1)-Pb(2)-Br(2)	95.67(10)
Br(1)-Pb(2)-Br(2)#0	97.50(10)
Br(1)-Pb(2)-Br(3)	83.28(9)
Br(1)-Pb(2)-Br(5)#0	82.59(9)
Br(1)-Pb(2)-Br(7)	179.34(10)
Br(2)-Pb(2)-Br(2)#0	166.40(8)
Br(2)-Pb(2)-Br(3)	89.93(12)

---

Br(2)-Pb(2)-Br(5)#0	88.72(11)
Br(2)-Pb(2)-Br(7)	84.74(10)
Br(2)#0-Pb(2)-Br(3)	94.97(11)
Br(2)#0-Pb(2)-Br(5)#0	89.61(11)
Br(2)#0-Pb(2)-Br(7)	82.12(10)
Br(3)-Pb(2)-Br(5)#0	165.61(9)
Br(3)-Pb(2)-Br(7)	96.20(8)
Br(5)#0-Pb(2)-Br(7)	97.94(9)
Pb(1)#0-Br(1)-Pb(2)	160.92(15)
Pb(1)#0-Br(1)-N(1)#0	103.2(3)
Pb(1)#0-Br(1)-N(4)#0	94.2(3)
Pb(2)-Br(1)-N(1)#0	86.5(3)
Pb(2)-Br(1)-N(4)#0	102.0(3)
N(1)#0-Br(1)-N(4)#0	92.1(4)
Pb(2)-Br(2)-Pb(2)#0	158.77(11)
Pb(2)-Br(2)-N(2)#0	102.7(3)
Pb(2)-Br(2)-N(3)#0	87.5(5)
Pb(2)#0-Br(2)-N(2)#0	95.4(3)
Pb(2)#0-Br(2)-N(3)#0	103.1(5)
N(2)#0-Br(2)-N(3)#0	91.5(5)
Pb(2)-Br(3)-N(3)#0	87.9(4)
Pb(1)-Br(4)-N(4)	87.9(3)
Pb(2)#0-Br(5)-N(1)	88.3(3)
Pb(1)-Br(6)-N(2)	87.1(3)
Pb(1)-Br(7)-Pb(2)	161.09(16)
Pb(1)-Br(7)-N(1)#0	98.5(3)
Pb(1)-Br(7)-N(2)	77.0(2)
Pb(1)-Br(7)-N(4)	84.0(3)
Pb(2)-Br(7)-N(1)#0	96.9(3)
Pb(2)-Br(7)-N(2)	89.8(2)
Pb(2)-Br(7)-N(4)	106.8(3)
N(1)#0-Br(7)-N(2)	98.7(4)
N(1)#0-Br(7)-N(4)	90.6(4)
N(2)-Br(7)-N(4)	159.8(3)
Pb(1)-Br(8)-Pb(1)#0	158.29(11)
Pb(1)-Br(8)-N(2)	84.9(3)



---

Pb(1)-Br(8)-N(3)	100.6(5)
Pb(1)#0-Br(8)-N(2)	105.6(3)
Pb(1)#0-Br(8)-N(3)	98.0(5)
N(2)-Br(8)-N(3)	92.2(5)
Br(1)#0-N(1)-Br(5)	70.9(3)
Br(1)#0-N(1)-Br(7)#0	88.5(3)
Br(1)#0-N(1)-C(3)	95.0(9)
Br(1)#0-N(1)-C(16)	150.0(11)
Br(1)#0-N(1)-H(1n1)	64.75
Br(1)#0-N(1)-H(2n1)	49.87
Br(5)-N(1)-Br(7)#0	133.9(5)
Br(5)-N(1)-C(3)	110.0(10)
Br(5)-N(1)-C(16)	104.1(10)
Br(5)-N(1)-H(1n1)	6.18
Br(5)-N(1)-H(2n1)	109.69
Br(7)#0-N(1)-C(3)	112.6(10)
Br(7)#0-N(1)-C(16)	73.7(9)
Br(7)#0-N(1)-H(1n1)	131.55
Br(7)#0-N(1)-H(2n1)	38.69
C(3)-N(1)-C(16)	114.0(14)
C(3)-N(1)-H(1n1)	109.47
C(3)-N(1)-H(2n1)	109.47
C(16)-N(1)-H(1n1)	109.47
C(16)-N(1)-H(2n1)	109.47
H(1n1)-N(1)-H(2n1)	104.52
C(6)-C(1)-N(4)	115.7(14)
C(6)-C(1)-H(1c1)	109.47
C(6)-C(1)-H(2c1)	109.47
N(4)-C(1)-H(1c1)	109.47
N(4)-C(1)-H(2c1)	109.47
H(1c1)-C(1)-H(2c1)	102.45
N(3)-C(2)-C(7)	112(2)
N(3)-C(2)-H(1c2)	109.47
N(3)-C(2)-H(2c2)	109.47
C(7)-C(2)-H(1c2)	109.47
C(7)-C(2)-H(2c2)	109.47

---

H(1c2)-C(2)-H(2c2)	107.26
N(1)-C(3)-C(9)	101.4(12)
N(1)-C(3)-H(1c3)	109.47
N(1)-C(3)-H(2c3)	109.47
C(9)-C(3)-H(1c3)	109.47
C(9)-C(3)-H(2c3)	109.47
H(1c3)-C(3)-H(2c3)	116.49
Br(2)#0-N(2)-Br(6)	133.4(5)
Br(2)#0-N(2)-Br(7)	67.7(3)
Br(2)#0-N(2)-Br(8)	88.0(3)
Br(2)#0-N(2)-C(5)	118.1(11)
Br(2)#0-N(2)-C(15)#0	78.7(9)
Br(2)#0-N(2)-H(1n2)	120.13
Br(2)#0-N(2)-H(2n2)	32.27
Br(6)-N(2)-Br(7)	65.8(3)
Br(6)-N(2)-Br(8)	75.2(3)
Br(6)-N(2)-C(5)	103.3(9)
Br(6)-N(2)-C(15)#0	101.0(12)
Br(6)-N(2)-H(1n2)	16.2
Br(6)-N(2)-H(2n2)	115.82
Br(7)-N(2)-Br(8)	71.5(3)
Br(7)-N(2)-C(5)	155.2(10)
Br(7)-N(2)-C(15)#0	86.8(11)
Br(7)-N(2)-H(1n2)	54.36
Br(7)-N(2)-H(2n2)	61.32
Br(8)-N(2)-C(5)	84.3(8)
Br(8)-N(2)-C(15)#0	157.6(12)
Br(8)-N(2)-H(1n2)	62.08
Br(8)-N(2)-H(2n2)	55.74
C(5)-N(2)-C(15)#0	117.8(14)
C(5)-N(2)-H(1n2)	109.47
C(5)-N(2)-H(2n2)	109.47
C(15)#0-N(2)-H(1n2)	109.47
C(15)#0-N(2)-H(2n2)	109.47
H(1n2)-N(2)-H(2n2)	99.68
Br(2)#0-N(3)-Br(3)#0	73.5(5)

---

Br(2)#0-N(3)-Br(8)	88.2(6)
Br(2)#0-N(3)-C(2)	89.9(14)
Br(2)#0-N(3)-C(12)	158.4(15)
Br(2)#0-N(3)-H(1n3)	72.17
Br(2)#0-N(3)-H(2n3)	52.36
Br(3)#0-N(3)-Br(8)	129.4(9)
Br(3)#0-N(3)-C(2)	112.6(15)
Br(3)#0-N(3)-C(12)	107.1(16)
Br(3)#0-N(3)-H(1n3)	3.28
Br(3)#0-N(3)-H(2n3)	109.15
Br(8)-N(3)-C(2)	114.1(17)
Br(8)-N(3)-C(12)	74.7(11)
Br(8)-N(3)-H(1n3)	131.83
Br(8)-N(3)-H(2n3)	35.82
C(2)-N(3)-C(12)	109(2)
C(2)-N(3)-H(1n3)	109.47
C(2)-N(3)-H(2n3)	109.47
C(12)-N(3)-H(1n3)	109.47
C(12)-N(3)-H(2n3)	109.47
H(1n3)-N(3)-H(2n3)	109.95
C(7)-C(4)-C(14)	115(2)
C(7)-C(4)-C(18)	120(2)
C(7)-C(4)-H(1c4)	99.37
C(14)-C(4)-C(18)	119(2)
C(14)-C(4)-H(1c4)	102.78
C(18)-C(4)-H(1c4)	92.32
N(2)-C(5)-C(8)#0	106.8(14)
N(2)-C(5)-H(1c5)	109.47
N(2)-C(5)-H(2c5)	109.47
C(8)#0-C(5)-H(1c5)	109.47
C(8)#0-C(5)-H(2c5)	109.47
H(1c5)-C(5)-H(2c5)	112.02
C(1)-C(6)-C(11)	120.1(18)
C(1)-C(6)-H(1c6)	109.47
C(1)-C(6)-H(2c6)	109.47
C(11)-C(6)-H(1c6)	109.47

---

C(11)-C(6)-H(2c6)	109.47
H(1c6)-C(6)-H(2c6)	96.21
C(2)-C(7)-C(4)	114.2(18)
C(2)-C(7)-H(1c7)	109.47
C(2)-C(7)-H(2c7)	109.47
C(4)-C(7)-H(1c7)	109.47
C(4)-C(7)-H(2c7)	109.47
H(1c7)-C(7)-H(2c7)	104.3
C(5)#0-C(8)-C(18)	114.5(14)
C(5)#0-C(8)-H(1c8)	109.47
C(5)#0-C(8)-H(2c8)	109.47
C(18)-C(8)-H(1c8)	109.47
C(18)-C(8)-H(2c8)	109.47
H(1c8)-C(8)-H(2c8)	103.97
C(3)-C(9)-C(13)	108.5(15)
C(3)-C(9)-H(1c9)	109.47
C(3)-C(9)-H(2c9)	109.47
C(13)-C(9)-H(1c9)	109.47
C(13)-C(9)-H(2c9)	109.47
H(1c9)-C(9)-H(2c9)	110.42
C(15)-C(10)-C(18)	110.9(14)
C(15)-C(10)-H(1c10)	109.47
C(15)-C(10)-H(2c10)	109.47
C(18)-C(10)-H(1c10)	109.47
C(18)-C(10)-H(2c10)	109.47
H(1c10)-C(10)-H(2c10)	107.99
C(6)-C(11)-C(13)#0	117(2)
C(6)-C(11)-C(20)	109.7(17)
C(6)-C(11)-H(1c11)	107.33
C(13)#0-C(11)-C(20)	117.0(17)
C(13)#0-C(11)-H(1c11)	97.87
C(20)-C(11)-H(1c11)	106.72
N(3)-C(12)-C(14)	108.0(18)
N(3)-C(12)-H(1c12)	109.47
N(3)-C(12)-H(2c12)	109.47
C(14)-C(12)-H(1c12)	109.47

---

C(14)-C(12)-H(2c12)	109.47
H(1c12)-C(12)-H(2c12)	110.93
C(9)-C(13)-C(11)#0	106.2(19)
C(9)-C(13)-C(19)	108.9(17)
C(9)-C(13)-H(1c13)	113.26
C(11)#0-C(13)-C(19)	113.1(16)
C(11)#0-C(13)-H(1c13)	109.07
C(19)-C(13)-H(1c13)	106.36
C(4)-C(14)-C(12)	122(2)
C(4)-C(14)-H(1c14)	109.47
C(4)-C(14)-H(2c14)	109.47
C(12)-C(14)-H(1c14)	109.47
C(12)-C(14)-H(2c14)	109.47
H(1c14)-C(14)-H(2c14)	93.14
N(2)#0-C(15)-C(10)	115.2(15)
N(2)#0-C(15)-H(1c15)	109.47
N(2)#0-C(15)-H(2c15)	109.47
C(10)-C(15)-H(1c15)	109.47
C(10)-C(15)-H(2c15)	109.47
H(1c15)-C(15)-H(2c15)	103.03
N(1)-C(16)-C(19)	104.9(14)
N(1)-C(16)-H(1c16)	109.47
N(1)-C(16)-H(2c16)	109.47
C(19)-C(16)-H(1c16)	109.47
C(19)-C(16)-H(2c16)	109.47
H(1c16)-C(16)-H(2c16)	113.67
N(4)-C(17)-C(20)	116.8(18)
N(4)-C(17)-H(1c17)	109.47
N(4)-C(17)-H(2c17)	109.47
C(20)-C(17)-H(1c17)	109.47
C(20)-C(17)-H(2c17)	109.47
H(1c17)-C(17)-H(2c17)	101.03
Br(1)#0-N(4)-Br(4)	137.9(5)
Br(1)#0-N(4)-Br(7)	88.6(3)
Br(1)#0-N(4)-C(1)	111.8(10)
Br(1)#0-N(4)-C(17)	83.6(11)

---

Br(1)#0-N(4)-H(1n4)	27.16
Br(1)#0-N(4)-H(2n4)	129.75
Br(4)-N(4)-Br(7)	70.1(3)
Br(4)-N(4)-C(1)	103.4(10)
Br(4)-N(4)-C(17)	107.2(11)
Br(4)-N(4)-H(1n4)	118.71
Br(4)-N(4)-H(2n4)	8.21
Br(7)-N(4)-C(1)	87.6(9)
Br(7)-N(4)-C(17)	164.1(12)
Br(7)-N(4)-H(1n4)	61.46
Br(7)-N(4)-H(2n4)	65.67
C(1)-N(4)-C(17)	108.1(14)
C(1)-N(4)-H(1n4)	109.47
C(1)-N(4)-H(2n4)	109.47
C(17)-N(4)-H(1n4)	109.47
C(17)-N(4)-H(2n4)	109.47
H(1n4)-N(4)-H(2n4)	110.84
C(4)-C(18)-C(8)	114.9(17)
C(4)-C(18)-C(10)	110.6(18)
C(4)-C(18)-H(1c18)	103.61
C(8)-C(18)-C(10)	105.1(15)
C(8)-C(18)-H(1c18)	109.23
C(10)-C(18)-H(1c18)	113.61
C(13)-C(19)-C(16)	105.7(13)
C(13)-C(19)-H(1c19)	109.47
C(13)-C(19)-H(2c19)	109.47
C(16)-C(19)-H(1c19)	109.47
C(16)-C(19)-H(2c19)	109.47
H(1c19)-C(19)-H(2c19)	113.02
C(11)-C(20)-C(17)	119.0(17)
C(11)-C(20)-H(1c20)	109.47
C(11)-C(20)-H(2c20)	109.47
C(17)-C(20)-H(1c20)	109.47
C(17)-C(20)-H(2c20)	109.47
H(1c20)-C(20)-H(2c20)	97.86

---

Table 1. Crystal data and structure refinement for C<sub>6</sub>H<sub>16</sub>Br<sub>4</sub>N<sub>2</sub>Pb<sub>1</sub> at 293 K.

Empirical formula	C <sub>6</sub> H <sub>16</sub> Br <sub>4</sub> N <sub>2</sub> Pb <sub>1</sub>
Formula weight	643
Temperature	293 K
Wavelength	0.71073 Å
Crystal system	orthorhombic
Space group	P c a 21
Unit cell dimensions	a = 17.7632(5) Å, α = 90° b = 10.2507(2) Å, β = 90° c = 7.8349(3) Å, γ = 90°
Volume	1426.62(7) Å <sup>3</sup>
Z	4
Density (calculated)	2.9938 g/cm <sup>3</sup>
Absorption coefficient	22.997 mm <sup>-1</sup>
F(000)	1152
Crystal size	? x ? x ? mm <sup>3</sup>
θ range for data collection	1.99 to 35.56°
Index ranges	-27 ≤ h ≤ 28, -14 ≤ k ≤ 14, -12 ≤ l ≤ 12
Reflections collected	86881
Independent reflections	2599 [R <sub>int</sub> = 0.1476]
Completeness to θ = 34.02°	98%
Refinement method	Full-matrix least-squares on F <sup>2</sup>
Data / restraints / parameters	2599 / 0 / 119
Goodness-of-fit	1.57
Final R indices [I > 2σ(I)]	R <sub>obs</sub> = 0.0361, wR <sub>obs</sub> = 0.0886
R indices [all data]	R <sub>all</sub> = 0.0422, wR <sub>all</sub> = 0.0902
Extinction coefficient	?
Largest diff. peak and hole	0.64 and -1.33 e·Å <sup>-3</sup>

$$R = \frac{\sum ||F_o| - |F_c||}{\sum |F_o|}, wR = \left\{ \frac{\sum [w(|F_o|^2 - |F_c|^2)^2]}{\sum [w(|F_o|^4)]} \right\}^{1/2} \text{ and } w = 1/(\sigma^2(I) + 0.0004I^2)$$

Table 2. Atomic coordinates (x10<sup>4</sup>) and equivalent isotropic displacement parameters (Å<sup>2</sup>x10<sup>3</sup>) for C<sub>6</sub>H<sub>16</sub>Br<sub>4</sub>N<sub>2</sub>Pb<sub>1</sub> at 293 K with estimated standard deviations in parentheses.

Label	x	y	z	Occupancy	U <sub>eq</sub> <sup>*</sup>
Pb(1)	6227(1)	5072(1)	7204(2)	1	40(1)
Br(1)	8473(1)	2066(2)	1980(3)	1	52(1)
Br(2)	6125(1)	7854(2)	7448(4)	1	54(1)

Br(3)	7333(1)	5198(2)	10215(2)	1	50(1)
Br(4)	5371(1)	5028(2)	3935(3)	1	55(1)
N(1)	6180(6)	7640(11)	1775(18)	1	51(5)
N(2)	6659(7)	2638(11)	2810(16)	1	51(5)
C(1)	6107(7)	1815(13)	1850(19)	1	46(5)
C(2)	6090(7)	441(13)	2470(20)	1	47(5)
C(3)	6789(9)	8319(15)	2710(20)	1	62(7)
C(4)	5464(7)	-324(14)	1500(20)	1	59(6)
C(5)	6850(7)	9704(13)	2120(30)	1	61(6)
C(6)	5440(7)	8293(14)	2050(30)	1	63(6)
H(1n1)	6283.87	7634.34	690.26	1	61.4
H(2n1)	6153.32	6833.78	2116.67	1	61.4
H(1n2)	6599.94	3451.91	2524.1	1	61.5
H(2n2)	6582.19	2550.4	3900.8	1	61.5
H(3n2)	7114.3	2390.99	2563.19	1	61.5
H(1c1)	6230.43	1825.61	657.52	1	55.1
H(2c1)	5613.45	2188.5	1946.96	1	55.1
H(1c2)	6001.51	478.31	3678.58	1	56.6
H(1c3)	6681.4	8304.11	3914.74	1	74.6
H(2c3)	7258.16	7878.7	2517.81	1	74.6
H(1c4)	4984.71	76.67	1718.59	1	71.2
H(2c4)	5556.63	-282.26	299	1	71.2
H(1c5)	6956.98	9719.04	920.52	1	73.3
H(2c5)	7251.39	10130.77	2722.67	1	73.3
H(1c6)	5056.82	7840.24	1425.63	1	75.8
H(2c6)	5310.07	8248.67	3242.16	1	75.8

\* $U_{eq}$  is defined as one third of the trace of the orthogonalized  $U_{ij}$  tensor.

Table 3. Anisotropic displacement parameters ( $\text{\AA}^2 \times 10^3$ ) for C6 H16 Br4 N2 Pb1 at 293 K with estimated standard deviations in parentheses.

Label	$U_{11}$	$U_{22}$	$U_{33}$	$U_{12}$	$U_{13}$	$U_{23}$
Pb(1)	34(1)	43(1)	42(1)	1(1)	0(1)	-3(1)
Br(1)	41(1)	52(1)	62(2)	-1(1)	2(1)	2(1)
Br(2)	50(1)	47(1)	66(2)	7(1)	1(1)	-3(1)



Br(3)	46(1)	58(1)	45(1)	6(1)	-7(1)	-1(1)
Br(4)	50(1)	62(1)	54(1)	-2(1)	-11(1)	-1(1)
N(1)	41(6)	44(7)	68(11)	3(5)	4(7)	-10(7)
N(2)	59(8)	42(7)	53(9)	5(6)	8(6)	1(6)
C(1)	50(8)	42(7)	46(11)	10(6)	1(8)	0(7)
C(2)	39(7)	48(7)	55(10)	1(6)	3(7)	4(8)
C(3)	46(9)	63(10)	78(14)	11(8)	-6(8)	7(9)
C(4)	29(8)	51(9)	98(15)	9(6)	2(8)	-15(9)
C(5)	34(7)	52(8)	97(14)	5(6)	-10(12)	1(11)
C(6)	31(7)	60(9)	98(15)	-7(6)	-6(10)	-23(11)

The anisotropic displacement factor exponent takes the form:  $-2\pi^2[h^2a^{*2}U_{11} + \dots + 2hka^*b^*U_{12}]$ .

Table 4. Bond lengths [ $\text{\AA}$ ] for C6 H16 Br4 N2 Pb1 at 293 K with estimated standard deviations in parentheses.

Label	Distances
Pb(1)-Br(1)#0	3.1325(15)
Pb(1)-Br(2)	2.8637(15)
Pb(1)-Br(3)	3.0725(19)
Pb(1)-Br(3)#0	2.9984(17)
Pb(1)-Br(4)	2.978(2)
Pb(1)-Br(4)#0	3.1477(18)
Br(1)-N(2)	3.339(13)
Br(1)-N(2)#0	3.328(13)
Br(2)-N(1)#0	3.399(15)
Br(3)-N(1)#0	3.458(11)
Br(3)-N(2)#0	3.529(12)
Br(3)-N(2)#0	3.694(12)
Br(4)-N(1)	3.478(12)
Br(4)-N(2)	3.466(12)
N(1)-C(3)	1.48(2)
N(1)-C(6)	1.491(17)
N(1)-H(1n1)	0.87
N(1)-H(2n1)	0.87
N(2)-C(1)	1.496(18)
N(2)-H(1n2)	0.87
N(2)-H(2n2)	0.87

---

N(2)-H(3n2)	0.87
C(1)-C(2)	1.490(19)
C(1)-H(1c1)	0.96
C(1)-H(2c1)	0.96
C(2)-C(4)	1.56(2)
C(2)-C(5)#0	1.570(18)
C(2)-H(1c2)	0.96
C(3)-C(5)	1.50(2)
C(3)-H(1c3)	0.96
C(3)-H(2c3)	0.96
C(4)-C(6)#0	1.48(2)
C(4)-H(1c4)	0.96
C(4)-H(2c4)	0.96
C(5)-H(1c5)	0.96
C(5)-H(2c5)	0.96
C(6)-H(1c6)	0.96
C(6)-H(2c6)	0.96

---

Table 5. Bond angles [°] for C6 H16 Br4 N2 Pb1 at 293 K with estimated standard deviations in parentheses.

---

Label	Angles
Br(1)#0-Pb(1)-Br(2)	173.80(4)
Br(1)#0-Pb(1)-Br(3)	88.58(5)
Br(1)#0-Pb(1)-Br(3)#0	82.41(5)
Br(1)#0-Pb(1)-Br(4)	91.38(6)
Br(1)#0-Pb(1)-Br(4)#0	98.37(4)
Br(2)-Pb(1)-Br(3)	86.99(6)
Br(2)-Pb(1)-Br(3)#0	92.64(5)
Br(2)-Pb(1)-Br(4)	92.29(6)
Br(2)-Pb(1)-Br(4)#0	86.93(5)
Br(3)-Pb(1)-Br(3)#0	81.47(5)
Br(3)-Pb(1)-Br(4)	170.78(5)
Br(3)-Pb(1)-Br(4)#0	104.30(6)
Br(3)#0-Pb(1)-Br(4)	89.38(5)
Br(3)#0-Pb(1)-Br(4)#0	174.17(6)
Br(4)-Pb(1)-Br(4)#0	84.82(5)

---

Pb(1)#0-Br(1)-N(2)	88.9(2)
Pb(1)#0-Br(1)-N(2)#0	83.9(2)
N(2)-Br(1)-N(2)#0	95.3(3)
Pb(1)-Br(2)-N(1)#0	90.0(2)
Pb(1)-Br(3)-Pb(1)#0	160.52(7)
Pb(1)-Br(3)-N(1)#0	85.6(2)
Pb(1)-Br(3)-N(2)#0	101.2(2)
Pb(1)-Br(3)-N(2)#0	83.6(2)
Pb(1)#0-Br(3)-N(1)#0	110.6(2)
Pb(1)#0-Br(3)-N(2)#0	87.6(2)
Pb(1)#0-Br(3)-N(2)#0	79.7(2)
N(1)#0-Br(3)-N(2)#0	97.7(3)
N(1)#0-Br(3)-N(2)#0	169.1(3)
N(2)#0-Br(3)-N(2)#0	86.0(3)
Pb(1)-Br(4)-Pb(1)#0	146.23(7)
Pb(1)-Br(4)-N(1)	101.3(2)
Pb(1)-Br(4)-N(2)	83.8(2)
Pb(1)#0-Br(4)-N(1)	100.8(2)
Pb(1)#0-Br(4)-N(2)	117.5(2)
N(1)-Br(4)-N(2)	98.5(3)
Br(2)#0-N(1)-Br(3)#0	73.2(3)
Br(2)#0-N(1)-Br(4)	121.5(3)
Br(2)#0-N(1)-C(3)	119.1(9)
Br(2)#0-N(1)-C(6)	95.3(10)
Br(2)#0-N(1)-H(1n1)	14.49
Br(2)#0-N(1)-H(2n1)	111.48
Br(3)#0-N(1)-Br(4)	81.9(2)
Br(3)#0-N(1)-C(3)	94.8(8)
Br(3)#0-N(1)-C(6)	154.0(9)
Br(3)#0-N(1)-H(1n1)	61.57
Br(3)#0-N(1)-H(2n1)	56.84
Br(4)-N(1)-C(3)	114.9(9)
Br(4)-N(1)-C(6)	84.8(8)
Br(4)-N(1)-H(1n1)	123.91
Br(4)-N(1)-H(2n1)	25.4
C(3)-N(1)-C(6)	111.1(12)

---

C(3)-N(1)-H(1n1)	109.47
C(3)-N(1)-H(2n1)	109.47
C(6)-N(1)-H(1n1)	109.47
C(6)-N(1)-H(2n1)	109.47
H(1n1)-N(1)-H(2n1)	107.78
Br(1)-N(2)-Br(1)#0	103.2(3)
Br(1)-N(2)-Br(3)#0	72.0(2)
Br(1)-N(2)-Br(3)#0	75.9(3)
Br(1)-N(2)-Br(4)	144.2(4)
Br(1)-N(2)-C(1)	115.8(8)
Br(1)-N(2)-H(1n2)	103.53
Br(1)-N(2)-H(2n2)	108.87
Br(1)-N(2)-H(3n2)	7.09
Br(1)#0-N(2)-Br(3)#0	136.1(4)
Br(1)#0-N(2)-Br(3)#0	70.0(2)
Br(1)#0-N(2)-Br(4)	80.1(3)
Br(1)#0-N(2)-C(1)	110.4(8)
Br(1)#0-N(2)-H(1n2)	114.42
Br(1)#0-N(2)-H(2n2)	6.46
Br(1)#0-N(2)-H(3n2)	103.42
Br(3)#0-N(2)-Br(3)#0	66.5(2)
Br(3)#0-N(2)-Br(4)	81.1(2)
Br(3)#0-N(2)-C(1)	110.6(8)
Br(3)#0-N(2)-H(1n2)	34.85
Br(3)#0-N(2)-H(2n2)	134.09
Br(3)#0-N(2)-H(3n2)	76.86
Br(3)#0-N(2)-Br(4)	71.8(2)
Br(3)#0-N(2)-C(1)	167.1(8)
Br(3)#0-N(2)-H(1n2)	60.55
Br(3)#0-N(2)-H(2n2)	69.39
Br(3)#0-N(2)-H(3n2)	82.46
Br(4)-N(2)-C(1)	95.4(7)
Br(4)-N(2)-H(1n2)	46.26
Br(4)-N(2)-H(2n2)	73.75
Br(4)-N(2)-H(3n2)	151.22
C(1)-N(2)-H(1n2)	109.47

---

C(1)-N(2)-H(2n2)	109.47
C(1)-N(2)-H(3n2)	109.47
H(1n2)-N(2)-H(2n2)	109.47
H(1n2)-N(2)-H(3n2)	109.47
H(2n2)-N(2)-H(3n2)	109.47
N(2)-C(1)-C(2)	112.5(12)
N(2)-C(1)-H(1c1)	109.47
N(2)-C(1)-H(2c1)	109.47
C(2)-C(1)-H(1c1)	109.47
C(2)-C(1)-H(2c1)	109.47
H(1c1)-C(1)-H(2c1)	106.29
C(1)-C(2)-C(4)	109.4(13)
C(1)-C(2)-C(5)#0	112.4(12)
C(1)-C(2)-H(1c2)	106.71
C(4)-C(2)-C(5)#0	106.7(12)
C(4)-C(2)-H(1c2)	112.42
C(5)#0-C(2)-H(1c2)	109.41
N(1)-C(3)-C(5)	110.1(14)
N(1)-C(3)-H(1c3)	109.47
N(1)-C(3)-H(2c3)	109.47
C(5)-C(3)-H(1c3)	109.47
C(5)-C(3)-H(2c3)	109.47
H(1c3)-C(3)-H(2c3)	108.82
C(2)-C(4)-C(6)#0	111.2(13)
C(2)-C(4)-H(1c4)	109.47
C(2)-C(4)-H(2c4)	109.47
C(6)#0-C(4)-H(1c4)	109.47
C(6)#0-C(4)-H(2c4)	109.47
H(1c4)-C(4)-H(2c4)	107.73
C(2)#0-C(5)-C(3)	109.9(12)
C(2)#0-C(5)-H(1c5)	109.47
C(2)#0-C(5)-H(2c5)	109.47
C(3)-C(5)-H(1c5)	109.47
C(3)-C(5)-H(2c5)	109.47
H(1c5)-C(5)-H(2c5)	109.07
N(1)-C(6)-C(4)#0	111.2(11)

---

N(1)-C(6)-H(1c6)	109.47
N(1)-C(6)-H(2c6)	109.47
C(4)#0-C(6)-H(1c6)	109.47
C(4)#0-C(6)-H(2c6)	109.47
H(1c6)-C(6)-H(2c6)	107.69

---

---

## Hybrid Organic-Inorganic Halide Post-Perovskite 3-Cyanopyridinium Lead Tribromide for Optoelectronic Applications

*Nikita I. Selivanov, Anna Yu. Samsonova, Ruslan Kevorkyants, Irina V. Krauklis, Yuri V. Chizhov, Boris V. Stroganov, Marios E. Triantafyllou-Rundell, Detlef W. Bahnemann\*, Constantinos C. Stoumpos, Alexei V. Emeline, Yury V. Kapitonov*

Dr. N.I. Selivanov, A.Yu. Samsonova, Dr. R. Kevorkyants, Dr. I.V. Krauklis, Prof. Dr. Yu.V. Chizhov, B.V. Stroganov, Prof. Dr. D.W. Bahnemann, Prof. Dr. A.V. Emeline, Dr. Yu.V. Kapitonov  
Saint Petersburg State University, 7/9 Universitetskaya Emb., St. Petersburg 199034, Russia

M.E. Triantafyllou-Rundell, Assoc. Prof. C.C. Stoumpos  
Department of Materials Science and Technology, Voutes Campus, University of Crete, Heraklion 70013, Greece

Prof. Dr. D.W. Bahnemann  
Institut fuer Technische Chemie, Gottfried Wilhelm Leibniz Universitaet Hannover, Callinstrasse 3, D-30167 Hannover, Germany  
E-mail: bahnemann@iftc.uni-hannover.de

Keywords: post-perovskites, halide perovskites, single crystals, semiconductors, quantum wells

2D halide perovskite-like semiconductors are attractive materials for various optoelectronic applications, from photovoltaics to lasing. To date, the most studied families of such low-dimensional halide perovskite-like compounds are Ruddlesden–Popper, Dion-Jacobson and other phases that can be derived from 3D halide perovskites by slicing along different crystallographic directions, which leads to the spatially isotropic corner-sharing connectivity type of metal-halide octahedra in the 2D layer plane. In this work a new family of hybrid organic-inorganic 2D lead-halides is introduced, by reporting the first example of the hybrid organic-inorganic post-perovskite 3-cyanopyridinium lead tribromide (3cp)PbBr<sub>3</sub>. Post-perovskite structure has unique octahedra connectivity type in the layer plane: typical “perovskite-like” corner-sharing in

---

one direction, and the rare edge-sharing connectivity pattern in the other. Such connectivity leads to a significant anisotropy in the material properties within the inorganic layer plane. Moreover, the dense organic cations packing results in the formation of 1D fully-organic bands in the electronic structure, offering prospects of the involvement of the organic subsystem into material's optoelectronic properties. The (3cp)PbBr<sub>3</sub> clearly shows the 2D quantum size effect with a band gap around 3.2 eV and typical broadband self-trapped excitonic photoluminescence at temperature below 200 K.

## 1. Introduction

Halide perovskites, known and studied<sup>[1-3]</sup> for more than a century, attracted attention in the mid-2010s due to the possibility of their use for the absorber layer in solar cells.<sup>[4]</sup> In parallel with the record achievements in the efficiency of perovskite solar cells,<sup>[5]</sup> the possibilities of using these unique semiconductors in other fields of optoelectronics, such as photodetectors,<sup>[6]</sup> light-emitting diodes,<sup>[7]</sup> lasers active media,<sup>[8]</sup>  $\gamma$ - and X-ray detectors,<sup>[9]</sup> to name a few, are opening up. The structural formula of halide perovskite crystals is ABX<sub>3</sub>, where B<sup>2+</sup> is a metal cation (usually Pb<sup>2+</sup> or Sn<sup>2+</sup>), X<sup>-</sup> is a halide anion (I<sup>-</sup>, Br<sup>-</sup>, Cl<sup>-</sup>), and A<sup>+</sup> is either an inorganic or organic cation in fully inorganic and hybrid organic-inorganic halide perovskites respectively. The main building blocks of the 3D perovskite inorganic frameworks are the [BX<sub>6/2</sub>] octahedra, connected in corner-sharing manner along the three orthogonal spatial dimensions. Such infinite frameworks are only stable when the A-cations have suitable sizes limited by the Goldschmidt relation<sup>[10]</sup> for ionic solids.

Violation of this limitation could lead to edge- or face-sharing octahedra connectivity or leave some of X<sup>-</sup> anions as terminal ligands. This structural versatility results in a huge



---

variety of perovskite-like structures of  $ABX_3$  or dimensionally-reduced stoichiometries. Some B-X framework types could be obtained in fully-inorganic perovskite-like compounds,<sup>[11,12]</sup> but the greatest variety can be achieved via the organic A-cations substitution. Low-dimensional perovskite-like structures are of particular practical interest, among which quasi-2D crystals got the most attention.<sup>[13,14]</sup> The 2D perovskite-like semiconductors are natural multiple quantum wells with well-pronounced quantum size effect, increased exciton binding energy and oscillator strength<sup>[15,16]</sup> and are praised for their stability<sup>[17]</sup> and possibility to be used in various optoelectronic applications, ranging from photovoltaics<sup>[18]</sup> to lasers.<sup>[19]</sup>

The broadest order of hybrid organic-inorganic quasi-2D perovskite-like structures<sup>[20]</sup> could be imagined by slicing off layers from  $ABX_3$  perovskites framework along the (100), (110) or (111) directions with organic cations serving as spacers. The (100)-oriented cleaves lead to the mostly studied Ruddlesden–Popper (RP) and Dion-Jacobson (DJ) families.<sup>[13]</sup> **Figure 1a,c** shows inorganic layers of these two homologous families for  $n=1$ . Therein, the corner-sharing octahedra connectivity in the layer plane inherited from the 3D-perovskite ancestor results in the material isotropy in  $x$  and  $y$  directions. Despite the tremendous possibilities of controlling the crystal structure by selecting the organic cations, not all the possible analogous structures found in oxide perovskite derivatives have been realized in their halide counterparts.

One of the most unexpected oxide perovskite-like crystal structures comes from geophysics. Seismic observation of the Earth's interior led to the discovery of unexpected features of the lowermost mantle region called D'' layer. Most of the lower mantle is composed of  $MgSiO_3$  perovskite. It was expected that in D'' layer this mineral undergoes

---

phase transition, and new phase would explain abnormal properties of this layer. In 2004 this question was resolved by the discovery of  $\text{MgSiO}_3$  polytype<sup>[21,22]</sup> named “post-perovskite”.  $\text{MgSiO}_3$  post-perovskite exists at pressures above 125 GPa and a temperature of 2500 K. This phase consists of  $[\text{SiO}_{6/2}]^{2-}$  octahedra, forming layers with corner- and edge-sharing connectivity in orthogonal directions across the layers’ plane separated by  $\text{Mg}^{2+}$  cations between the layers. This connectivity is schematically shown in Figure 1b. The post-perovskite structure is quite uncommon and it only known in the  $\text{MgGeO}_3$ ,<sup>[23]</sup>  $\text{MnGeO}_3$ ,<sup>[24]</sup>  $\text{CaIrO}_3$ ,<sup>[25]</sup>  $\text{CaRuO}_3$ ,<sup>[26]</sup>  $\text{CaPtO}_3$ <sup>[27]</sup> among oxides. Other material families that host the post-perovskite structure include the  $\text{NaMgF}_3$ <sup>[28]</sup> fluoride, and the  $\beta\text{-LnLuSe}_3$  ( $\text{Ln} = \text{Pr}, \text{Nd}$ )<sup>[29]</sup> and  $\text{UFeE}_3$  ( $\text{E} = \text{S}, \text{Se}$ )<sup>[30]</sup> chalcogenides. The structure of  $\text{Cr}_3\text{GeC}$  is an example of the anti-post-perovskite structure in carbide chemistry.<sup>[31]</sup> The only known heavy halide post-perovskite is fully inorganic  $\text{TlPbI}_3$ .<sup>[11,32]</sup> Despite its toxicity, this material already attracted attention for possible ionizing radiation detection.<sup>[33]</sup> It should be noted that in all the post-perovskites mentioned above the crystal structures adopts the based-centered orthorhombic *Cmcm* space group containing two layers of corrugated octahedra sheets within the unit cell as shown in Figure 1d. This structure could be represented as a high-symmetry structure (Figure 1b) with the lattice constant doubling along the *y* direction due to the octahedra tilts. For hybrid organic-inorganic lead halides only 1D chains with post-perovskite connectivity type were synthesized so far.<sup>[34]</sup>

In this work we introduce a new family of hybrid organic-inorganic 2D lead-halides by reporting the first example of the hybrid organic-inorganic post-perovskite  $(3\text{cp})\text{PbBr}_3$ , where 3cp stands for the 3-cyanopyridinium,  $[\text{3-CN-C}_5\text{H}_5\text{NH}]^+$  cation. We

experimentally explore its structural, optical and vibrational properties, and predict its electronic structure peculiarities by theoretical calculations. The different octahedra connectivities across the inorganic framework layers give rise to the material anisotropy, while the dense organic cations packing offers prospects of the involvement of the organic subsystem into material's optoelectronic properties.

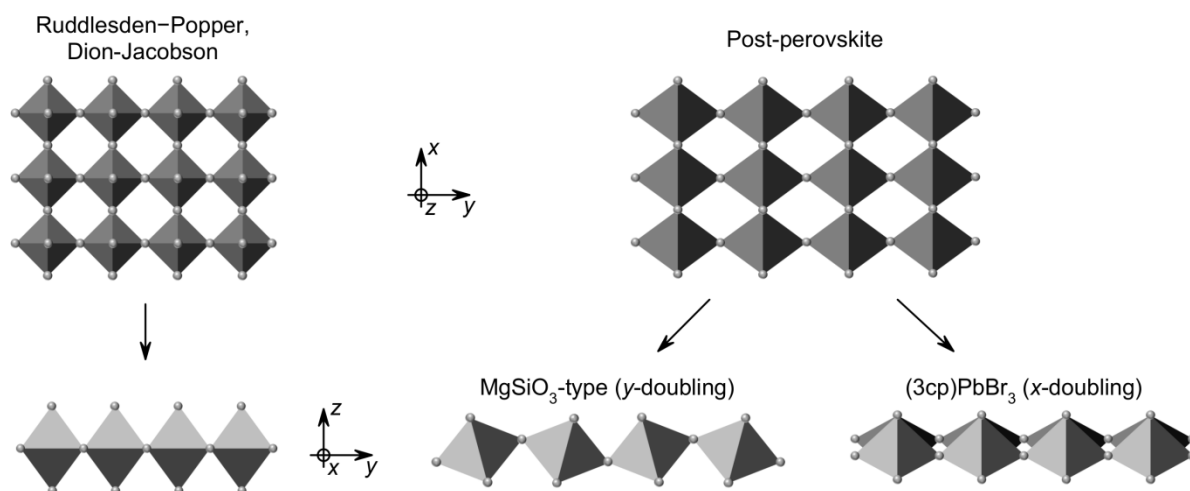


**Figure 1.** Schematic crystal structures of connected  $[BX_6]$  octahedra frameworks for Ruddlesden–Popper and Dion-Jacobson phases (left), and for post-perovskite phase (right) viewed along the stacking  $z$ -axis (top row) and in-plane  $x$ -axis (bottom row). Symmetry lowering in actual post-perovskite structures by doubling the lattice constant along the  $y$ -axis in  $MgSiO_3$ -type and  $x$ -axis in  $(3cp)PbBr_3$  crystal types are shown.

## 2. Results and Discussion

### 2.1. Crystal Growth and Characterization

Centimeter-sized  $(3cp)PbBr_3$  single crystals were grown by the slow counterdiffusion of individual solutions of  $PbBr_2$  and 3-cyanopyridine in  $HBr$  in the silica gel filled U-tube.

This gel growth method has proved applicable for a synthesis of low-dimensional organic-inorganic lead halides<sup>[35]</sup> and 3D perovskites  $MAPbX_3$  ( $X = I, Br$ )<sup>[36]</sup> of high crystal and optical quality. The as-grown  $(3cp)PbBr_3$  crystal plates are optically

translucent and have well-defined rectangular morphology (**Figure 2a**). **The crystals are quite stable and retained their properties after 20 month of storage in a dry atmosphere.**

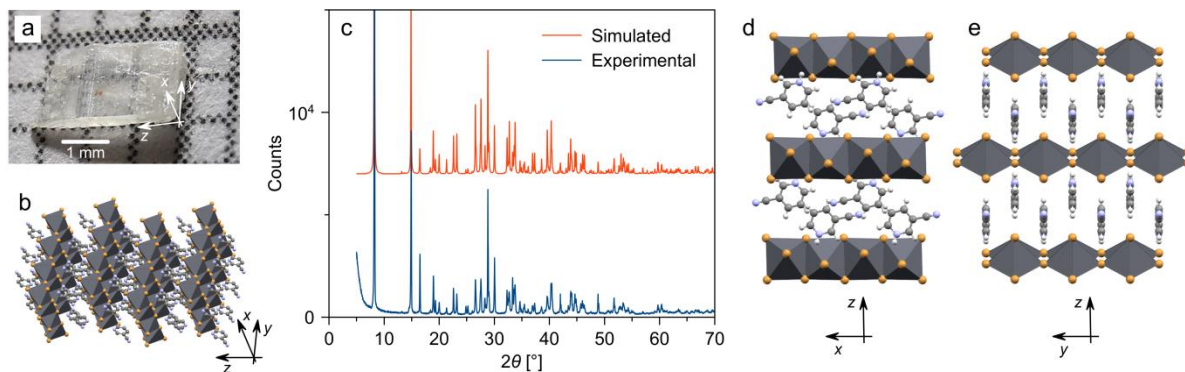


**Figure 2.** The photo (a) and the structure (b) of (3cp)PbBr<sub>3</sub> crystal. [PbBr<sub>6</sub>] octahedrons are shown in gray. Hydrogen atoms are omitted for clarity. (c) XRD patterns for powdered crystal (blue) and simulated patterns based on the single crystal XRD data (red). (d) Crystal structure seen along y (d) and x (e) axes. Atom colors: Pb – grey, Br – orange, C – light gray, N – light blue, H – white.

## 2.2. Crystal Structure

Single crystal XRD study of (3cp)PbBr<sub>3</sub> at 300 K revealed its post-perovskite-type structure (Figure 2b, **Figure S1b**, **Table S2**) with *C2/m* monoclinic space group with (*x,y,z*) axes of Figure 1 roughly corresponding to (*c,b,a*) lattice vectors. The single-phase formation during the synthesis was confirmed by powder XRD analysis of the grinded single crystals (Figure 2c). Note that unlike MgSiO<sub>3</sub>-type post-perovskites (Figure 1d), the crystal structure of (3cp)PbBr<sub>3</sub> exhibits the lattice constant doubling along the *x*-axis, caused by the distortion of the [BX<sub>6</sub>] octahedra in addition to the regular distortion of the structure type (Figure 1e). This distortion is responsible for the lowering of the symmetry from orthorhombic *Cmcm* (parent) to the monoclinic *C2/m* (child) space group. Unlike RP and DJ structures (Figure 1a), the distribution of octahedra in (3cp)PbBr<sub>3</sub> is not

---

uniform in the (*x,y*) plane, arranging in “ridges” of edge-shared anions and “grooves” of corner-shared ones along *x*-axis (Figure 2d). Such anisotropy results in perfect ordering of 3-cyanopyridinium cations along *x*-axis in the “grooves” with the pyridinium nitrogen atoms anchored inside the grooves (Figure 2e). The formation of “ribs” in “grooves” is caused by deformation of the [BX<sub>6</sub>] octahedra, confining the placement of the organic cations along *x*-axis. This leads to the doubling of the lattice constant along the *x*-axis. In this configuration, the Pb<sup>2+</sup> cations are shifted from the octahedra centers (**Figure S5**). The crystal packing of the 3-cyanopyridinium cations in (3cp)PbBr<sub>3</sub> crystal allows for short interatomic distances between pyridinium nitrogen atom and bromides (distances are shown in **Figure 5e,f**). The shortest N···Br distance equal to 3.28 Å allows us to make an assumption about the presence of a hydrogen bond between the corresponding hydrogen and bromine atoms (**Figure 5f**).<sup>[37]</sup> These bonds together with the π-π stacking interactions discussed below likely serve as the stabilizing forces for the orientation and mutual arrangement of 3-cyanopyridinium cations in the organic layer.

Refinement of the XRD data at 100 K (Table S2) reveals a lower-symmetry unit cell for (3cp)PbBr<sub>3</sub>, crystallizing in the triclinic *P*-1 space group (Figure S1a). The phases can be transformed into one another via a phase transition, occurring between 300 and 100 K.

To determine the orientation of the as-grown single crystals, electron backscatter diffraction (EBSD) and powder XRD of single crystals were used. **Figure 3a** shows the EBSD pattern obtained for the crystal. This pattern could be perfectly fit using the known crystal structure (Figure 3b) with the orientation depicted for the crystal in Figure 2a. Surprisingly, the direction of the inorganic framework planes is orthogonal to crystal plate. This indicates a slower crystal growth along the *x*-axis, i.e. the edge-sharing

direction. An additional confirmation of the chosen orientation is the observation of (002) and (004) reflections in the XRD scan of the single crystal in the orientation shown in **Figure S6**. (3cp)PbBr<sub>3</sub> single crystals have cleavage planes along (xz) and (xy) planes (**Figure S7**), indicating the ease of breaking corner-sharing bonds and weak bond between alternating organic and inorganic layers, respectively. Absence of cleavage along the (yz) plane could be explained by the bond strength of edge-sharing octahedra connectivity. Figure 3c shows the X-ray photoelectron spectrum (XPS) of the (3cp)PbBr<sub>3</sub> single crystal. Br3d and Pb4f signals (**Figure S8**) confirm the expected oxidation states of bromide and lead atoms in the compound.

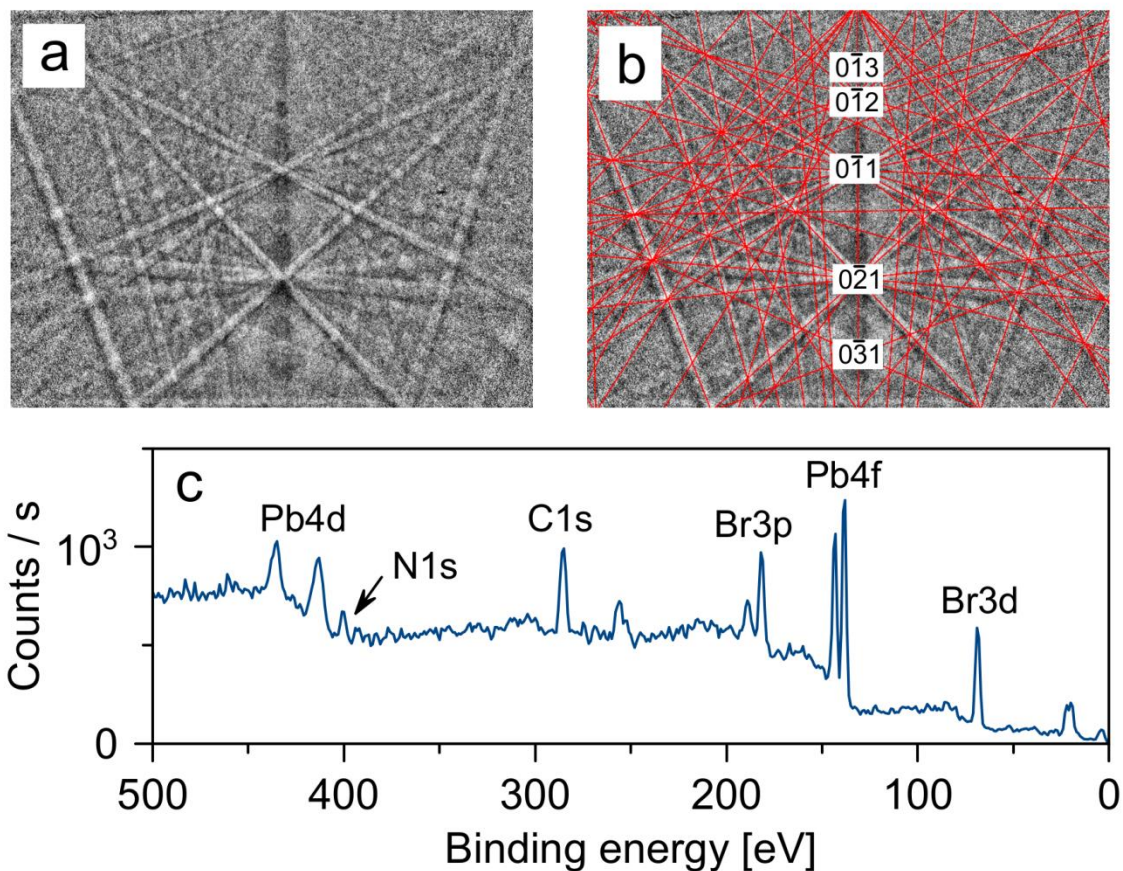


**Figure 3.** (a) EBSD pattern of (3cp)PbBr<sub>3</sub> single crystal and (b) its solution using known crystal structure. (c) XPS spectra of (3cp)PbBr<sub>3</sub> with peaks attribution.

### 2.3. Electronic Structure

Density functional theory (DFT) modeling of (3cp)PbBr<sub>3</sub> was performed with the crystal structure obtained at 300 K with spin-orbit coupling effects included. Calculated electronic band structure and density of states (DOS) are shown in **Figure 4**.

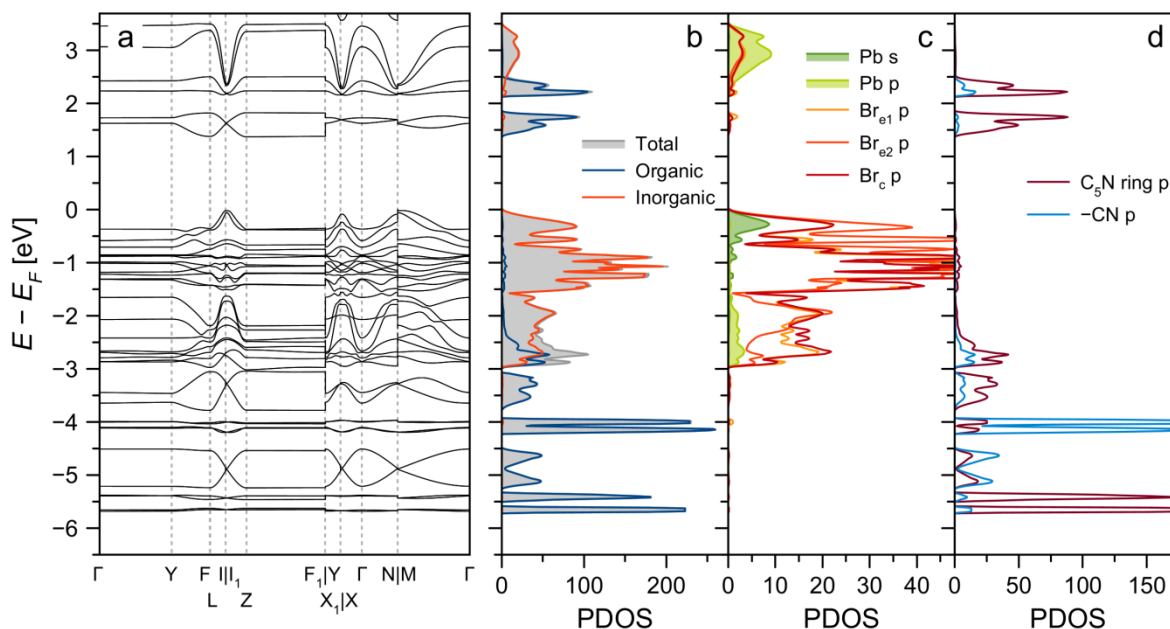


**Figure 4.** Calculated electronic structure of (3cp)PbBr<sub>3</sub>: band structure (a), total density of states (DOS) and organic/inorganic subsystems contribution (b), and DOS of inorganic (c) and organic (d) subsystems.

As can be seen from Figure 4c, the compounds valence band consists of *p*-orbitals of Br and *s*-orbitals of Pb, which is typical of lead-halides.<sup>[38]</sup> The unoccupied inorganic bands consisting of *p*-orbitals of Pb and Br are observed at > 2.4 eV. Additionally, two organic-related bands are observed between the abovementioned inorganic bands. Appearance of similar organic-related bands were already reported for pyridinium and 3-hydroxypyridinium cations in lead trihalides.<sup>[39]</sup> However, the reported bands were flat, which indicated the localization of electron density predominantly on the organic cations

---

weakly interacting with each other and with an inorganic subsystem. In our case, the tight packing of cyanopyridinium cations, their zig-zag stacking orientation within the interlayer space, an increase in the size of their molecular  $\pi$ -orbitals due to the  $-\text{C}\equiv\text{N}$  group, led to the onset of the weak bonding interaction between cations, and the formation of the dispersive bands, observed in the calculations. In attempt to deconvolute these bands, we performed calculations starting with single 3-cyanopyridinium cations. The 3-cyanopyridinium cation is isoelectronic to 3-cyanopyridine because it is formed by the addition of a proton. To better understand the electronic structure, 3-cyanopyridine can be roughly represented as a combination of pyridine and  $-\text{CN}$  group from hydrogen cyanide. **Figure S9** shows the  $\pi$ -molecular orbitals and the corresponding eigenenergies for 3-cyanopyridine  $3\text{-CN-C}_5\text{H}_4\text{N}$ , and its constituent analogues (benzene  $\text{C}_6\text{H}_6$ , pyridine  $\text{C}_5\text{H}_5\text{N}$  and hydrogen cyanide  $\text{HCN}$ ) calculated by DFT method  $\text{wB97X/6-311G(d,p)}$ . Full set of calculated parameters for highest molecular orbitals could be found in **Table S10**.

In the benzene molecule the lowest unoccupied molecular orbitals (LUMO) are degenerate  $\pi_4^*$  and  $\pi_5^*$  antibonding  $\pi$ -molecular orbitals. In the isoelectronic pyridine, this degeneracy is removed due to the symmetry breaking of the ring upon substitution of one of the carbon atoms with a nitrogen atom leading to the splitting of the corresponding molecular orbitals.

On the other hand, the LUMO of hydrogen cyanide consist of degenerate  $\pi_3^*$  and  $\pi_4^*$  antibonding  $\pi$ -molecular orbitals. With this combination, only the  $-\text{CN}$  group  $\pi$ -orbital orthogonal to the pyridine ring plane can interact with the pyridine  $\pi$ -system. This leads to the formation of two unoccupied  $\pi$ -conjugated molecular orbitals  $\pi_5^*$  and  $\pi_6^*$  due to the



---

bonding interaction of  $\pi_4^*$  and  $\pi_5^*$  orbitals of pyridine with  $\pi_4^*$  of  $-\text{CN}$  group. The  $\pi_5^*$  and  $\pi_6^*$  orbitals of 3-cyanopyridine are further split for 0.457 eV. Similar lineage could be drawn up for occupied  $\pi$ -conjugated 3-cyanopyridine orbitals  $\pi_1$ ,  $\pi_2$ ,  $\pi_3$  and  $\pi_4$ .

Next, we consider intermolecular interactions of the 3-cyanopyridinium dimer (Figure S9) with cations orientation and interatomic distances obtained from the room temperature crystal structure. Although this calculation does not capture the electronic properties of the crystal and ignores the crystal field potential, it allows for a qualitative assessment of the intermolecular interactions. The mutual orientation of the cations and the small distance between them favors the stacking interaction between their  $\pi$ -conjugated systems. The shortest distance of 3.265 Å is observed between the nitrogen atom in the  $-\text{CN}$  group of one cation, and the carbon atom in the fourth (counting from nitrogen atom in pyridinium ring) position in the ring of the adjacent cation. Stacking interaction leads to the formation of bonding and antibonding combinations of 3-cyanopyridinium cation  $\pi$ -molecular orbitals with the splitting between their energies being the measure of the interaction strength (Figure 4b).

The maximum splitting of 0.45 eV is for the occupied  $\pi_2 \pm \pi_2$  orbitals interaction (Table S12), and 0.241 and 0.101 eV splitting for  $\pi_5^* \pm \pi_5^*$  and  $\pi_6^* \pm \pi_6^*$  unoccupied orbitals interactions respectively. **Figure 5a-d** shows several molecular orbitals with electron density in the shortest intermolecular distance direction clearly visible. According to calculations, the difference in total energy in the formation of a stacking dimer from 3-cyanopyridinium cations is  $-6.65$  kcal/mol and  $-7.41$  kcal/mol with dispersion interactions taken into account.

This calculation was performed for a dimer, while the transition to an infinite crystal will lead to the formation of bands with electron density delocalized by stacking interactions in  $y$  direction. The shortest distance of 3.515 Å between carbons in fifth position in the rings of cations in adjacent chains prevents the further delocalization in  $x$  direction, so 1D organic bands are formed. Thus, organic bands at 1.4-1.8 eV and 2.1-2.5 eV we identify as delocalized  $\pi_5^* \pm \pi_5^*$  and  $\pi_6^* \pm \pi_6^*$  molecular orbitals of 3-cyanopyridinium cations. Similar bands formed by occupied orbitals are of less interest, since they are located deep in the valence band of (3cp)PbBr<sub>3</sub>.

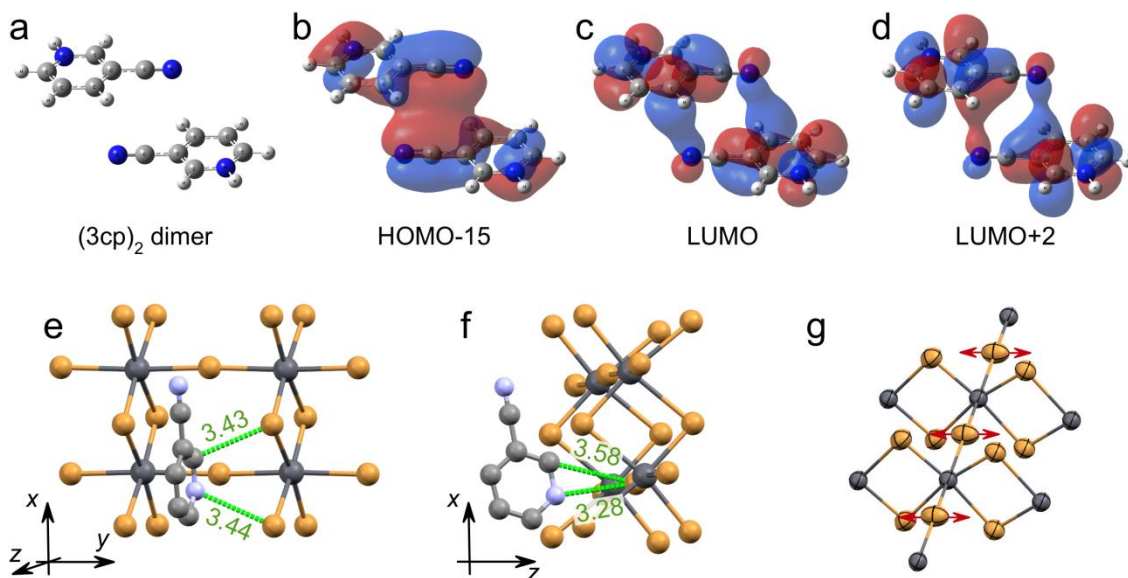


**Figure 5.** (a) Cations dimer arrangement and its molecular orbitals (b,c,d) demonstrating the stacking interaction. (e,f) Fragments of the crystal structure with shortest distances between organic and inorganic atoms shown in Å. Atoms colors: Pb – grey, Br – orange, C – light gray, N – light blue. Hydrogen atoms are omitted for clarity. (g) Thermal ellipsoids for  $T = 300$  K with 90% probability. Red arrows show excessive movement freedom of corner-shared Br atoms.

Presence of weak hydrogen bonds also leads to the insignificant admixture of bands, despite this, which can still be classified as organic and inorganic in origin (Figure 4b).

Little spatial overlap of inorganic and organic bands (for example, based on partial DOS

in Figure 4b) leads to the negligible transition dipole moment between the inorganic states at valence band maximum and unoccupied organic states. Thus, such transitions do not participate in the absorption of light and band gap should be estimated only by consideration of the inorganic bands. In this case the valence band maximum is located in nearly equivalent I, I<sub>1</sub>, N, M-points and the conduction band minimum in X-point and thus leading to the indirect transition with the calculated band gap of 2.27 eV (**Figure S13**). It should be noted that the calculation shows only 0.01 eV higher energy for the minimum at M-point, which leaves the possibility of the direct transition in this material in fact. Since unoccupied organic bands are lying in the band gap, they could act as deep defect states analogous to Bi-doped halide perovskites.<sup>[40,41]</sup>

## 2.4. Optical Spectroscopy

Diffuse reflectance spectra (DRS) of the grinded (3cp)PbBr<sub>3</sub> crystal were used for determination of the absorption edge. **Figure 6a** shows the room-temperature Kubelka-Munk function  $F(R) = (1-R)^2/2R$ , where  $R$  is the measured diffuse reflectance coefficient. The derivative  $dF/dE$  in **Figure S14** shows the maximum at 3.25 eV correlated to the fundamental absorption at the material band edge.

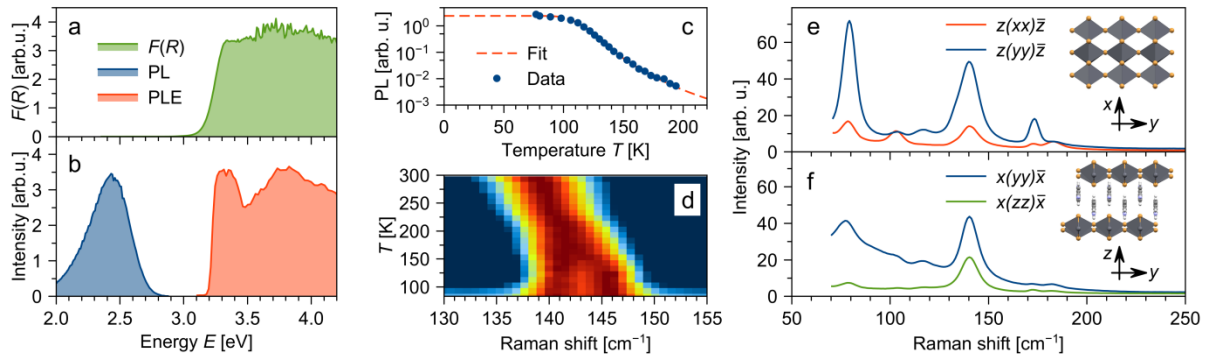


**Figure 6.** (a) Kubelka-Munk function  $F(R)$  at  $T = 300$  K. (b) PL ( $E_{ex} = 3.31$  eV) and PLE ( $E_{em} = 2.45$  eV) spectra at  $T = 77$  K. (c) PL temperature dependence (dots) and Arrhenius

---

fit (dashed line). (d) Normalized unpolarized Raman scattering temperature dependency. (e,f) Polarized Raman scattering at  $T = 300$  K. Insets show crystal orientation. Porto notation is used for polarized scattering geometry.

The photoluminescence (PL) spectrum at  $T = 77$  K with excitation well above the absorption edge ( $E_{ex} = 3.31$  eV) shows a broad emission peak centered at  $E_{em} = 2.45$  eV (Figure 6b). The emission peak's FWHM (full width at half maximum) is 0.36 eV. Such broad emission probably derives from the self-trapped exciton (STE) recombination, a well-known phenomenon in low-dimensional lead halides.<sup>[42]</sup> Photoluminescence excitation (PLE) measurements at  $E_{em}$  show sharp edge at 3.18 eV, which is consistent with the band gap determined by the DRS measurements (Figure 6b). This value is larger than the band gap calculated by DFT (2.34 eV for the direct transition between inorganic bands) due to the well-known tendency of DFT calculations to underestimate the energy band gap.

The studied 2D lead-bromide's band edge is blueshifted by 0.9 eV in comparison with the 3D MAPbBr<sub>3</sub> perovskite band edge.<sup>[43]</sup> This is a manifestation of the quantum-size effect in natural multiple quantum wells (QWs) formed by inorganic framework layers of (3cp)PbBr<sub>3</sub>. This also confirms the fact that despite the slight interaction of organic and inorganic subsystems described above, there are no charge transfer signatures through the organic layer. Thus, we conclude that the organic layer acts as a QW barrier. The red shift of 0.4 eV between the absorption edge and PL emission maximum is a sum of exciton binding energy and STE trapping energy. Absence of the free exciton emission feature (not observed in PL down to  $T = 4$  K) prevents separation of these two contributions. As the temperature rises, PL emission gradually disappears without significant spectral shift or broadening (Figure S15). PLE excitation edge also remains

---

unshifted (Figure S15). The temperature dependency of the PL emission intensity was fitted by the Arrhenius equation  $I = I_0 / (1 + A \cdot \exp(-E_a / k_B T))$ , yielding the activation energy  $E_a$  of the PL quenching processes of 0.14 eV (Figure 6c).

## 2.5. Vibrational Spectroscopy

Different connectivity of octahedra in the inorganic layer of (3cp)PbBr<sub>3</sub> along  $x$  and  $y$  directions should lead to a significant anisotropy of electron-phonon interaction. In order to probe experimentally this anisotropy, polarized Raman spectra were measured at room temperature in different geometries (Figure 6e,f). Observed low-frequency signals (< 200 cm<sup>-1</sup>) correspond to vibrations of the inorganic framework. Figure 5e shows the larger amplitude of the co-polarized Raman signal for vibrations along the octahedra corner-sharing axis ( $y$ -axis) in comparison with vibrations along the edge-sharing axis ( $x$ -axis) for excitation normal to the inorganic layers plane. This effect is the manifestation of the higher amplitude of vibrations of corner-shared Br atoms, which could be also seen in structural data by observation of thermal ellipsoids at 300 K (Figure 5g). Even more pronounced this effect could be seen for the excitation along  $x$ -axis (Figure 6f). A similar effect of an increase in the amplitude and broadening of the Raman signal was observed for three-dimensional halide perovskites in those cases when a motion freedom of the A-cation exists in the crystal lattice.<sup>[44-47]</sup>

Raman spectroscopy was also used to reveal the phase transition between high-temperature  $C2/m$  and low-temperature  $P-1$  phases. The measured temperature dependence of the Raman signal for region around 140 cm<sup>-1</sup> is shown in Figure 6d. At 100 K signal is split in two lines (140 cm<sup>-1</sup> and 146 cm<sup>-1</sup>). With temperature growth

---

these two lines merge at temperature around 200 K, which is a manifestation of the crystal symmetry increase.

### 3. Conclusion

In this work we have introduced the first member of a new family of 2D hybrid organic-inorganic halides, in the form of (3cp)PbBr<sub>3</sub> post-perovskite. The first member of this family – (3cp)PbBr<sub>3</sub>, was synthesized using the innovative gel growth method and characterized both experimentally and theoretically. Optical measurement on single crystals of this material demonstrate a band gap of 3.2 eV and a broadband self-trapped excitonic photoluminescence below 200 K. The material undergoes a structural phase transition around 200 K, reducing its crystal lattice symmetry from monoclinic to triclinic. DFT calculations show that dense packing of organic cations leads to the formation of 1D fully-organic band. However, this band does not directly participate in the optical response. Anisotropy of the post-perovskite structure in the layer plane manifests itself in the anisotropy of electron-phonon coupling pathways, evidenced by the different thermal motion of the corner- (perovskite-like) and edge-shared octahedra. Ongoing work is focused on finding other representatives of this family, studying the possibility of functionalizing the organic A-site cation and the development of routes towards practical application of these materials in optoelectronics, for example as white-light emitters or ionizing radiation detectors.

---

#### 4. Experimental Section

*Reagents:* Lead (II) bromide  $\text{PbBr}_2$  (98%, Sigma-Aldrich), aqueous HBr (40%, Iodobrom), 3-cyanopyridine (98%, Alfa Aesar) were used as received. Silica gel was prepared from sodium metasilicate crystallohydrate solution  $\text{Na}_2\text{SiO}_3 \cdot 9\text{H}_2\text{O}$  with the distilled water as solvent.

*Crystal Growth:* In the present work, a modification of the method used for a synthesis of 1D piperidinium lead triiodide in silicate gel<sup>[38]</sup> was employed. The method is based on a difference in solubility of a target perovskite and lead halide in corresponding hydrohalic acid.

*Crystal Characterization:* Single crystal X-ray diffraction study of the obtained single crystals was carried out using the diffractometer Agilent Technologies Xcalibur (Oxford Diffraction). The apparatus includes an anode – $\text{MoK}\alpha$  X-ray tube, and a detector of reflected X-rays – the high-speed position-sensitive CCD “Atlas”. The structure was solved using charge flipping methods and it was subsequently refined using the Jana2006 software.<sup>[48,49]</sup> XRD measurements were performed at two different temperatures of 100 K and 300 K. Powder X-ray diffraction study was conducted using the Bruker D2 Phaser diffractometer from powdered single crystals and high-resolution X-ray diffractometer Bruker D8 Discover using a long focus X-ray tube  $\text{CuK}\alpha$  anode. Reflected X-rays were detected using a solid position sensitive detector LYNXEYE.

The EBSD measurements were carried out using backscattered electron diffraction detector OxfordHKL NordLys Nano equipped on Hitachi S-3400N scanning electron microscope. Due to structure photodegradation under electron beam EBSD images acquisition was performed as follows: multiple images (50-100) from an area  $40 \times 40 \mu\text{m}$

---

were collected (exposure 50ms per image) and averaged. Pattern indexing was performed using Oxford AzTec software using 300 K crystal structure as a model.

The XPS spectra were collected using Thermo Fisher Scientific ESCALAB 250Xi setup with Al-K $\alpha$  X-ray source (1486.6 eV with monochromator), variable beam size (200-900  $\mu$ m) and energy resolution 0.45 eV.

*Electronic Structure Calculations:*

Electronic structure calculations of (3cp)PbBr<sub>3</sub> were performed within the framework of periodic density functional theory (DFT) using Abinit-8.2.3 program.<sup>[50]</sup> LDA density functional<sup>[51]</sup> was applied. Spin-orbit coupling was accounted for by using relativistic separable Hartwigsen-Goedecker-Hutter pseudopotentials.<sup>[52]</sup> In both the band structure and projected density of states calculations the Brillouin zone was sampled over 4 $\times$ 4 $\times$ 4  $\Gamma$ -centered Monkhorst-Pack grid of k-points.<sup>[53]</sup> The applied kinetic energy cut-off was equal to 60 Hartree. The band structure was computed along the  $\Gamma$ -Y-F-L-I-I1-Z-F1-Y-X1-X- $\Gamma$ -N-M- $\Gamma$  path<sup>[54]</sup> of high symmetry k-points of monoclinic reciprocal lattice.

The DFT-calculations of molecular orbitals were performed with the long-range corrected wB97X/6-311G(d,p) functional, which allows us to accurately estimate the ionization potentials of pyridines. In models of single and dimer organic cations Br<sup>-</sup> anions were added in calculation in order to neutralize the excessive positive charge. In optimization of the geometry, each of the N, Br and C6 atoms of the 3-cyanopyridine cations were fixed. The negligible interaction of anions Br<sup>-</sup> with organic cations allowed us to ignore the bromide orbitals.

*Optical Characterization:*



---

Temperature-dependent photoluminescence and photoluminescence excitation spectra were measured in the 77-300 K range using the Agilent Cary Eclipse spectrofluorometer.

The sample was fixed in a quartz dewar in the cuvette compartment of the spectrofluorometer. Photoluminescence spectra were obtained with 365 nm excitation, and photoluminescence excitation spectra were recorded at 510 nm. The emission slit width was 5 nm, and the excitation slit width was 2.5 nm in both cases.

Powders were prepared by grinding single crystals in an agate mortar. The diffuse reflectance spectra of the powders were obtained using the Cary 5000 UV-Vis-NIR spectrometer equipped with a diffuse reflectance accessory DRA 2500. BaSO<sub>4</sub> powder was used as the reference material.

*Raman Scattering Characterization:*

Raman scattering measurements were carried out in the temperature range 83-300 K using the Horiba LabRam HR 800 spectrometer with the grating of 1800 l/mm and spectral resolution of 2 cm<sup>-1</sup>. A solid-state laser with the wavelength of 532 nm and the power of 10 mW was used as an excitation source. The sample was cooled using the Linkam LNP95 system. An Olympus BX41 microscope with the 10×/0.75NA objective lens was used to focus the laser beam on a sample surface.

[CCDC 2065528-2065529 contains the supplementary crystallographic data for this paper. These data can be obtained free of charge from The Cambridge Crystallographic Data Centre via [www.ccdc.cam.ac.uk/data\\_request/cif](http://www.ccdc.cam.ac.uk/data_request/cif).]

**Supporting Information**

Supporting Information is available from the Wiley Online Library or from the author.

---

## Acknowledgements

This study was supported by the Russian Foundation of Basic Research (Project No. 19-03-00836) and by Saint Petersburg State University via a research Grant ID 73032813. Work at the University of Crete was supported in part by the project “NANO-TANDEM” (MIS 5029191), co-financed by Greece and the European Regional Development Fund and in part by SARF UoC under grant number KA 10652. This work was carried out on the equipment of SPbU Resource centers “Nanophotonics”, “X-Ray Diffraction Studies”, “Computer Center”, “Physical Methods of Surface Investigation” and “Geomodel”.

Received: ((will be filled in by the editorial staff))

Revised: ((will be filled in by the editorial staff))

Published online: ((will be filled in by the editorial staff))

## References

- [1] H. L. Wells, *Am. J. Sci.* **1893**, *3*, 121.
- [2] I. P. Pashuk, N. S. Pidzyrailo, M. G. Matsko, *Sov. Phys. Solid State* **1981**, *23*, 1263.
- [3] D. Frohlich, K. Heidrich, H. Kunzel, G. Trendel, J. Treusch, *J. Lumin.* **1979**, *18/19*, 385.
- [4] A. Kojima, K. Teshima, Y. Shirai, T. Miyasaka, *J. Am. Chem. Soc.* **2009**, *131*, 6050.
- [5] NREL, Best Research-Cell Efficiency Chart, <https://www.nrel.gov/pv/cell-efficiency.html>.
- [6] M. Ahmadi, T. Wu, B. Hu, *Adv. Mater.* **2017**, *29*, 1605242.
- [7] Q. V. Le, H. W. Jang, S. Y. Kim, *Small Methods* **2018**, *2*, 1700419.
- [8] H. Dong, Ch. Zhang, X. Liu, J. Yao, Y. Sh. Zhao, *Chem. Soc. Rev.* **2020**, *49*, 951.
- [9] H. Wei, J. Huang, *Nat. Commun.* **2019**, *10*, 1066.
- [10] V. M. Goldschmidt, *Naturwissenschaften* **1926**, *14*, 477.

- 
- [11] O. Y. Khyzhun, P. M. Fochuk, I. V. Kityk, M. Piasecki, S. I. Levkovets, A. O. Fedorchuk, O. V. Parasyuk, *Mater. Chem. Phys.* **2016**, *172*, 165.
- [12] C. K. Møller, *Nature* **1958**, *182*, 1436.
- [13] L. Mao, C. C. Stoumpos, M. G. Kanatzidis, *J. Am. Chem. Soc.* **2019**, *141*, 1171.
- [14] M. D. Smith, B. A. Connor, H. I. Karunadasa, *Chem. Rev.* **2019**, *119*, 3104.
- [15] J.-C. Blancon, A. V. Stier, H. Tsai, W. Nie, C. C. Stoumpos, B. Traoré, L. Pedesseau, M. Kepenekian, F. Katsutani, G. T. Noe, J. Kono, S. Tretiak, S. A. Crooker, C. Katan, M. G. Kanatzidis, J. J. Crochet, J. Even, A. D. Mohite, *Nat. Commun.* **2018**, *9*, 2254.
- [16] M. Hirasawa, T. Ishihara, T. Goto, *J. Phys. Soc. Jap.* **1994**, *63*, 3870.
- [17] Z. Wang, Q. Lin, F. P. Chmiel, N. Sakai, L. M. Herz, H. J. Snaith, *Nat. Energy* **2017**, *2*, 17135.
- [18] A. Krishna, S. Gottis, M. K. Nazeeruddin, F. Sauvage, *Adv. Funct. Mater.* **2019**, *29*, 1806482.
- [19] E. P. Booker, M. B. Price, P. J. Budden, H. Abolins, Y. del V. - I. Redondo, L. Eyre, I. Nasrallah, R. T. Phillips, R. H. Friend, F. Deschler, N. C. Greenham, *Adv. Opt. Mater.* **2018**, *6*, 1800616.
- [20] E. I. Marchenko, S. A. Fateev, A. A. Petrov, V. V. Korolev, A. Mitrofanov, A. V. Petrov, E. A. Goodilin, A. B. Tarasov, *Chem. Mater.* **2020**, *32*, 7383.
- [21] A. R. Oganov, S. Ono, *Nature* **2004**, *430*, 445.
- [22] M. Murakami, K. Hirose, K. Kawamura, N. Sata, Y. Ohishi, *Science* **2004**, *304*, 855.
- [23] K. Hirose, K. Kawamura, Y. Ohishi, S. Tateno, N. Sata, *Am. Mineral.* **2005**, *90*, 262.
- [24] S. Tateno, K. Hirose, N. Sata, Y. Ohishi, *Phys. Chem. Miner.* **2006**, *32*, 721.
- [25] K. Hirose, Y. Fujita, *Geophys. Res. Lett.* **2005**, *32*.

- 
- [26] H.Kojitani, Y.Shirako, M.Akaogi, *Phys. Earth Planet. Inter.* **2007**, *165*, 127.
- [27] A. Lindsay-Scott, I. G. Wood, D. P. Dobson, L. Vocadlo, J. P. Brodholt, K. S. Knight, M. G. Tucker, T. Taniguchi, *J. Appl. Crystallogr.* **2011**, *44*, 999.
- [28] H. - Z. Liu, J. Chen, J. Hu, C. D. Martin, D. J. Weidner, D. Häusermann, H. - K. Mao, *Geophys. Res. Lett.* **2005**, *32*.
- [29] G. B. Jin, E. S. Choi, R. P. Guertin, J. S. Brooks, C. H. Booth, T. E. Albrecht-Schmitt, *Inorg. Chem.* **2007**, *46*, 9213.
- [30] G. B. Jin, E. Ringe, G. J. Long, F. Grandjean, M. T. Sougrati, E. S. Choi, D. M. Wells, M. Balasubramanian, J. A. Ibers, *Inorg. Chem.* **2010**, *49*, 10455.
- [31] B. Wang, K. Ohgushi, *Sci. Rep.* **2016**, *6*, 37896.
- [32] W. Stoeger, *Z. Naturforsch. B* **2015**, *32*, 975.
- [33] W. Lin, J. He, K. M. McCall, C. C. Stoumpos, Zh. Liu, I. Hadar, S. Das, H. - H. Wang, B.- X. Wang, D. Y. Chung, B. W. Wessels, M. G. Kanatzidis, *Adv. Funct. Mater.* **2021**, 2006635.
- [34] R. Gautier, F. Massuyeau, G. Galon, M. Paris *Adv. Mater.* **2019**, *31*, 1807383.
- [35] R. Kevorkyants, N.I. Selivanov, A.V. Emeline, Crystal and electronic structure of low-dimensional 3-(R)pyridinium lead halide perovskites, R=CH(3-n)Fn (n=0-3), *Journal of Physics and Chemistry of Solids* (under review)
- [36] N.I. Selivanov, A.O. Murzin, V.I. Yudin, Yu.V. Kapitonov, A.V. Emeline, (Preprint) arXiv:2104.03175. submitted: Apr **2021**.
- [37] T. Steiner, *Angew. Chem* **2002**, *41*, 48.
- [38] T. Umebayashi, K. Asai, T. Kondo, A. Nakao, *Phys. Rev. B* **2003**, *67*, 155405.

- 
- [39] N. I. Selivanov, Yu. A. Rozhkova, R. Kevorkyants, A. V. Emeline, D. W. Bahnemann, *Dalton Trans.* **2020**,49, 4390.
- [40] O. A. Lozhkina, A. A. Murashkina, V. V. Shilovskikh, Y. V. Kapitonov, V. K. Ryabchuk, A. V. Emeline, T. Miyasaka, *J. Phys. Chem. Lett.* **2018**, 9, 5408.
- [41] P. K. Nayak, M. Sendner, B. Wenger, Z. Wang, K Sharma, A. J. Ramadan, Robert Lovrinčić, A. Pucci, P. K. Madhu, and H. J. Snaith, *J. Am. Chem. Soc.* **2018**, 140, 574.
- [42] M. D. Smith, A. Jaffe, E. R. Dohner, A. M. Lindenberg, H. I. Karunadasa, *Chem. Sci.* **2017**, 8, 4497.
- [43] O. A. Lozhkina, V. I. Yudin, A. A. Murashkina, V. V. Shilovskikh, V. G. Davydov, R. Kevorkyants, A. V. Emeline, Y. V. Kapitonov, D. W. Bahnemann, *J. Phys. Chem. Lett.* **2018**, 9, 302.
- [44] Y. Guo, O. Yaffe, D. W. Paley, A. N. Beecher, T. D. Hull, G. Szpak, J. S. Owen, L. E. Brus, M. A. Pimenta, *Phys. Rev. Materials* **2017**, 1.
- [45] D. H. Fabini, G. Laurita, J. S. Bechtel, C. C. Stoumpos, H. A. Evans, A. G. Kontos, Y. S. Raptis, P. Falaras, A. Van der Ven, M. G. Kanatzidis, R. Seshadri, *J. Am. Chem. Soc.* **2016**, 138, 11820.
- [46] D. H. Fabini, C. C. Stoumpos, G. Laurita, A. Kaltzoglou, A. G. Kontos, P. Falaras, M. G. Kanatzidis, R. Seshadri, *Angew. Chem.* **2016**, 128, 15618.
- [47] G. Laurita, D. H. Fabini, C. C. Stoumpos, M. G. Kanatzidis, R. Seshadri, *Chem. Sci.* **2017**, 8, 5628.

---

[48] V. Petricek, M. Dusek, L. Palatinus, *Z. Kristallogr.* **2014**, 229, 345.

[49] L. Palatinus, G. Chapuis, *J. Appl. Crystallogr.* **2007**, 40, 786.

[50] X. Gonze, B. Amadon, P. M. Anglade, J. - M. Beuken, F. Bottin, P. Boulanger, F. Bruneval, D. Caliste, R. Caracas, M. Cote, T. Deutsch, L. Genovese, Ph. Ghosez, M. Giantomassi, S. Goedecker, D. Hamann, P. Hermet, F. Jollet, G. Jomard, S. Leroux, M. Mancini, S. Mazevet, M. J. T. Oliveira, G. Onida, Y. Pouillon, T. Rangel, G. - M. Rignanese, D. Sangalli, R. Shaltaf, M. Torrent, M. J. Verstraete, G. Zérah, J. W. Zwanziger, *Comput. Phys. Commun.* **2009**, 180, 2582.

[51] D. M. Ceperley, B. J. Alder, *Phys. Rev. Lett.* **1980**, 45, 566.

[52] C. Hartwigsen, S. Goedecker, J. Hutter, *Phys. Rev. B* **1998**, 58, 3641.

[53] H. J. Monkhorst, J. D. Pack, *Phys. Rev. B* **1976**, 13, 5188.

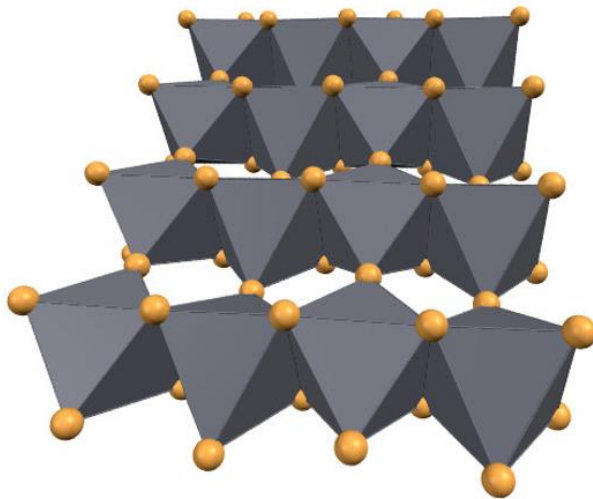
[54] W. Setyawan, S. Curtarolo, *Comput. Mater. Sci.* **2010**, 49, 299.

---

A new family of hybrid organic-inorganic 2D lead-halides is introduced: hybrid organic-inorganic post-perovskites. First member – 3-cyanopyridinium lead tribromide (3cp)PbBr<sub>3</sub> is synthesized and studied. 2D quantum size effect is observed with the band gap around 3.2 eV and broadband self-trapped excitonic photoluminescence at temperature below 200 K. Material in-plane anisotropy is revealed by the Raman scattering. Tight organic cations packing leads to the formation of the 1D band.

N.I. Selivanov, A.Yu. Samsonova, R. Kevorkyants, I.V. Krauklis, Yu.V. Chizhov, B.V. Stroganov, M.E. Triantafyllou-Rundell, D.W. Bahnemann\*, C.C. Stoumpos, A.V. Emeline, Yu.V. Kapitonov

**Hybrid Organic-Inorganic Halide Post-Perovskite 3-Cyanopyridinium Lead Tribromide for Optoelectronic Applications**



halide post-perovskite

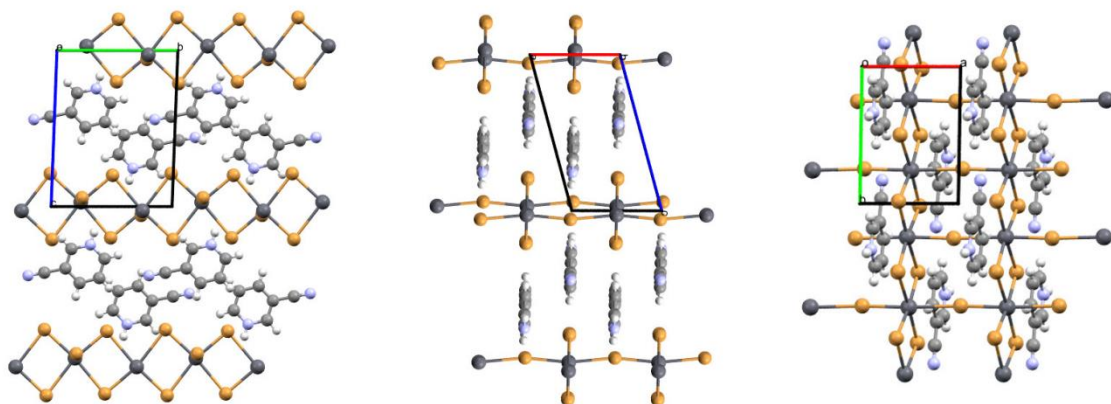
---

## Supporting Information

### Hybrid Organic-Inorganic Halide Post-Perovskite 3-Cyanopyridinium Lead Tribromide for Optoelectronic Applications

*Nikita I. Selivanov, Anna Yu. Samsonova, Ruslan Kevorkyants, Irina V. Krauklis, Yuri V. Chizhov, Boris V. Stroganov, Marios E. Triantafyllou-Rundell, Detlef W. Bahnemann\*, Constantinos C. Stoumpos, Alexei V. Emeline, Yury V. Kapitonov*

a  $T = 100$  K



b  $T = 300$  K

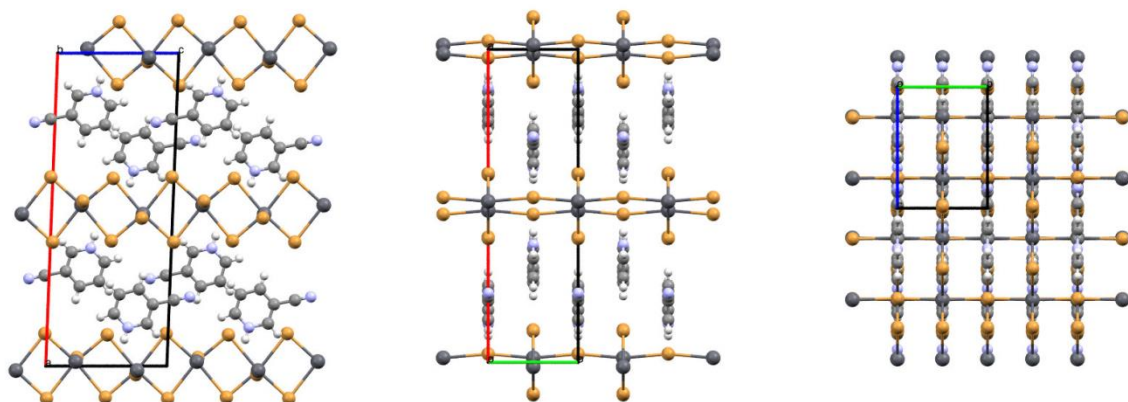


**Figure S1.** Crystal structure of (3cp)PbBr<sub>3</sub> single crystals at  $T = 100$  K (a) and  $T = 300$  K (b).

**Table S2.** Crystal data and structure refinement for (3cp)PbBr<sub>3</sub> (C<sub>6</sub>H<sub>5</sub>Br<sub>3</sub>N<sub>2</sub>Pb).



Temperature	99.9 K	296.7 K
Structure parameters	Tables S3.1-S3.4	Tables S4.1-S4.4
Empirical formula	C6 H5 Br3 N2 Pb1	
Formula weight	552	
Wavelength	0.71073 Å	
Crystal system	triclinic	monoclinic
Space group	P -1	C 1 2 / m 1
a, Å	6.1425(3)	21.5052(9)
b, Å	8.2612(3)	6.1867(4)
c, Å	11.0368(7)	8.3273(3)
$\alpha$ , °	91.963(4)	90
$\beta$ , °	105.053(5)	92.184(3)
$\gamma$ , °	90.396(4)	90
Volume, Å <sup>3</sup>	540.45(5)	1107.11(9)
Z	2	4
Density (calculated)	3.3922 g/cm <sup>3</sup>	3.3119 g/cm <sup>3</sup>
Absorption coefficient	26.649 mm <sup>-1</sup>	26.018 mm <sup>-1</sup>
F(000)	484	968
Crystal size	0.1 x 0.08 x 0.03 mm <sup>3</sup>	
$\theta$ range for data collection	3.07 to 29.12°	3.04 to 29.14°
Index ranges	-8<=h<=8, -10<=k<=11, -14<=l<=14	-22<=h<=29, -8<=k<=7, -11<=l<=11
Reflections collected	8012	4756
Independent reflections	2554 [R <sub>int</sub> = 0.0406]	1432 [R <sub>int</sub> = 0.0216]
Completeness	to $\theta$ = 27.41° 98%	to $\theta$ = 27.62° 98%
Refinement method	Full-matrix least-squares on F <sup>2</sup>	
Data / restraints / parameters	2554 / 0 / 110	1432 / 0 / 73
Goodness-of-fit	1.89	1.62
Final R indices [ $I > 2\sigma(I)$ ]	R <sub>obs</sub> = 0.0524, wR <sub>obs</sub> = 0.1037	R <sub>obs</sub> = 0.0219, wR <sub>obs</sub> = 0.0585
R indices [all data]	R <sub>all</sub> = 0.0573, wR <sub>all</sub> = 0.1053	R <sub>all</sub> = 0.0249, wR <sub>all</sub> = 0.0591
Extinction coefficient	?	?
Largest diff. peak and hole	8.37 and -3.89 e·Å <sup>-3</sup>	0.55 and -1.16 e·Å <sup>-3</sup>

$$R = \frac{\sum ||F_o| - |F_c||}{\sum |F_o|}, wR = \left\{ \frac{\sum [w(|F_o|^2 - |F_c|^2)^2]}{\sum [w(|F_o|^4)]} \right\}^{1/2} \text{ and } w = 1/(\sigma^2(I) + 0.0004I^2)$$

**Table S3.1.** Atomic coordinates ( $\times 10^4$ ) and equivalent isotropic displacement parameters ( $\text{\AA}^2 \times 10^3$ ) for C6 H5 Br3 N2 Pb1 at **99.9 K** with estimated standard deviations in parentheses.

Label	x	y	z	Occupancy	$U_{\text{eq}}^*$
Pb(1)	5141(1)	7564(1)	280(1)	1	13(1)
Br(1)	6027(2)	5015(2)	2004(1)	1	15(1)
Br(2)	6077(2)	10172(2)	2112(1)	1	16(1)
Br(3)	409(2)	7466(2)	562(2)	1	19(1)
C(1)	1990(20)	1372(14)	3966(10)	1	17(4)
N(1)	2221(19)	-1698(12)	4426(9)	1	23(4)
N(2)	1190(17)	3362(11)	2456(8)	1	17(3)
C(2)	2460(20)	2587(13)	4899(10)	1	15(4)
C(3)	2280(20)	4188(13)	4581(10)	1	16(4)
C(4)	1360(20)	1798(13)	2719(10)	1	16(4)
C(5)	1652(18)	4571(13)	3346(10)	1	13(4)
C(6)	2160(20)	-356(14)	4239(10)	1	18(4)
H(1c2)	2911.99	2312.38	5766.42	1	18.3
H(1c3)	2604.41	5031.81	5225.49	1	19.4
H(1c4)	1048.89	977.9	2056.17	1	19.4
H(1c5)	1536.79	5682.27	3113.04	1	15.2
H(1n2)	760.59	3617.99	1671.99	1	20.4

\* $U_{\text{eq}}$  is defined as one third of the trace of the orthogonalized  $U_{ij}$  tensor.

**Table S3.2.** Anisotropic displacement parameters ( $\text{\AA}^2 \times 10^3$ ) for C6 H5 Br3 N2 Pb1 at **99.9 K** with estimated standard deviations in parentheses.

Label	$U_{11}$	$U_{22}$	$U_{33}$	$U_{12}$	$U_{13}$	$U_{23}$
Pb(1)	21(1)	8(1)	10(1)	-1(1)	2(1)	0(1)
Br(1)	23(1)	10(1)	10(1)	0(1)	2(1)	0(1)
Br(2)	24(1)	10(1)	11(1)	-2(1)	2(1)	-2(1)
Br(3)	22(1)	22(1)	12(1)	0(1)	4(1)	0(1)
C(1)	20(7)	18(6)	14(6)	0(5)	2(5)	2(5)
N(1)	33(7)	14(5)	23(6)	1(5)	5(5)	2(4)
N(2)	24(6)	15(5)	11(5)	1(4)	3(4)	0(4)
C(2)	17(7)	16(6)	11(5)	-3(5)	2(5)	4(4)

C(3)	12(7)	16(6)	18(6)	-1(5)	1(5)	-7(5)
C(4)	14(7)	16(6)	20(6)	-7(5)	6(5)	-4(5)
C(5)	8(6)	15(6)	16(6)	-3(5)	5(4)	5(4)
C(6)	22(7)	21(7)	9(5)	-2(5)	3(5)	-6(5)

The anisotropic displacement factor exponent takes the form:  $-2\pi^2[h^2a^*U_{11} + \dots + 2hka^*b^*U_{12}]$ .

**Table S3.3.** Bond lengths [Å] for C6 H5 Br3 N2 Pb1 at **99.9 K** with estimated standard deviations in parentheses.

Label	Distances
Pb(1)-Br(1)	2.8462(11)
Pb(1)-Br(1)#1	3.1757(11)
Pb(1)-Br(2)	2.8536(11)
Pb(1)-Br(2)#2	3.2191(12)
Pb(1)-Br(3)	3.0030(15)
Pb(1)-Br(3)#3	3.1715(14)
Br(1)-N(2)	3.420(11)
Br(1)-N(2)#3	3.385(10)
Br(2)-N(1)#4	3.855(10)
Br(3)-N(2)#5	3.265(9)
C(1)-C(2)	1.386(15)
C(1)-C(4)	1.388(16)
C(1)-C(6)	1.468(16)
N(1)-C(6)	1.133(16)
N(2)-C(4)	1.334(14)
N(2)-C(5)	1.351(14)
N(2)-H(1n2)	0.87
C(2)-C(3)	1.378(15)
C(2)-H(1c2)	0.96
C(3)-C(5)	1.366(15)
C(3)-H(1c3)	0.96
C(4)-H(1c4)	0.96
C(5)-H(1c5)	0.96

Symmetry transformations used to generate equivalent atoms:

---

(1) -x+1,-y+1,-z (2) -x+1,-y+2,-z (3) x+1,y,z (4) -x+1,-y+1,-z+1 (5) -x,-y+1,-z (6) x-1,y,z

**Table S3.4.** Bond angles [°] for C6 H5 Br3 N2 Pb1 at **99.9 K** with estimated standard deviations in parentheses.

---

Label	Angles
Br(1)-Pb(1)-Br(1)#1	90.23(3)
Br(1)-Pb(1)-Br(2)	96.66(3)
Br(1)-Pb(1)-Br(2)#2	167.82(3)
Br(1)-Pb(1)-Br(3)	86.26(4)
Br(1)-Pb(1)-Br(3)#3	83.93(4)
Br(1)#1-Pb(1)-Br(2)	173.11(3)
Br(1)#1-Pb(1)-Br(2)#2	77.59(3)
Br(1)#1-Pb(1)-Br(3)	92.41(3)
Br(1)#1-Pb(1)-Br(3)#3	93.95(3)
Br(2)-Pb(1)-Br(2)#2	95.52(3)
Br(2)-Pb(1)-Br(3)	88.06(4)
Br(2)-Pb(1)-Br(3)#3	86.80(3)
Br(2)#2-Pb(1)-Br(3)	94.28(3)
Br(2)#2-Pb(1)-Br(3)#3	96.65(3)
Br(3)-Pb(1)-Br(3)#3	168.32(3)
Pb(1)-Br(1)-Pb(1)#1	89.77(3)
Pb(1)-Br(1)-N(2)	112.28(15)
Pb(1)-Br(1)-N(2)#3	115.10(17)
Pb(1)#1-Br(1)-N(2)	80.46(15)
Pb(1)#1-Br(1)-N(2)#3	81.94(15)
N(2)-Br(1)-N(2)#3	129.0(2)
Pb(1)-Br(2)-Pb(1)#2	84.48(3)
Pb(1)-Br(2)-N(1)#4	150.07(15)
Pb(1)#2-Br(2)-N(1)#4	125.44(15)
Pb(1)#6-Br(3)-Pb(1)	168.32(4)
Pb(1)#6-Br(3)-N(2)#5	82.96(19)
Pb(1)-Br(3)-N(2)#5	86.63(19)

---

C(2)-C(1)-C(4)	119.0(10)
C(2)-C(1)-C(6)	122.8(10)
C(4)-C(1)-C(6)	118.2(10)
Br(2)#4-N(1)-C(6)	83.2(7)
Br(1)#6-N(2)-Br(1)	129.0(3)
Br(1)#6-N(2)-Br(3)#5	84.3(2)
Br(1)#6-N(2)-C(4)	117.1(8)
Br(1)#6-N(2)-C(5)	79.8(6)
Br(1)#6-N(2)-H(1n2)	73.01
Br(1)-N(2)-Br(3)#5	87.9(3)
Br(1)-N(2)-C(4)	113.5(8)
Br(1)-N(2)-C(5)	78.2(7)
Br(1)-N(2)-H(1n2)	78.16
Br(3)#5-N(2)-C(4)	92.2(6)
Br(3)#5-N(2)-C(5)	144.5(7)
Br(3)#5-N(2)-H(1n2)	26.14
C(4)-N(2)-C(5)	123.3(9)
C(4)-N(2)-H(1n2)	118.37
C(5)-N(2)-H(1n2)	118.37
C(1)-C(2)-C(3)	119.9(10)
C(1)-C(2)-H(1c2)	120.04
C(3)-C(2)-H(1c2)	120.04
C(2)-C(3)-C(5)	119.8(10)
C(2)-C(3)-H(1c3)	120.12
C(5)-C(3)-H(1c3)	120.12
C(1)-C(4)-N(2)	119.0(10)
C(1)-C(4)-H(1c4)	120.52
N(2)-C(4)-H(1c4)	120.52
N(2)-C(5)-C(3)	119.1(10)
N(2)-C(5)-H(1c5)	120.47
C(3)-C(5)-H(1c5)	120.47
C(1)-C(6)-N(1)	178.0(12)

---

Symmetry transformations used to generate equivalent atoms:

(1)  $-x+1, -y+1, -z$  (2)  $-x+1, -y+2, -z$  (3)  $x+1, y, z$  (4)  $-x+1, -y+1, -z+1$  (5)  $-x, -y+1, -z$  (6)  $x-1, y, z$

**Table S4.1.** Atomic coordinates ( $\times 10^4$ ) and equivalent isotropic displacement parameters ( $\text{\AA}^2 \times 10^3$ ) for C6 H5 Br3 N2 Pb1 at **296.7 K** with estimated standard deviations in parentheses.

Label	x	y	z	Occupancy	$U_{\text{eq}}^*$
Pb(1)	4857(1)	0	2448(1)	1	30(1)
Br(1)	3962(1)	0	-171(1)	1	37(1)
Br(2)	9730(1)	0	2541(1)	1	44(1)
Br(3)	4001(1)	0	4982(1)	1	35(1)
N(1)	7791(4)	0	11671(9)	1	64(3)
N(2)	8766(3)	0	6653(7)	1	39(2)
C(1)	7711(4)	0	5862(10)	1	43(3)
C(2)	7894(4)	0	10369(11)	1	46(3)
C(3)	8324(4)	0	5478(9)	1	38(2)
C(4)	7548(4)	0	7462(9)	1	40(3)
C(5)	8027(4)	0	8640(9)	1	39(2)
C(6)	8641(3)	0	8220(9)	1	36(2)
H(1c1)	7392.37	0	5022.54	1	51.1
H(1c3)	8436.82	0	4373	1	45.9
H(1c4)	7119.23	0	7746.98	1	47.9
H(1c6)	8971.45	0	9029.42	1	43.6
H(1n2)	9153.49	0	6388.33	1	47.1

\* $U_{\text{eq}}$  is defined as one third of the trace of the orthogonalized  $U_{ij}$  tensor.

**Table S4.2.** Anisotropic displacement parameters ( $\text{\AA}^2 \times 10^3$ ) for C6 H5 Br3 N2 Pb1 at **296.7 K** with estimated standard deviations in parentheses.

Label	$U_{11}$	$U_{22}$	$U_{33}$	$U_{12}$	$U_{13}$	$U_{23}$
Pb(1)	29(1)	34(1)	27(1)	0	0(1)	0
Br(1)	34(1)	40(1)	36(1)	0	-5(1)	0
Br(2)	35(1)	36(1)	62(1)	0	-1(1)	0
Br(3)	31(1)	40(1)	36(1)	0	4(1)	0
N(1)	77(6)	71(6)	43(4)	0	7(4)	0
N(2)	33(3)	30(4)	54(4)	0	2(3)	0

C(1)	41(4)	36(5)	50(5)	0	-11(4)	0
C(2)	47(5)	37(5)	54(5)	0	-5(4)	0
C(3)	41(4)	31(4)	43(4)	0	2(3)	0
C(4)	28(4)	32(4)	59(5)	0	-4(3)	0
C(5)	37(4)	30(4)	50(4)	0	-1(3)	0
C(6)	34(4)	20(4)	54(5)	0	-5(3)	0

The anisotropic displacement factor exponent takes the form:  $-2\pi^2[h^2a^{*2}U_{11} + \dots + 2hka^*b^*U_{12}]$ .

**Table S4.3.** Bond lengths [Å] for C6 H5 Br3 N2 Pb1 at **296.7 K** with estimated standard deviations in parentheses.

Label	Distances
Pb(1)-Br(1)	2.8539(8)
Pb(1)-Br(1)#1	3.2277(8)
Pb(1)-Br(2)#2	3.1065(4)
Pb(1)-Br(2)#3	3.1065(4)
Pb(1)-Br(3)	2.8516(8)
Pb(1)-Br(3)#4	3.1949(8)
Br(1)-N(1)#4	3.925(9)
Br(2)-N(2)#5	3.277(6)
Br(3)-N(2)#2	3.437(3)
Br(3)-N(2)#3	3.437(3)
N(1)-C(2)	1.115(12)
N(2)-C(3)	1.337(10)
N(2)-C(6)	1.343(10)
N(2)-H(1n2)	0.87
C(1)-C(3)	1.369(11)
C(1)-C(4)	1.392(11)
C(1)-H(1c1)	0.96
C(2)-C(5)	1.478(12)
C(3)-H(1c3)	0.96
C(4)-C(5)	1.395(11)
C(4)-H(1c4)	0.96
C(5)-C(6)	1.380(11)
C(6)-H(1c6)	0.96

Symmetry transformations used to generate equivalent atoms:  
[126]

(1)  $-x+1, y, -z$  (2)  $x-1/2, y-1/2, z$  (3)  $x-1/2, y+1/2, z$  (4)  $-x+1, y, -z+1$  (5)  $-x+2, y, -z+1$  (6)  $x+1/2, y-1/2, z$  (7)  $x+1/2, y+1/2, z$

**Table S4.4.** Bond angles [°] for C6 H5 Br3 N2 Pb1 at **296.7 K** with estimated standard deviations in parentheses.

Label	Angles
Br(1)-Pb(1)-Br(1)#1	94.25(2)
Br(1)-Pb(1)-Br(2)#2	87.808(15)
Br(1)-Pb(1)-Br(2)#3	87.808(15)
Br(1)-Pb(1)-Br(3)	97.47(2)
Br(1)-Pb(1)-Br(3)#4	172.22(2)
Br(1)#1-Pb(1)-Br(2)#2	94.944(15)
Br(1)#1-Pb(1)-Br(2)#3	94.944(15)
Br(1)#1-Pb(1)-Br(3)	168.28(2)
Br(1)#1-Pb(1)-Br(3)#4	77.964(19)
Br(2)#2-Pb(1)-Br(2)#3	169.45(2)
Br(2)#2-Pb(1)-Br(3)	85.532(15)
Br(2)#2-Pb(1)-Br(3)#4	92.821(15)
Br(2)#3-Pb(1)-Br(3)	85.532(15)
Br(2)#3-Pb(1)-Br(3)#4	92.821(15)
Br(3)-Pb(1)-Br(3)#4	90.31(2)
Pb(1)-Br(1)-Pb(1)#1	85.75(2)
Pb(1)-Br(1)-N(1)#4	148.74(12)
Pb(1)#1-Br(1)-N(1)#4	125.51(12)
Pb(1)#6-Br(2)-Pb(1)#7	169.45(3)
Pb(1)#6-Br(2)-N(2)#5	85.320(16)
Pb(1)#7-Br(2)-N(2)#5	85.320(16)
Pb(1)-Br(3)-Pb(1)#4	89.69(2)
Pb(1)-Br(3)-N(2)#2	114.12(10)
Pb(1)-Br(3)-N(2)#3	114.12(10)
Pb(1)#4-Br(3)-N(2)#2	81.38(10)
Pb(1)#4-Br(3)-N(2)#3	81.38(10)
N(2)#2-Br(3)-N(2)#3	128.30(13)
Br(1)#4-N(1)-C(2)	85.2(6)
Br(2)#5-N(2)-Br(3)#6	85.62(11)



---

Br(2)#5-N(2)-Br(3)#7	85.62(11)
Br(2)#5-N(2)-C(3)	144.8(5)
Br(2)#5-N(2)-C(6)	91.9(4)
Br(2)#5-N(2)-H(1n2)	26.47
Br(3)#6-N(2)-Br(3)#7	128.30(18)
Br(3)#6-N(2)-C(3)	79.35(19)
Br(3)#6-N(2)-C(6)	115.57(10)
Br(3)#6-N(2)-H(1n2)	74.95
Br(3)#7-N(2)-C(3)	79.35(19)
Br(3)#7-N(2)-C(6)	115.57(10)
Br(3)#7-N(2)-H(1n2)	74.95
C(3)-N(2)-C(6)	123.3(7)
C(3)-N(2)-H(1n2)	118.36
C(6)-N(2)-H(1n2)	118.36
C(3)-C(1)-C(4)	120.3(7)
C(3)-C(1)-H(1c1)	119.85
C(4)-C(1)-H(1c1)	119.85
N(1)-C(2)-C(5)	179.6(9)
N(2)-C(3)-C(1)	119.5(7)
N(2)-C(3)-H(1c3)	120.24
C(1)-C(3)-H(1c3)	120.24
C(1)-C(4)-C(5)	117.8(7)
C(1)-C(4)-H(1c4)	121.09
C(5)-C(4)-H(1c4)	121.09
C(2)-C(5)-C(4)	121.4(7)
C(2)-C(5)-C(6)	117.9(7)
C(4)-C(5)-C(6)	120.7(7)
N(2)-C(6)-C(5)	118.3(7)
N(2)-C(6)-H(1c6)	120.83
C(5)-C(6)-H(1c6)	120.83

---

Symmetry transformations used to generate equivalent atoms:

(1)  $-x+1, y, -z$  (2)  $x-1/2, y-1/2, z$  (3)  $x-1/2, y+1/2, z$  (4)  $-x+1, y, -z+1$  (5)  $-x+2, y, -z+1$  (6)  $x+1/2, y-1/2, z$  (7)  $x+1/2, y+1/2, z$

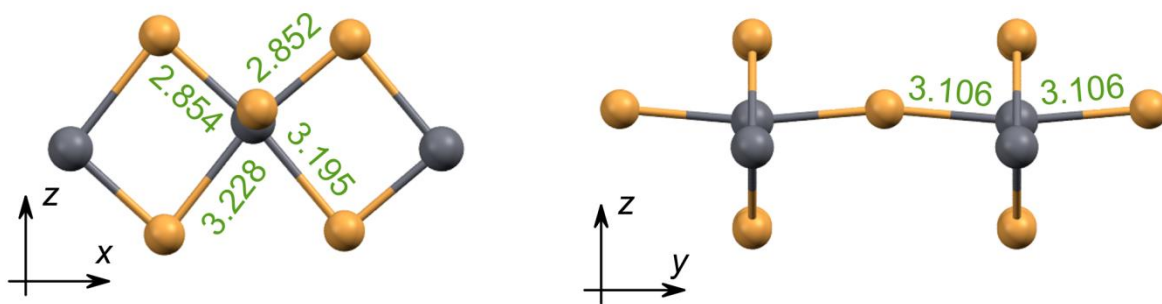


**Figure S5.** Pb-Br distances in  $[\text{PbBr}_6]$  octahedron at  $T = 300$  K.

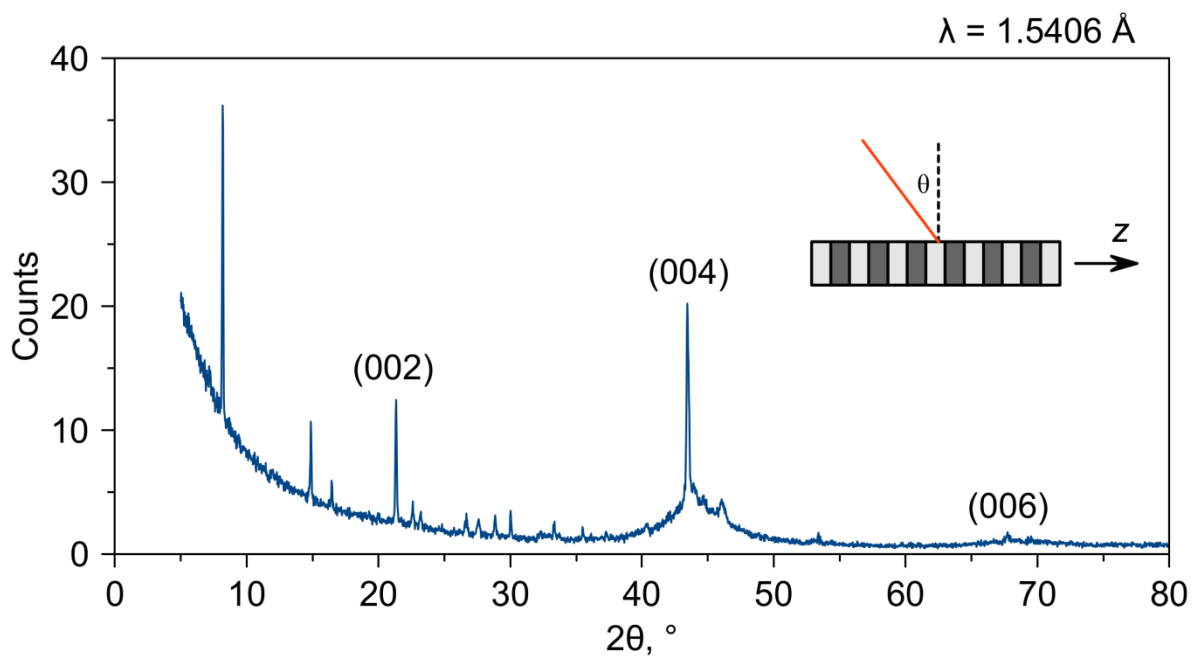


**Figure S6.** Powder XRD scan of the  $(3\text{cp})\text{PbBr}_3$  single crystal. Crystal orientation is shown in the inset.

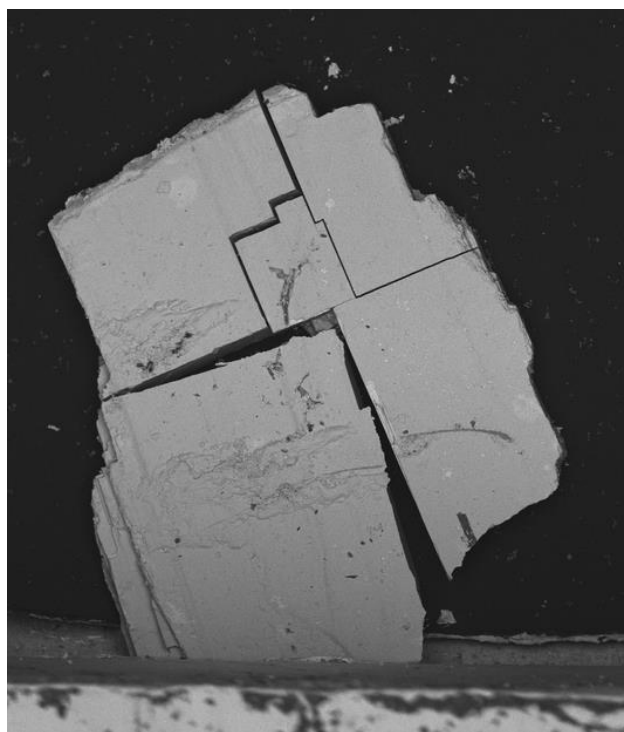


**Figure S7.** Crystal cracks parallel to  $(xy)$  and  $(xz)$  planes after 300 K – 4 K – 300 K thermal cycling. Scanning electron microscopy image, crystal size 2×3 mm.

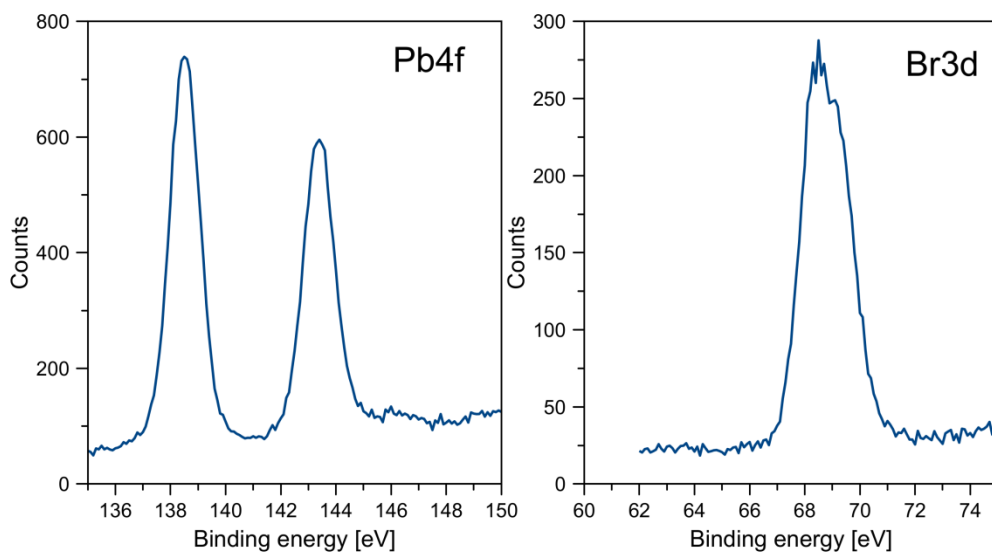


**Figure S8.** XPS spectra of  $(3cp)PbBr_3$  single crystal.

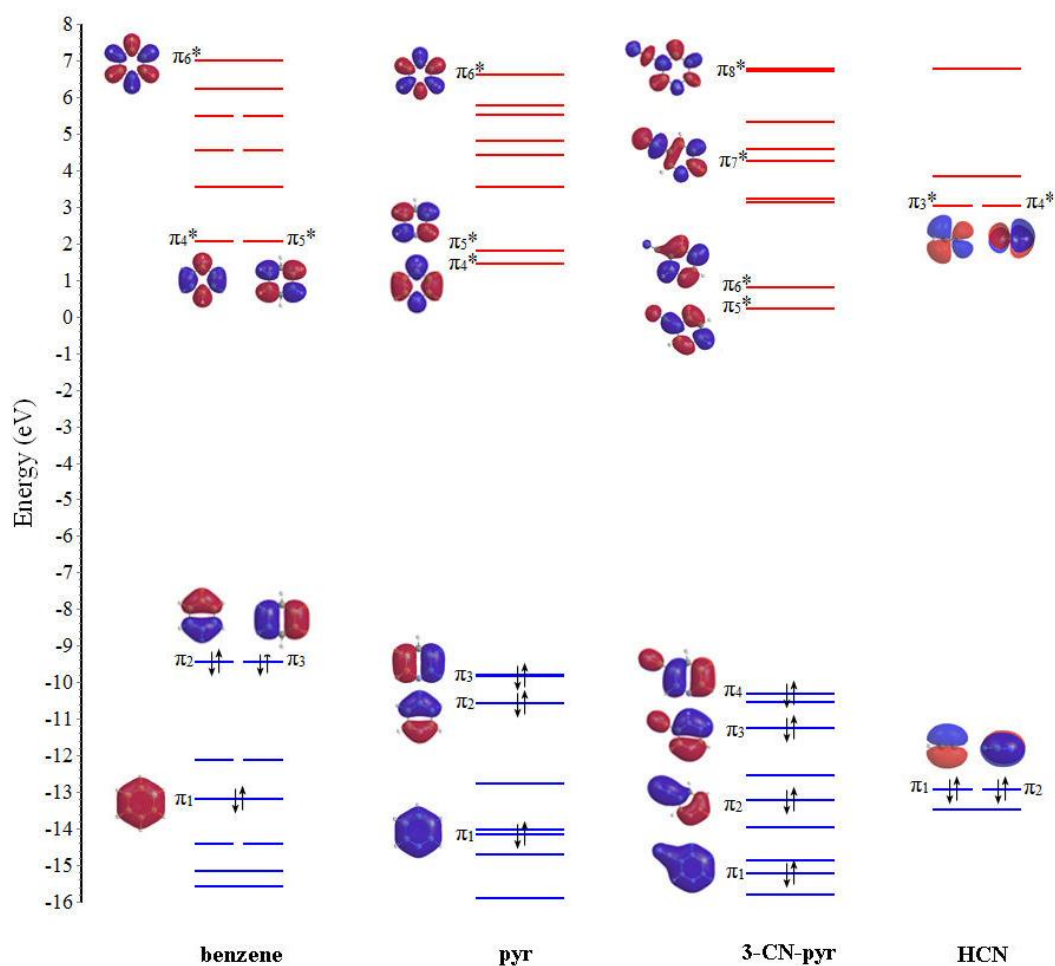


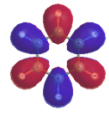
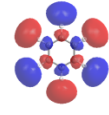
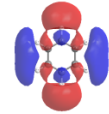
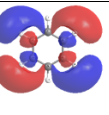
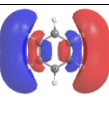
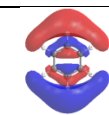
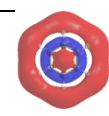
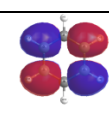
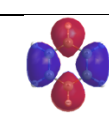
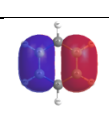
**Figure S9.** Molecular orbitals diagram for benzene ( $C_6H_6$ ), pyridine ( $C_5H_5N$ ), 3-cyanopyridine (3-CN- $C_5H_5N$ ), and hydrogen cyanide (HCN).

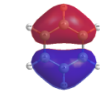
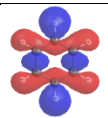
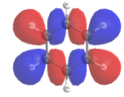
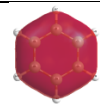
**Table S10.** Molecular orbitals of benzene, pyridine, 3-cyanopyridine, and hydrogen cyanide obtained by the wb97X/6-311G(d,p) method.

**Benzene,  $C_6H_6$**  (symmetry group  $D_{6h}$ )

$E = -232.234197$  a. u.,  $\mu = 0.00$  D

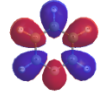
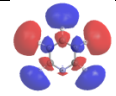
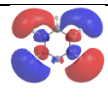
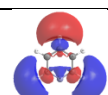
Number	HOMO-LUMO	Irreducible Representation (IR)	$\epsilon$ , eV	Type of MO

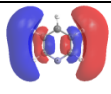
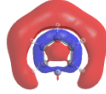
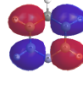
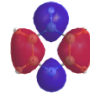
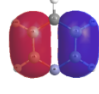
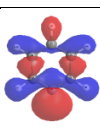
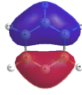
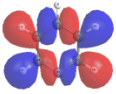
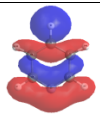
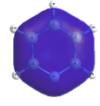
30	LUMO+8	1b <sub>2g</sub>	6.986		$\pi_6^*$ - MO
29	LUMO+7	3b <sub>1u</sub>	6.224		$\sigma_{12}^*$ - MO
28	LUMO+6	8e <sub>2g</sub>	5.488		$\sigma_{11}^*$ - MO
27	LUMO+5	7e <sub>2g</sub>	5.488		$\sigma_{10}^*$ - MO
26	LUMO+4	8e <sub>1u</sub>	4.542		$\sigma_9^*$ - MO
25	LUMO+3	7e <sub>1u</sub>	4.542		$\sigma_8^*$ - MO
24	LUMO+2	4a <sub>1g</sub>	3.549		$\sigma_7^*$ - MO
23	LUMO+1	2e <sub>2u</sub>	2.044		$\pi_5^*$ - MO
22	LUMO	1e <sub>2u</sub>	2.044		$\pi_4^*$ - MO
21	HOMO	2e <sub>1g</sub>	-9.436		$\pi_3$ - MO

20	HOMO-1	$1e_{1g}$	-9.436		$\pi_{2-}$ MO
19	HOMO-2	$6e_{2g}$	-12.114		$\sigma_{6-}$ MO
18	HOMO-3	$5e_{2g}$	-12.114		$\sigma_{5-}$ MO
17	HOMO-4	$1a_{2u}$	-13.190		$\pi_{1-}$ MO

**Pyridine,  $C_5H_5N$**  (symmetry group  $C_{2v}$ )

$E = -248.270521$  a.u.,  $\mu = 2.22$  D

Number	HOMO-LUMO	Irreducible Representation (IR)	$\epsilon$ , eV	Type of MO
29	LUMO+7	$4b_1$	6.611	 $\pi_{6}^{*-}$ MO
28	LUMO+6	$14a_1$	5.776	 $\sigma_{11}^{*-}$ MO
27	LUMO+5	$9b_2$	5.497	 $\sigma_{10}^{*-}$ MO
26	LUMO+4	$13a_1$	4.809	 $\sigma_{9}^{*-}$ MO

25	LUMO+3	8b <sub>2</sub>	4.415		$\sigma_8^*$ - MO
24	LUMO+2	12a <sub>1</sub>	3.552		$\sigma_7^*$ - MO
23	LUMO+1	2a <sub>2</sub>	1.785		$\pi_5^*$ - MO
22	LUMO	3b <sub>1</sub>	1.431		$\pi_4^*$ - MO
21	HOMO	1a <sub>2</sub>	-9.806		$\pi_3$ - MO
20	HOMO-1	11a <sub>1</sub>	-9.816		$\sigma_6$ - MO
19	HOMO-2	2b <sub>1</sub>	- 10.569		$\pi_2$ - MO
18	HOMO-3	7b <sub>2</sub>	- 12.762		$\sigma_5$ - MO
17	HOMO-4	10a <sub>1</sub>	- 14.014		$\sigma_4$ - MO
16	HOMO-5	1b <sub>1</sub>	- 14.147		$\pi_1$ - MO

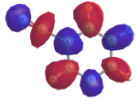
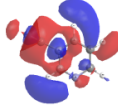
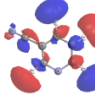
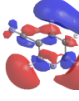
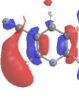
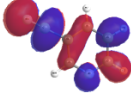
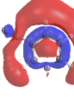
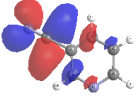
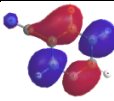
Ionization potentials:

IP(experiment) = 9.85 eV [Alexei N. Pankratov. Quantitative Structure–Property Relationships in the Pyridine Series. // Heteroatom Chemistry, Vol. 13, N. 3, 2002, pp. 229-240.]

IP(our calculation) = 9.81 eV.

**3-CN-Pyridine, 3-CN-C<sub>5</sub>H<sub>4</sub>N** (symmetry group C<sub>s</sub>)

E = -340.508314 a.u.,  $\mu$  = 3.91 D

Number	HOMO-LUMO	Irreducible Representation (IR)	$\epsilon$ , eV	Type of MO	
37	LUMO+9	8 a''	6.363		$\pi_8^*$ -MO
36	LUMO+8	29 a'	6.169		$\sigma_{11}^*$ -MO
35	LUMO+7	28 a'	5.253		$\sigma_{10}^*$ -MO
34	LUMO+6	27 a'	4.518		$\sigma_9^*$ -MO
33	LUMO+5	26 a'	4.130		$\sigma_8^*$ -MO
32	LUMO+4	7 a''	3.977		$\pi_7^*$ -MO
31	LUMO+3	25 a'	3.050		$\sigma_7^*$ -MO
30	LUMO+2	24 a'	2.958		pseudo $\pi^*$ -MO CN-group
					



29	LUMO+1	6 a''	0.702		$\pi_6^*$ -MO
28	LUMO	5 a''	0.245		$\pi_5^*$ -MO
27	HOMO	4a''	-10.317		$\pi_4$ -MO
26	HOMO-1	23a'	-10.555		$\sigma_6$ -MO
25	HOMO-2	3a''	-11.248		$\pi_3$ -MO
24	HOMO-3	22a'	-12.546		pseudo $\pi$ -MO CN-group
23	HOMO-4	21a'	-13.217		$\sigma$ -MO CN-group
22	HOMO-5	2a''	-13.232		$\pi_2$ -MO
21	HOMO-6	20a'	-13.972		$\sigma_5$ -MO
20	HOMO-7	19a'	-14.872		$\sigma_4$ -MO
19	HOMO-8	1a''	-15.215		$\pi_1$ -MO

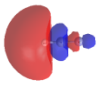
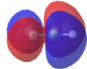
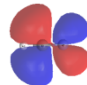
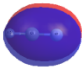
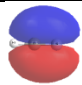
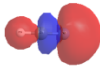
### Ionization potentials:

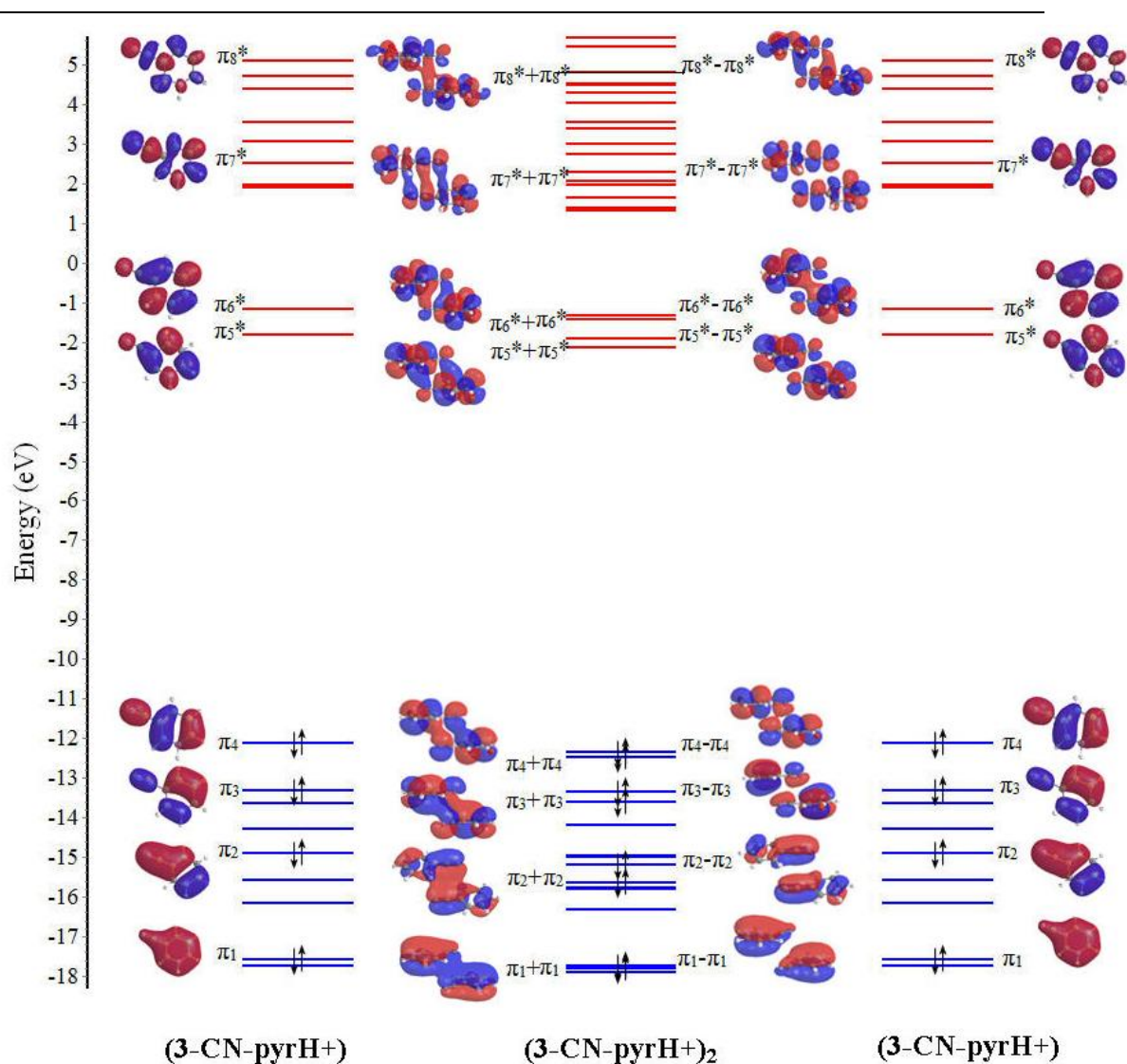
IP (experiment) = 10.10 eV [Alexei N. Pankratov. Quantitative Structure–Property Relationships in the Pyridine Series. // Heteroatom Chemistry, Vol. 13, N. 3, 2002, pp. 229-240.]

IP(our calculation) = 10.32eV.

**Hydrogen cyanide, HCN** (symmetry group  $C_{\infty v}$ )

E = -93.420594 a. u.,  $\mu$  = 3.01 D

Number	HOMO-LUMO	Irreducible Representation (IR)	$\epsilon$ , eV	Type of MO	
10	LUMO+2	$6\sigma$	3.820		$\sigma^*$ - MO
9	LUMO+1	$4\pi$	3.029		$\pi_4^*$ - MO
8	LUMO	$3\pi$	3.029		$\pi_3^*$ - MO
7	HOMO	$2\pi$	- 12.925		$\pi_2$ - MO
6	HOMO-1	$1\pi$	- 12.925		$\pi_1$ - MO
5	HOMO-2	$5\sigma$	- 13.494		$\sigma$ - MO

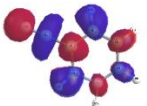
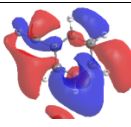
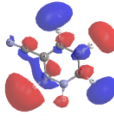
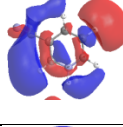
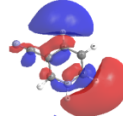
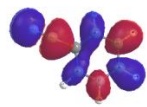
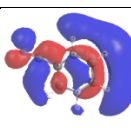
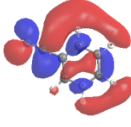
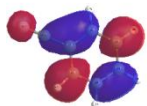


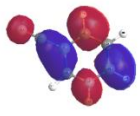
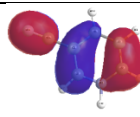
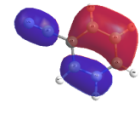
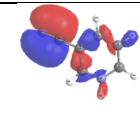
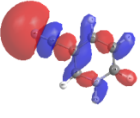
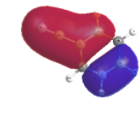
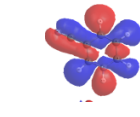
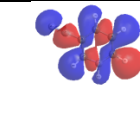
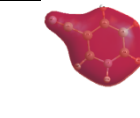
**Figure S11.** Molecular orbitals diagram for two separated 3-cyanopyridinium cations and a dimer.

**Table S12.** Table of the MO energies of 3-cyanopyridine cations 3-CN-C<sub>5</sub>H<sub>4</sub>NH<sup>+</sup> and (3-CN-C<sub>5</sub>H<sub>4</sub>NH<sup>+</sup>)<sub>2</sub> dimer.

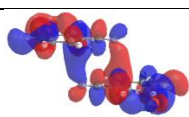
(3-CN-C<sub>5</sub>H<sub>4</sub>NH<sup>+</sup>) (symmetry group C<sub>s</sub>)

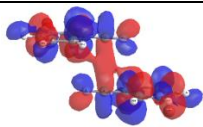
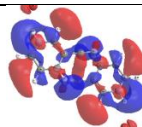
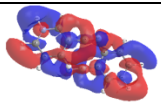
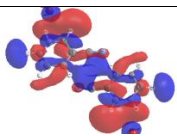
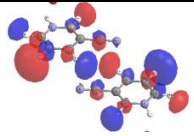
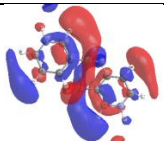
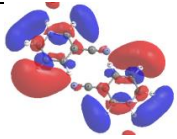
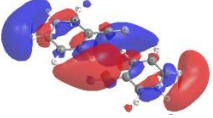
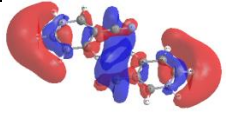
MO	HOMO-LUMO	$\epsilon$ , eV	Type of MO

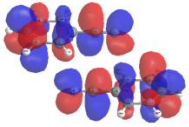
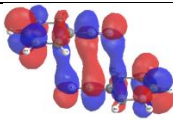
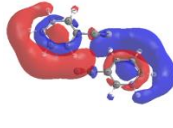
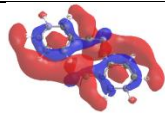
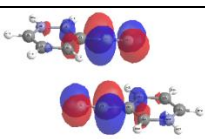
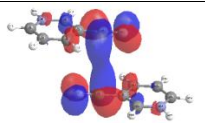
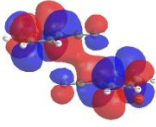
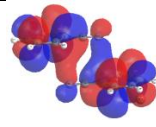
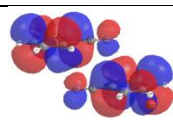
55 a''	LUMO+9	5.096		$\pi_8^*$ -MO 3-CN-pyr
54 a'	LUMO+8	4.720		$\sigma_{11}^*$ -MO 3-CN-pyr
53 a'	LUMO+7	4.400		$\sigma_{10}^*$ -MO 3-CN-pyr
52 a'	LUMO+6	3.560		$\sigma^*$ -MO 3-CN-pyr
51 a'	LUMO+5	3.070		$\sigma_9^*$ -MO 3-CN-pyr
50 a''	LUMO+4	2.526		$\pi_7^*$ -MO 3-CN-pyr
49 a'	LUMO+3	1.955		pseudo $\pi^*$ -MO CN-group + $\sigma_8^*$ -MO 3-CN-pyr
48 a'	LUMO+2	1.884		pseudo $\pi^*$ -MO CN-group + $\sigma_7^*$ -MO 3-CN-pyr
47 a''	LUMO+1	-1.169		$\pi_6^*$ -MO 3-CN-pyr

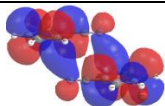
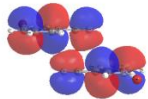
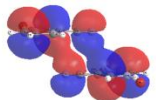


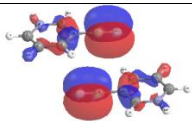
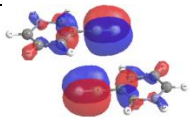
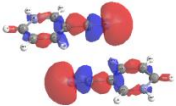
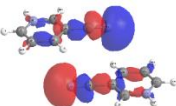
46 a''	LUMO	-1.830		$\pi_5^*$ -MO 3-CN-pyr
42 a''	HOMO-3	-12.124		$\pi_4$ -MO 3-CN-pyr
41 a''	HOMO-4	-13.309		$\pi_3$ -MO 3-CN-pyr
40 a'	HOMO-5	-13.641		pseudo $\pi$ -MO CN-group
39 a'	HOMO-6	-14.297		$\sigma$ -MO CN-group
38 a''	HOMO-7	-14.915		$\pi_2$ -MO 3-CN-pyr
37 a'	HOMO-8	-15.574		$\sigma_6$ -MO 3-CN-pyr
36 a'	HOMO-9	-16.148		$\sigma_5$ -MO 3-CN-pyr
35 a''	HOMO-10	-17.571		$\pi_1$ -MO 3-CN-pyr

**(3-CN-C<sub>5</sub>H<sub>4</sub>NH<sup>+</sup>)<sub>2</sub>** (symmetry group C<sub>i</sub>)

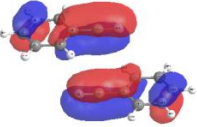
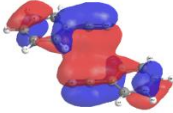
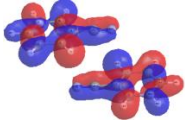
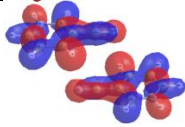
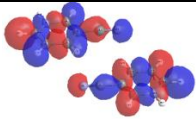
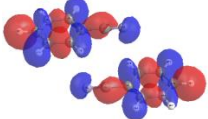
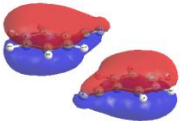
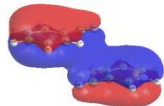
MO	HOMO-LUMO	$\epsilon$ , eV	Type of MO	
110 a <sub>u</sub>	LUMO+19	4.819		( $\pi_8^* - \pi_8^*$ ) MO 3-CN-pyr

109 <sub>ag</sub>	LUMO+18	4.815		( $\pi_8^* + \pi_8^*$ ) MO 3-CN-pyr
108 <sub>ag</sub>	LUMO+17	4.520		( $\sigma_{11}^* - \sigma_{11}^*$ ) MO 3-CN-pyr
107 <sub>au</sub>	LUMO+16	4.495		( $\sigma_{11}^* + \sigma_{11}^*$ ) MO 3-CN-pyr
106 <sub>ag</sub>	LUMO+15	4.290		( $\sigma^* + \sigma^*$ ) MO 3-CN-pyr
105 <sub>au</sub>	LUMO+14	4.032		( $\sigma_{10}^* + \sigma_{10}^*$ ) MO 3-CN-pyr
104 <sub>au</sub>	LUMO+13	3.557		( $\sigma_9^* - \sigma_9^*$ ) MO 3-CN-pyr
103 <sub>ag</sub>	LUMO+12	3.370		( $\sigma_9^* + \sigma_9^*$ ) MO 3-CN-pyr
102 <sub>au</sub>	LUMO+11	2.981		( $\sigma_8^* - \sigma_8^*$ ) MO 3-CN-pyr
101 <sub>ag</sub>	LUMO+10	2.723		( $\sigma_8^* + \sigma_8^*$ ) MO 3-CN-pyr

100 a <sub>u</sub>	LUMO+9	2.285		( $\pi_7^* - \pi_7^*$ ) MO 3-CN-pyr
99a <sub>g</sub>	LUMO+8	2.064		( $\pi_7^* + \pi_7^*$ ) MO 3-CN-pyr
98a <sub>u</sub>	LUMO+7	1.974		( $\sigma_7^* - \sigma_7^*$ ) MO 3-CN-pyr
97a <sub>g</sub>	LUMO+6	1.645		( $\sigma_7^* + \sigma_7^*$ ) MO 3-CN-pyr
96 a <sub>u</sub>	LUMO+5	1.373		(pseudo $\pi^* - \text{pseudo}\pi^*$ ) MOCN-group
95a <sub>g</sub>	LUMO+4	1.318		(pseudo $\pi^* + \text{pseudo}\pi^*$ ) MOCN-group
94 a <sub>g</sub>	LUMO+3	-1.336		( $\pi_6^* - \pi_6^*$ ) MO 3-CN-pyr
93a <sub>u</sub>	LUMO+2	-1.437		( $\pi_6^* + \pi_6^*$ ) MO 3-CN-pyr
92 a <sub>u</sub>	LUMO+1	-1.913		( $\pi_5^* - \pi_5^*$ ) MO 3-CN-pyr

91 <sub>ag</sub>	LUMO	-2.154		( $\pi_5^* + \pi_5^*$ ) MO 3-CN-pyr
84 <sub>ag</sub>	HOMO-6	-12.340		( $\pi_4 - \pi_4$ ) MO 3-CN-pyr
83 <sub>au</sub>	HOMO-7	-12.483		( $\pi_4 + \pi_4$ ) MO 3-CN-pyr
82 <sub>ag</sub>	HOMO-8	-13.345		( $\pi_3 - \pi_3$ ) MO 3-CN-pyr
81 <sub>au</sub>	HOMO-9	-13.597		( $\pi_3 + \pi_3$ ) MO 3-CN-pyr
80 <sub>au</sub>	HOMO-10	-14.184		(pseudo $\pi$ - pseudo $\pi$ ) MO3-CN-pyr
79 <sub>ag</sub>	HOMO-11	-14.193		(pseudo $\pi$ + pseudo $\pi$ ) MOCN-group
78 <sub>ag</sub>	HOMO-12	-14.963		( $\sigma - \sigma$ ) MO CN-group
77 <sub>au</sub>	HOMO-13	-15.008		( $\sigma + \sigma$ ) MO CN-group



76a <sub>u</sub>	HOMO-14	-15.176		( $\pi_2 - \pi_2$ ) MO 3-CN-pyr
75 a <sub>g</sub>	HOMO-15	-15.626		( $\pi_2 + \pi_2$ ) MO 3-CN-pyr
74a <sub>u</sub>	HOMO-16	-15.768		( $\sigma_6 - \sigma_6$ ) MO 3-CN-pyr
73 a <sub>g</sub>	HOMO-17	-15.805		( $\sigma_6 + \sigma_6$ ) MO 3-CN-pyr
72a <sub>u</sub>	HOMO-18	-16.326		( $\sigma_5 - \sigma_5$ ) MO 3-CN-pyr
71 a <sub>g</sub>	HOMO-19	-16.336		( $\sigma_5 + \sigma_5$ ) MO 3-CN-pyr
70a <sub>u</sub>	HOMO-20	-17.739		( $\pi_1 - \pi_1$ ) MO 3-CN-pyr
69 a <sub>g</sub>	HOMO-21	-17.808		( $\pi_1 + \pi_1$ ) MO 3-CN-pyr

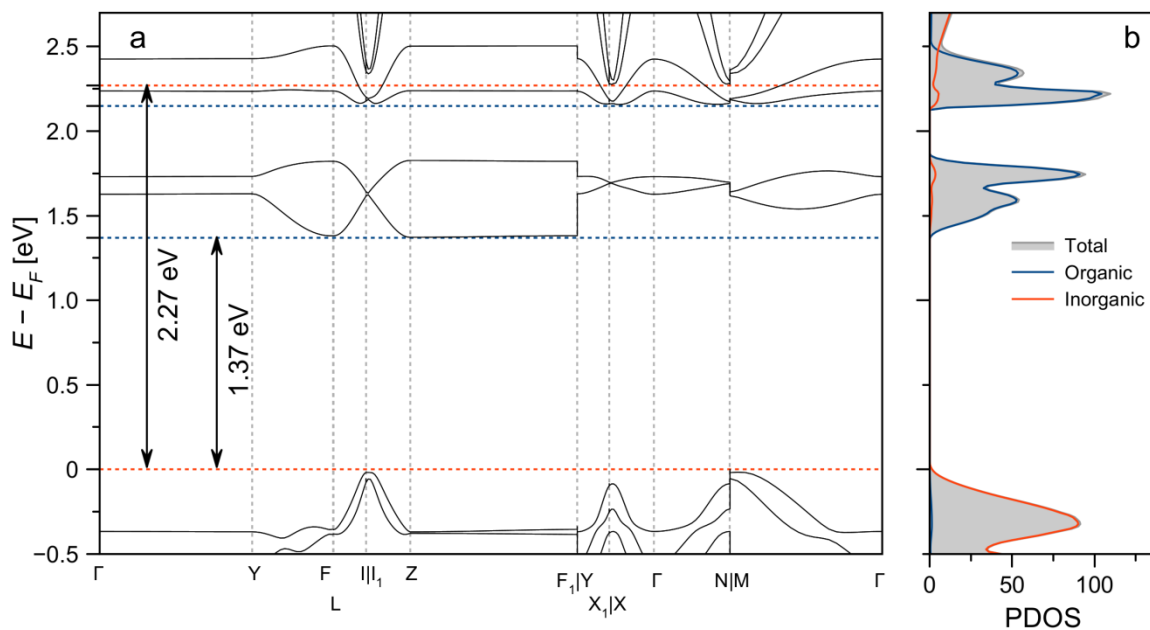


**Figure S13.** Calculated electronic structure of (3cp)PbBr<sub>3</sub>: band structure (a), total DOS and organic/inorganic subsystems contribution.

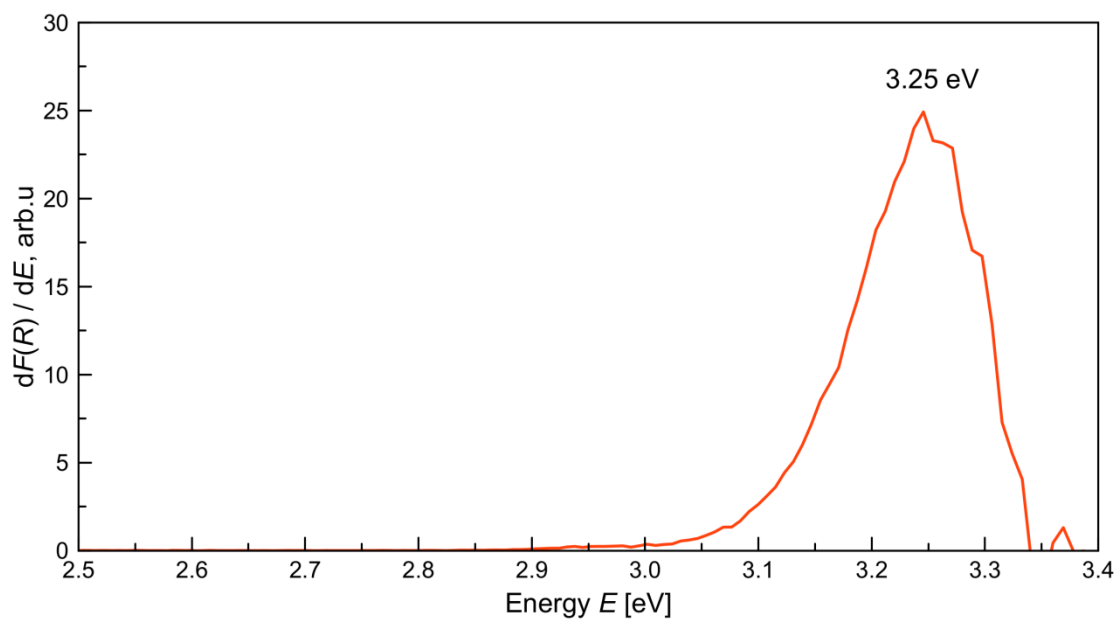


**Figure S14.** Kubelka-Munk function derivative ( $T = 300$  K).

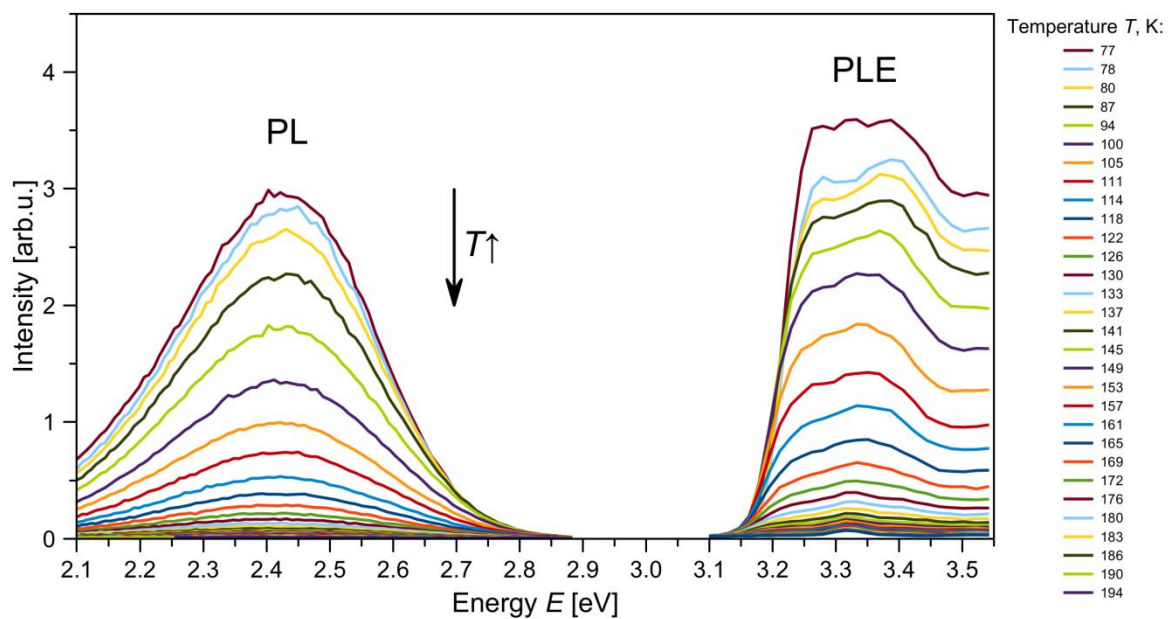


**Figure S15.** Temperature dependence of photoluminescence (PL) ( $E_{ex} = 3.31$  eV) and photoluminescence excitation (PLE) ( $E_{em} = 2.45$  eV) spectra.